Sensing and Emission in Optical Cavities

by

Deniz Aydin

A Dissertation Submitted in Partial Fulfillment

of the Requirements for the Degree of

DOCTOR OF PHILOSOPHY

in the Department of Physics and Astronomy

University of Victoria

We acknowledge and respect the lək̓ʷəŋən peoples on whose traditional territory the university stands, and the Songhees, Esquimalt and W̱SÁNEĆ peoples whose historical relationships with the land continue to this day.

Supervisory Committee

Sensing and Emission in Optical Cavities

by

Deniz Aydin

Supervisory Committee

Dr. Hans-Peter Loock, Supervisor
Department of Physics & Astronomy

Dr. Andrew MacRae, Departmental Member
Department of Physics & Astronomy

Dr. Tao Lu, Outside Member
Department of Electrical and Computer Engineering

Abstract

This work encompasses a study of fibre optic devices and micro-resonator cavities and their use as strain sensors, interferometers, and eventually as light sources. We demonstrate the use of a π-shifted fibre Bragg grating as a strain sensor and quantify its performance through several metrics relevant to its operation in a frequency-locked system. We then discuss the use of waveguide devices as refractive index sensors in a detailed and critical analysis of most of the literature on fibre optic-based interferometry where we define new metrics of assessment that are aimed to be device-independent. We then categorize and study the performance of the literature on fiber-optic refractive index sensors and highlight few key devices of each category based on their performance or design. We relate the performance of these interferometers to various design parameters to outline a way for future researchers to create high-performance devices. Finally, we study light emission in dye-loaded droplet micro-resonators, which are a promising new platform to generate low-threshold lasing action excited by lasers coupled to the whispering gallery modes of the resonator. We characterize multiple types of emissions in these cavities and pave the way for future microdroplet-based lasers.

Table of Contents

List of Figures

Acknowledgments

In this work, I would like to acknowledge the continued and tireless support of my supervisor, Dr. Peter Loock. Throughout the years he kept me inspired, motivated, and shared his contagious enthusiasm for the work we did together. His unconditional support helped me see my future bright and clear.

Major thanks also to Dr. Jack Barnes. He has been incredibly patient and pivotal in helping me understand the nuances of the physics covered by this thesis and more. Without his input I would be lost.

Special thanks to Dr. Gianluca Gagliardi, Dr. Antonio Giorgini, and the rest of the team at INO Naples for their time, hospitality, and support in all ways imaginable during my 3-week stay which turned into a very fruitful collaboration.

I would also like to acknowledge Dr. James Fraser's advice on all matters graduate school and his willingness to always listen. To Dr. Andrew MacRae, thank you for the time you have taken to discuss my misbehaving error signals and for your kindness in suggesting ways to improve my thesis!

I admire my labmates for their support and professionalism without which I would not have enjoyed myself as much as I did during my time at the Loock Lab.

People outside of graduate school have kept me grounded throughout my journey, and for that I will be forever grateful. Special thanks to my parents, my family, and my friends scattered throughout the world.

Also major thanks to our administrative staff both at Queen's and at UVic who have helped my transition back into academia smooth and painless. I could have only wished for as helpful people.

Dedication

In loving memory of my maternal grandmother.

Chapter 1 Introduction

In this work we present three types of sensors -- all are based on optical waveguiding. While their function, appearance, and applications widely differ, they have common elements that provide a recurring theme throughout this thesis. These sensors measure strain, refractive index, and optical gain in waveguide structures. The first two types of sensors employ fiber optic sensor heads, whereas the third device relies on optical waveguiding in so-called whispering gallery modes.

All sensor systems use tunable diode lasers with high temporal coherence and therefore narrow linewidth to measure phase changes associated with the sensor head's response to a change in environmental conditions – to wit: presence of acoustic waves or changes in concentration of an analyte.

The first of the three sensor systems uses a fiber optic sensor head to measure strain at a particular location at the end of a very long fiber tether. This system was developed in response to a need in seismic monitoring using passive devices that can be deployed on the ocean floor and are capable of sensing minute changes in deformation, pressure, and infrasound.

The Pacific Coast is often said to be overdue for a megathrust earthquake[1]. In this context, there is a vested interest to develop earthquake early warning systems (EEWS) and *in situ* monitoring architectures that allow for vibrations to be translated to an electro-optical signal to be transduced to the shore, preferably in time to enact harm reduction measures. Optical detection methods are a promising platform through which EEWS can be developed owing to their chemical inertness, unparalleled speed, immunity to electromagnetic interference, and their ability to be integrated with the present-day telecommunications backbone. The types of optical fibre-based sensors used in EEWS fall typically under the category of fibre Bragg gratings (FBG), a type of in-fibre mirror. Compared to other in-fibre sensors, FBGs are robust in that the gratings are written directly into the fibre without changing the fibre diameter. This fact presents possibilities in their field use in smart structures for strain or temperature sensing applications[2]. In Chapter 2, we present a π-shifted fibre Bragg grating (π-FBG) as an

acoustic sensor for earthquake detection. We employ a frequency-locked signal monitoring scheme that allows us to actively track the central fringe in the reflection spectrum of a π-FBG. Any deviations from the central peak location are converted into a feedback signal to re-centre the laser. As the acoustic vibrations disturb the cavity, the laser needs to be stabilized according to the disturbance, and we can infer the strain that created the disturbance from the amount of wavelength adjustment required. Using this detection setup, we characterize our sensor and compare its performance metrics to a previous sensor used by our group.

The second class of in-fibre sensors has been developed for refractive index-based detection. In Chapter 3, we present a critical analysis of most of the literature on in-fibre interferometry encompassing Mach-Zehnder, Michelson, Fabry-Pérot, and Sagnac interferometers. In these in-fiber interferometers, light is typically split into a reference and a sensing arm and is later recombined to give an interference pattern at the output. Light in the sensing arm is made to interact with a sample whose RI is changing. The light in the two paths is then recombined to create the interference pattern. In our work, we aim to give a solid understanding of the performance metrics, both previously used and presently defined. We compare the performance of different devices by analyzing each category of sensor independently and suggest ways in which future designs can be made. Our critical analysis of interferometric sensors based on in-line fibre optic devices is aimed at providing guidelines to help future sensor design based on desired performance metrics.

Chapter 4 explores various types of emission in a spherical, dye-loaded microdroplet cavity. Here, we report on preliminary experiments demonstrating the emission of light in traveling wave cavities by using spherical microdroplets of solvent loaded with laser dye. The use of a traveling wave cavity here contrasts with the previous two chapters where standing wave cavities are considered in various sensing architectures. As such, we explore whispering gallery modes (WGMs) that can be excited and lead to coherent emissions. We characterize a non-resonant coherent emission from the microdroplet cavity by exciting whispering gallery modes (WGMs) at

the excitation wavelength. In this work, we show an unusual combination of a low vapour pressure solvent (polyethylene glycol and glycerol) to dissolve the laser dye 4-(Dicyanomethylene)-2-methyl-6-(4-dimethylaminostyryl)-4H-pyran (DCM) to create optically stable droplets, and we localize them using a segment of an optical fibre from which the droplets are suspended.

These abovementioned chapters are summarized and concluded in Chapter 5, where we also present a future outlook on these projects and suggests possible venues that could be explored in continuation. In particular, suggestions are made to bring the π-FBGs of Chapter 2 to one step closer to combining the best features of polarization insensitivity *and* narrow linewidth fringes in one device to achieve stable and sensitive operation, as has been done in [3,4]. Moreover, we outline the achievements of the various types of sensors that have been found to be performant in our analysis in Chapter 3. Finally, we present a plan for Chapter 4 in order to observe and quantify lasing in these glycerol/polyethylene glycol microcavities.

Chapter 2 Seismic Monitoring with π-shifted Fibre Bragg Gratings

2.1. Introduction

In this chapter, we review the importance of fibre-optic sensors as earthquake early warning systems (EEWS), describe π-shifted fibre Bragg gratings and their applications in seismic monitoring, and characterize one such device as linked to various length tethers for localized remote sensing.

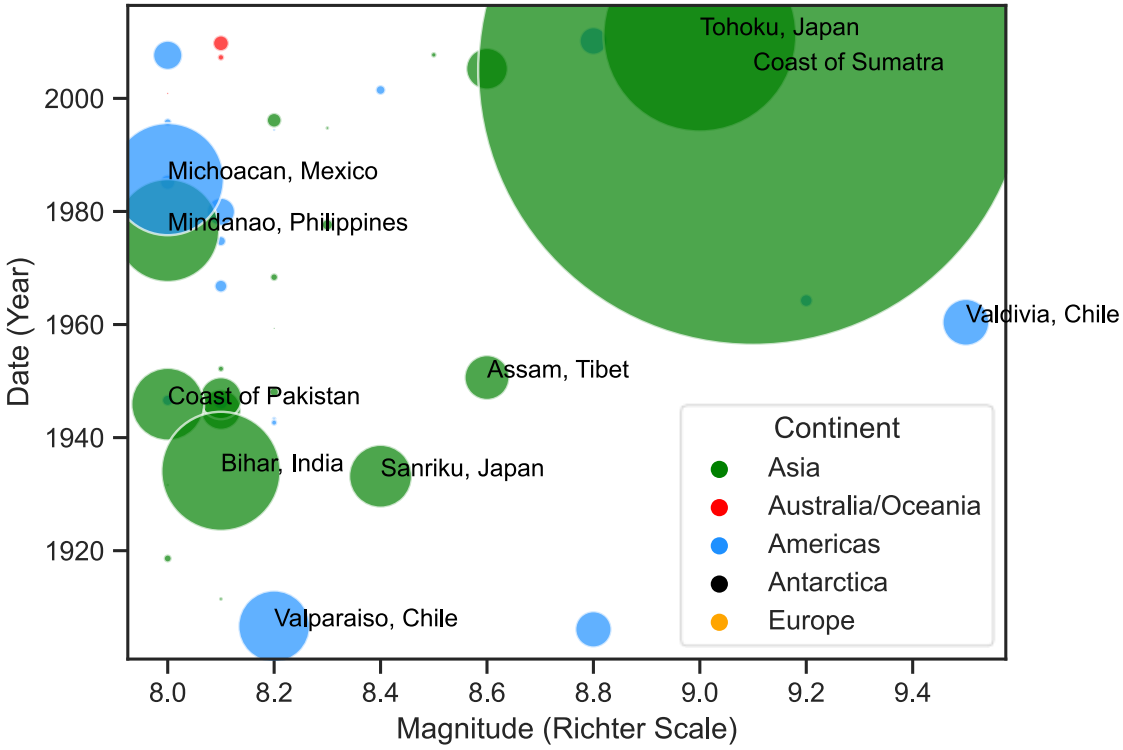

Figure 1. Earthquakes of magnitude 8.0 and greater since 1900[5].Size of the marker is linearly proportional to the number of fatalities.

Figure 1 shows data on the major earthquakes of magnitude 8.0 or greater that spans the last 120 years[5]. The particularly catastrophic tremors with more than 1500 fatalities are labeled with their respective epicentres. Of these, the death toll of the 5 deadliest ones exceeds a quarter million people. The 9.1 M_w 2004 Sumatra–Andaman earthquake and tsunami in the Indian Ocean alone killed an estimated 228,000 people.

It must be noted that earthquakes that are weaker can still produce devastating consequences, as have been experienced historically worldwide[6].

On the Pacific coast where we are located, the locals speak of the “Big One” -- the megathrust earthquake of magnitude 9.0 that is expected to hit British Columbia sometime in the next 50 years with 10% chance. The Big One is expected to originate from the Cascadia subduction zone, some 110-160 km to the West of the Pacific coast shoreline. While this ominous earthquake is the one most have heard of, it is not the only one: there is another crustal earthquake with a 7.0 magnitude and an epicentre located between Victoria and Vancouver anticipated to hit in the next 50 years with 20% chance[7]. Experts have estimated that the Big One alone could kill 10,000 and injure another 26,000[1]. Given the odds and the magnitude of the potential disaster, both public and private interest in earthquake early warning systems (EEWS) is clearly justified.

EEWS have the capacity to detect impending preliminary shock waves as they occur, thereby providing users with enough time to broadcast warnings and enact harm reduction measures before the secondary waves hit. The minimal time it takes to detect an earthquake is proportionally related to the distance to the epicentre as well as the delays in signal transmission and processing. Therefore, reducing the latency in EEWS detection schemes is of interest to public health and safety, particularly in active fault zones.

Optical strain sensors systems are being developed as EEWS owing to their capability to operate far away from power outlets, their immunity to electromagnetic interference, their chemical inertness, their high sensitivity, and their inherent aptness to be used over long distances with low loss. Systems akin to long-haul transmission lines based on long optical fibre links are of interest due to their compatibility with existing technology, their capacity to be manufactured for rugged environments and their performance. In this work, we propose a π-shifted fibre Bragg grating (FBG) as an optical sensor to detect remote acoustic waves, and a standard single-mode fibre to

relay strain information. In the following section, we first discuss requirements for transducers used in EEWS and then focus on the π-shifted FBG as a sensor.

2.2. Literature Review

Fibre sensors are advantageous in a number of ways including chemical inertness, immunity to electromagnetic interference, ability for remote and possibly passive sensing, and compatibility with the telecommunications backbone[8]. Remote sensing based on optical fibres can be further categorized into three distinct subgroups: localized (or point) sensing, quasi-distributed sensing, and distributed sensing[8]. This chapter concerns itself with a type of point-sensor known as a π-shifted FBG, but a brief overview of each of the three subgroups can be found here and can be seen in Figure 2, adapted from [8].

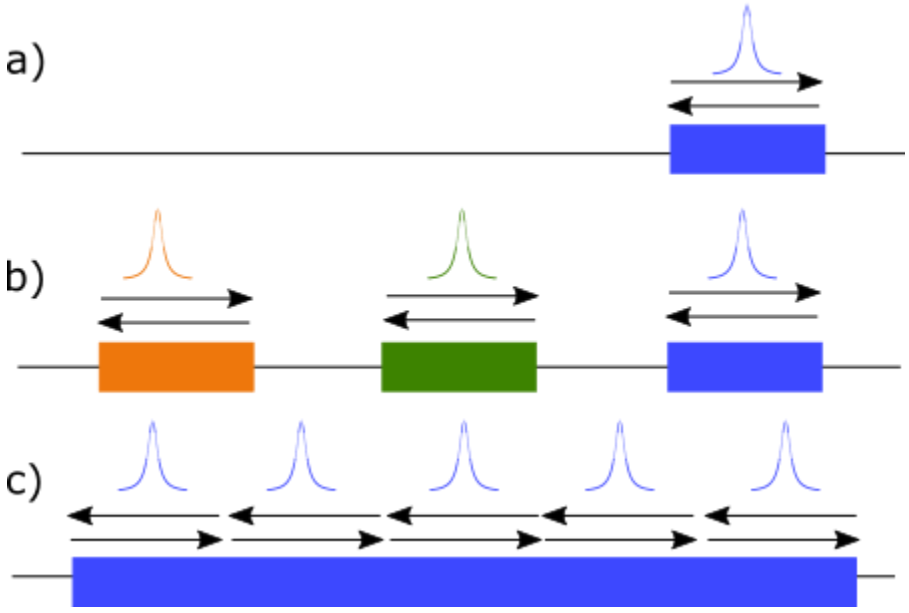

Figure 2. Three main types of fibre sensing architectures. (a) Single point (or localized) sensors, (b) quasi-distributed sensing with multiple point sensor heads cascaded on a single optical fibre, and (c) distributed sensing architecture that can continuously probe an entire length of fibre.

Localized sensors, as the name indicates, are sensors written on a particular section of an optical fibre that allow for the detection of changes at a specific location. These sensors can be compact with dimensions ranging from millimeters to centimeters, but they are also only sensitive to disturbances at this indicated location. It is possible then to use a cascade of these sensors, separated physically by stretches of regular optical fibre and spectrally by the shifted location of their resonances. A single optical fibre can then bear a number of in-line sensor heads, each one of them located at a particular site of the fibre, able to detect changes in more than one location. This cascading method is aptly named as quasi-distributed sensing, in that one now has more location information, but the information resolution is still limited by the number of sensor heads placed written in the fibre. The event locations are also correspondingly discretized, and it may be difficult to resolve or even detect an event that falls between two sensors. Finally, one can devise a sensing architecture that allows for the continuous monitoring of an entire length of an optical fibre in a distributed sensing setup. These sensors are typically based on different optical phenomena such as Brillouin, Rayleigh, or Raman scattering.

Many localized fiber sensors for sound, pressure, and even temperature are based on the detection of strain on the fiber. Strain (ε) is a dimensionless quantity given as the fractional length change of the fiber: $\varepsilon = dL/L$. A sensor with 1 nε (nanostrain) limit of detection is therefore able to resolve a 1 nm length change on a 1 m segment of fiber.

FBGs are of particular interest in point strain sensing because of their rugged nature compared to other sensors such as tapers, S-bends, and etched structures. Moreover, they have widely tunable geometries that allow one to tailor the output spectrum to the particular application. Previous works have presented fibre Fabry-Pérot (FFP) cavities made from two identical FBGs (FFP-FBGs) as localized strain sensors[9-11]. These FFP-FBG sensors are the mainstay of frequency-locked strain detection architectures owing to their narrow linewidth. As frequency-locked sensing is typically based on the derivative of the fringe lineshape[12], a narrower fringe will necessarily lead

to a steeper zero-crossing in the derivative signal, so an excursion in frequency will be associated with a larger amplitude feedback signal. As a result, the fluctuations in frequency can be accurately corrected. While exceptional limits of detection (picostrain, $p\varepsilon$ [3]) and remoteness (100 km^3) have been achieved with these sensors, a concern with these architectures is their polarization dependence, although some authors have apparently overcome these difficulties in recent years [3,4]. In this work, we develop a polarization-insensitive sensor head at the expense of limit of detection.

2.3. Seismic Waves

Tectonic plate movements, volcanoes, explosions, and landslides can all cause acoustic waves that travel through the earth[13]. In the following, we develop the formalism required to understand seismic waves based on equations and constants that can be found in the literature[14]. These waves, termed seismic waves, have different types, and can be characterized by their mode of propagation. The body waves are composed of compressional (longitudinal) *primary (P) waves* and transverse *secondary (S) waves*. The P-waves are caused by wavelike compression and decompressions of the propagation medium *along* the direction of propagation. As per their name, they propagate quickly and arrive first at locations far from the earthquake focus. The S-waves or the *shear waves* displace the propagation medium *perpendicular* to the direction of propagation and arrive later. S-waves typically travel at 60% of the speed of the P-waves. S-waves only occur in solid media, since the modulus of rigidity μ that determines the velocity as per Equation (2.3.2) is zero in liquids and gases. Typical velocities for the P-waves and S-waves are 5.5 km/s and 3.0 km/s respectively in surface rocks (e.g., granite). These values rise to 13.0 km/s and 7.0 km/s at 2800 km below the surface and drop sharply at the boundary of the Earth's mantle and its outer core region[14].

For P waves the velocity is given by (2.3.1)

$$\alpha = \sqrt{\left(k + \frac{4}{3}\mu\right)/\rho} \qquad (2.3.1)$$

where the velocity α = 5.5 km/s for granite and 1.5 km/s for water. The values of k and μ correspond to the bulk modulus and the modulus of rigidity respectively, and ρ is the density of the elastic material. For granite, $k \simeq 2.7\times10^{10}$ N/m^2, $\mu = 1.6\times10^{10}$ N/m^2. For water, on the other hand, $k \simeq 2.0\times10^{9}$ N/m^2 and $\mu = 0$ N/m^2.

The velocity for S-waves is given by (2.3.2)

$$\beta = \sqrt{\mu/\rho}\,. \qquad (2.3.2)$$

and can be calculated using the values for μ and ρ above. In addition to body waves, there exist *surface waves* along the free surface of an elastic medium. Surface waves, in turn, fall into two broad categories known as *Rayleigh waves* when their velocity is less than 0.92 β (where β indicates the velocity of the S-wave in the rock), and *Love waves* which can survive in layered solids traveling at a speed intermediate to the S-wave speeds in each layer. Then, one can also consider the reflected and refracted waves at each boundary for a complete treatment of the waves arriving at a particular point. Interestingly, seismic waves that travel along the boundary have qualities not unlike those of optical whispering gallery modes in that they are guided at the interface of two media, as described in Section 4.3.

In the following section I describe the types of sensors used in our seismic detection studies and their advantages. I discuss the disadvantages of the previous generation of sensors and address how one might resolve those issues.

2.4. Fibre Bragg Gratings

Fibre cavities written in single-mode optical fibres are widely used in strain detection. These cavities are typically fibre Bragg gratings (FBGs), π-shifted FBGs (π-FBGs), or Fabry-Pérot cavities made of a pair of two identical FBGs (FFP-FBGs). The working principle of an FBG is shown in Figure 3: (a) in an FBG, the periodic alternation in the refractive index (RI) acts as a broadband mirror, reflecting a range of wavelengths

and causing a dip in transmission. (b) in an FFP-FBG, two FBGs are stacked with a gap in between, creating a standing wave cavity. This results in a comb structure in transmission. (c) a π-shifted FBG has a structure like that of a regular FBG, but there is a missing "tooth" which creates a phase shift of π between the reflected and inbound waves. The optical spectrum of the π-FBG has a narrow wavelength region where the incident light and the back-reflections are π-shifted with respect to one another and cancel out, leading to a very narrow notch in the reflected spectrum and a corresponding peak in transmission.

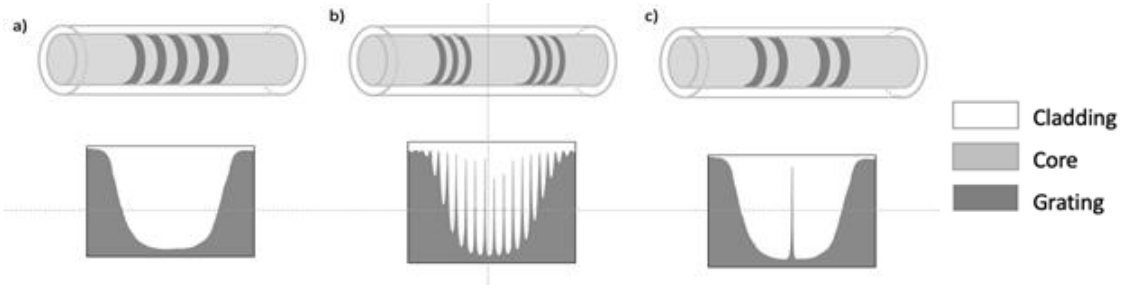

Figure 3. Schematic and transmission spectra of an FBG, a FP-FBG, and a π-FBG[15].

Previous work from our group has used FFP-FBGs to detect vibrations with a 1 nε resolution limit[16]. These gratings are formed by a periodic alternation of the refractive index typically achieved by ultraviolet laser writing methods[17]. In our prior publications, we have used laser-locked FFP-FBGs for strain sensing but observed that the technique was susceptible to polarization wander that resulted in peak splitting and lock instability. While the extremely narrow (sub-picometer) features of the FFP-FBG spectrum allow for an accurate detection of the strain applied, the peak splitting observed in operation under conditions in which polarization cannot be well-controlled prevents this system from being widely used in the field. Moreover, the length of the tether between the sensor and the experimental setup has previously been curbed to 10 km by the onset of Stimulated Brillouin Scattering (SBS). In this work, we propose to address these two limitations by two methods: firstly, we suggest the use of an amplifier

for longer tethers to boost the back-reflected signal before it is returned to the photodiode, and we demonstrate the use of polarization-insensitive π-shifted FBGs, instead of FFP-FBG cavities. Previous experiments from our group have demonstrated that the result of polarization wander in FFP-FBGs was birefringent peak-splitting due to slightly different refractive indices for the two orthogonal polarization modes. In these experiments, the state of polarization (SOP) had to be controlled before it is launched into the FFP-FBG cavity such that only a single peak was returned from the cavity, and a PDH lock can be performed. The use of π-FBGs deal with this issue by simple employing a broader linewidth reflection dip, which ostensibly still splits, but the effect is "washed out" in the broad response of the cavity. There is then a trade-off between obtaining a narrow-linewidth peak from the cavity for locking purposes and having a peak broad enough to be effectively immune to peak splitting. We tested the polarization insensitivity of this new type of sensor with a polarization controller inserted into the launch port and adjusting the SOP. The peak from the π-FBG remained stable and did not appear to split. In systems where birefringence causes peak splitting, the effective refractive index of the different polarization modes and therefore the amount of birefringence can be calculated from the Bragg formula $\lambda_B = 2n_{eff}\Lambda$.

The π-FBG used in these experiments were produced by our collaborators at Ryerson University (Dr. Xijia Gu, Department of Electrical, Computer, and Biomedical Engineering). The grating has been written in a Clear Curve fibre from Corning Inc. The centre wavelength is 1549.57 nm and the bandwidth of the envelope is 0.90 nm. A typical transmission spectrum is shown in Figure 5. Note that the spectral resolution of the spectrometer does not allow us to measure the spectral width of the centre fringe. Instead, we measured the linewidth of this FBG (5.61-6.28 pm, Figure 4, depending on the average windowing of 200 or 100 points respectively) by cross-referencing the photodiode signal with the laser scan ramp given the laser transfer function of 50 mA/V and the laser tuning characteristic of 3.38 pm/mA.

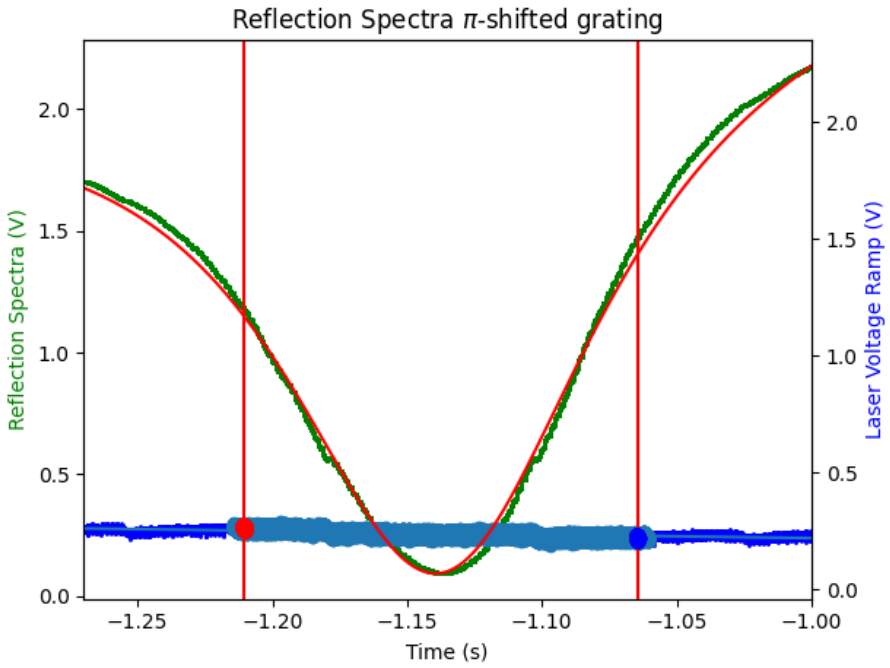

Figure 4. Determination of the π-FBG linewidth. The narrow reflection dip is shown (green) overlaid with a Lorentzian fit with a linear baseline (red). The voltage scan ramp used to drive the laser is shown in navy, and the linewidth (5.61-6.28 pm) is determined from an average of 100 to 200 data points around the FWHM points due to amplitude noise in the laser driver voltage.

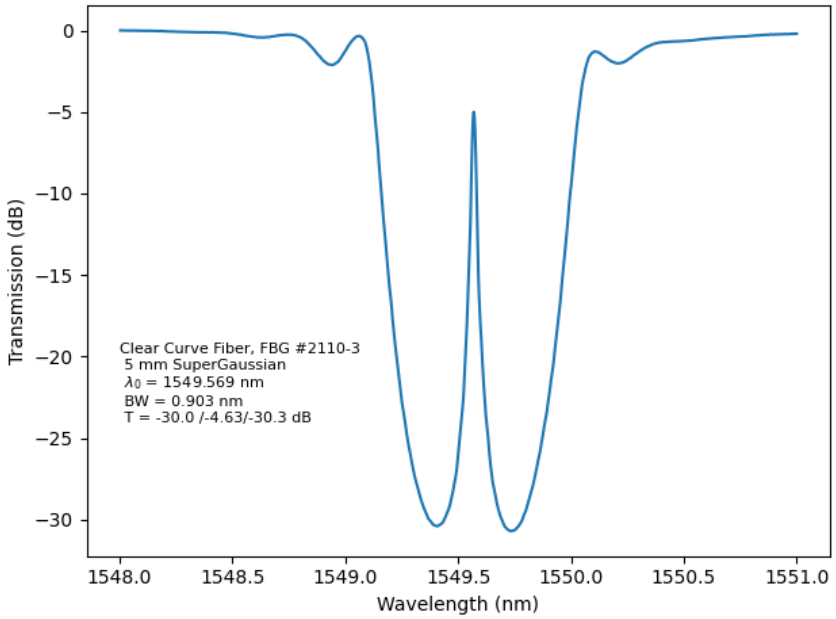

Figure 5. Transmission spectrum of the π-FBG sensor used in experiments, supplied by Ryerson University. The location of the narrow linewidth transmission peak is 1549.60 nm, and its extinction ratio exceeds 25 dB. The bandwidth of the stopband is 0.90 nm.

2.5. Pound-Drever-Hall Frequency Locking

Typical measurements of strain using optical signals are based on detecting changes in the reflection or transmission spectrum as a function of applied strain. Given that straining a cavity changes both its physical length and its effective refractive index, the *optical path length* as defined per (3.1.1) is altered by these external variations. Early strain sensing methods were based on transmission intensity measurements, which are limited in dynamic range. This issue arises from the fact that transmission intensity measurements only remain linear in an extremely limited range around the resonant peak, i.e., near the two inflection points of a resonant peak. Moreover, fluctuations in transmitted light intensity can be due to ambient changes such as thermal noise and due to system noise arising from laser power- or frequency-jitter, rather than a true wavelength shift. For these reasons, actively frequency locked systems are preferred since they exhibit inherently larger dynamic ranges, as well as higher sensitivities[18].

The Pound-Drever-Hall technique is based on active frequency stabilization and uses closed-loop feedback control. In this technique, the laser is actively locked to the narrow transmission peak (reflection dip) of a fiber sensor such as a π-shifted FBG. In our lab we electronically take the derivative of the dip in the back-reflection signal and feed back this derivative to the laser driver. As this derivative signal is a bi-polar signal, it indicates the degree and direction of the detuning from the centre wavelength. By decoupling the frequency from the transmitted intensity, we can accurately lock and maintain the laser frequency[12].

2.5.1 Theory

The theoretical concepts used by the Pound-Drever-Hall technique as applied to a monochromatic beam are derived below. Following the treatment by [12,19] we start with the expression for the beam incident on the π-shifted FBG:

$$E_{inc} = E_0 e^{i\omega t} \tag{2.5.1}$$

and follow with the equation for the beam reflected by the π-shifted FBG cavity, which here is treated like a short FBG cavity:

$$E_{ref} = E_1 e^{i\omega t}. \tag{2.5.2}$$

where E_0 and E_1 are the complex amplitudes, and ω is the frequency of the radiation. The reflection coefficient is then written as:

$$F(\omega) = \frac{E_{ref}}{E_{inc}} = \frac{r\left(\exp\left(i\frac{\omega}{\Delta\nu_{fsr}}\right)-1\right)}{1-r^2\exp\left(i\frac{\omega}{\Delta\nu_{fsr}}\right)} \tag{2.5.3}$$

for a cavity with two identical mirrors with reflectivity r, and where $\Delta\nu_{fsr} = c/2L$ is the free spectral range of the cavity of length L. Like in any Fabry-Pérot cavity, in the resonance condition, the beam that is immediately reflected from the first mirror (the *promptly reflected beam*[12]) interferes destructively with the standing wave that couples back out via the first mirror (the *leakage beam*). Since the promptly reflected beam and the leakage beam have the same amplitude and are 180° out of phase, the total reflected beam vanishes upon superposition. If the two waves are not perfectly out-of-phase, the phase of the total reflected light will be indicative of which side of the resonance the laser is on (Figure 6).

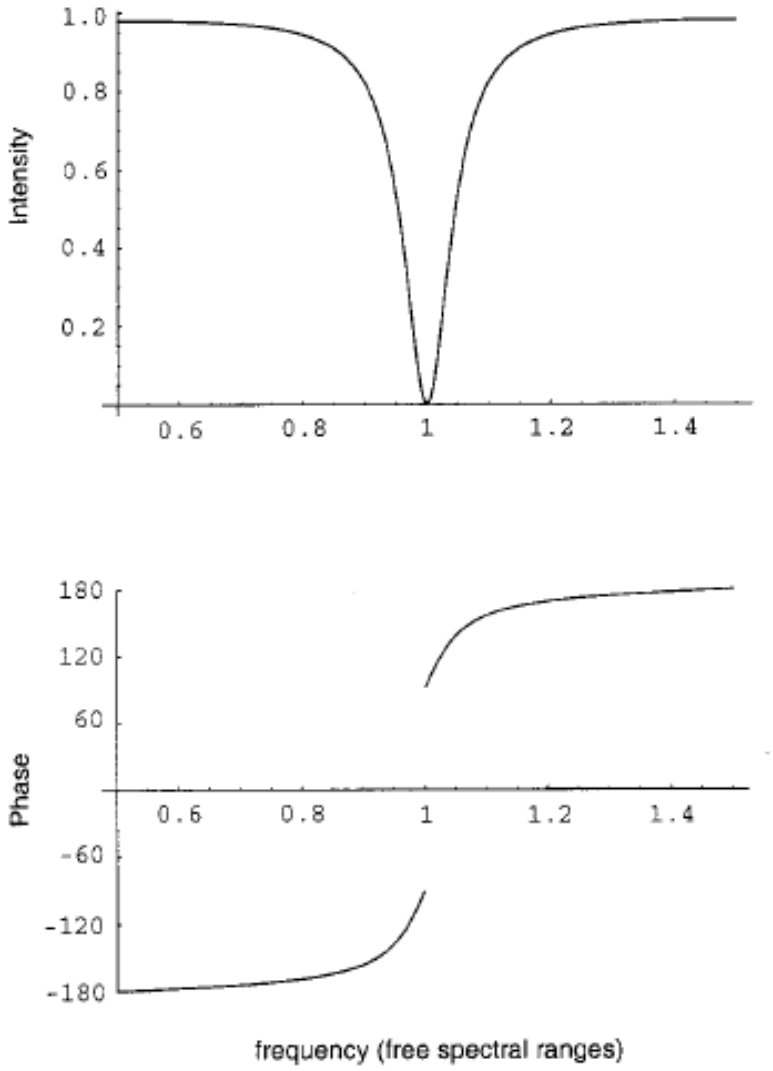

Figure 6. Adapted from[12]. Amplitude and phase of the total light reflected from a Fabry-Pérot cavity. Note the discontinuity in phase caused by the total reflected power vanishing at resonance.

As the phase of an electromagnetic wave cannot be directly measured, we turn to frequency dithering to generate sidebands that will have a fixed frequency relationship to the incident beam. By then interfering these sidebands with the reflected beam, we get a beat pattern that oscillates at the sum and difference frequencies. The phase of this beat pattern can be measured using intensity detection as per (2.5.11).

The modulated beam incident on the cavity can be expressed as

$$E_{inc} = E_0\left(1+\alpha\cos\left(\omega_m t\right)\right)e^{i\left(\omega-\delta\cos\left(\omega_m t\right)\right)t} \tag{2.5.4}$$

where α is the amplitude modulation depth and δ is the frequency modulation depth, and ω_m is the modulation frequency. As we can see, current modulation of the diode laser creates both an AM and an FM component. The frequency-phase relationship can be expressed as

$$\omega = \frac{d\Theta(t)}{dt} \tag{2.5.5}$$

where ω is the instantaneous frequency of oscillation of the incident wave, and Θ is the phase. This relationship can be used to write the frequency modulation shown in (2.5.4) in terms of an equivalent phase modulation in (2.5.6), with the Euler's identity replacing the cosine term in the amplitude modulation [19]

$$\begin{aligned} E_{inc} &= E_0\left(1+\alpha\cos\left(\omega_m t\right)\right)e^{i\left(\omega t+\beta\sin\left(\omega_m t\right)\right)} \\ &= E_0\left(1+\frac{\alpha}{2}\left(\exp\left(i\omega_m t\right)+\exp\left(-i\omega_m t\right)\right)\right)e^{i\left(\omega t+\beta\sin\left(\omega_m t\right)\right)}. \end{aligned} \tag{2.5.6}$$

This latter can then be expressed in terms of Bessel functions

$$E_{inc} \simeq E_0\left(1+\frac{\alpha}{2}\left(\exp\left(i\omega_m t\right)+\exp\left(-i\omega_m t\right)\right)\right)\left[J_0\left(\beta\right)+2iJ_1\left(\beta\right)\sin\omega_m t\right]e^{i\omega t} \tag{2.5.7}$$

And using Euler's identity for sine,

$$E_{inc} = E_0\left(1+\frac{\alpha}{2}\left(\exp\left(i\omega_m t\right)+\exp\left(-i\omega_m t\right)\right)\right)\left[J_0\left(\beta\right)e^{i\omega t}+J_1\left(\beta\right)e^{i(\omega+\omega_m)t}-J_1\left(\beta\right)e^{i(\omega-\omega_m)t}\right]$$

(2.5.8)

which can be approximated in the case of $\beta \ll 1$ as

$$E_{inc} = E_0 e^{i\omega t}\left(1+\frac{\alpha}{2}\left(\exp\left(i\omega_m t\right)+\exp\left(-i\omega_m t\right)\right)\right)\left[1+\frac{\beta}{2}e^{i\omega_m t}-\frac{\beta}{2}e^{-i\omega_m t}\right] \tag{2.5.9}$$

and eventually as

$$E_{inc} = E_0 e^{i\omega t}\left(1+\frac{\alpha+\beta}{2}\exp\left(i\omega_m t\right)+\frac{\alpha-\beta}{2}\exp\left(-i\omega_m t\right)+\mathrm{O}\left(\exp\left(2i\omega_m t\right)\right)+\ldots\right).$$

(2.5.10)

In (2.5.10) we only consider the terms oscillating at the modulation frequency because the higher order terms' coefficients are much smaller than one, given $\alpha,\beta,\delta \ll 1$. Multiplying the incident field with the reflection coefficient yields a three-term expression as only in-phase components survive the product

$$E_{ref} = E_0\left[F\left(\omega\right)e^{i\omega t}+\frac{\alpha+\beta}{2}F\left(\omega+\omega_m\right)e^{i(\omega+\omega_m)t}+\frac{\alpha-\beta}{2}F\left(\omega-\omega_m\right)e^{i(\omega-\omega_m)t}\right]$$

(2.5.11)

This expression, when multiplied with its complex conjugate, yields the reflected power

$$P_{ref} = \left|E_0\right|^2\left\{\begin{array}{l}\left|F\left(\omega\right)\right|^2+\left(\frac{\alpha+\beta}{2}\right)^2\left|F\left(\omega+\omega_m\right)\right|^2+\left(\frac{\alpha-\beta}{2}\right)^2\left|F\left(\omega-\omega_m\right)\right|^2 \\ +\left\{\begin{array}{l}\mathrm{Re}\left[\left(\alpha+\beta\right)F\left(\omega\right)F^*\left(\omega+\omega_m\right)-\left(\beta-\alpha\right)F^*\left(\omega\right)F\left(\omega-\omega_m\right)\right]\cos\omega_m t \\ +\mathrm{Im}\left[\left(\alpha+\beta\right)F\left(\omega\right)F^*\left(\omega+\omega_m\right)-\left(\beta-\alpha\right)F^*\left(\omega\right)F\left(\omega-\omega_m\right)\right]\sin\omega_m t\end{array}\right\}\end{array}\right\}$$

(2.5.12)

The power in the carrier is given by

$$P_C = P_0 J_0^{\,2}\left(\beta\right) \tag{2.5.13}$$

taking into account $P_0 = \left|E_0\right|^2$ and the power in the sidebands

$$P_S = P_1 J_1^2\left(\beta\right). \tag{2.5.14}$$

The total reflected power is then

$$P_0 \approx P_C + 2P_S \tag{2.5.15}$$

for $\beta < 1$, i.e., small modulation depth and $P_0 = \left|E_0^{'}\right|^2$.

Depending on the modulation regime, either the sine or the cosine term that oscillates at ω_m will dominate the expression for reflected power.

Using a mixer, we form the product of the two waves being mixed: the photodiode and the local oscillator signals. Since only identical trigonometric terms are parallel to one another, the terms that survive in the expression (2.5.12) are the ones in phase with one another. In other terms,

$$\sin\left(\omega_m t\right)\sin\left(\omega_m{}' t\right)=\frac{1}{2}\left[\cos\left(\omega_m-\omega_m{}'\right)t-\cos\left(\omega_m+\omega_m{}'\right)t\right] \tag{2.5.16}$$

where the difference term is a constant and multiplies the error signal we are looking for. This term can be isolated by a low-pass filter. Below I outline how the term preceding the trigonometric terms in (2.5.12) yield the error signal.

Low modulation frequencies (slow modulation regime, $\omega_{m,slow} << \Delta\nu_{\pi-FBG}$):

$$\omega(t)=\frac{d\varphi}{dt}=\frac{d\left(\omega t+\beta\sin\omega_m t\right)}{dt}=\omega+\omega_m\beta\cos\omega_m t \tag{2.5.17}$$

$$\begin{aligned} P_{ref}\left(\omega+\omega_m\beta\cos\omega_m t\right) &\approx P_{ref}\left(\omega\right)+\frac{dP_{ref}}{d\omega}\omega_m\beta\cos\omega_m t \\ &\simeq P_{ref}\left(\omega\right)+P_0\frac{d\left|F\right|^2}{d\omega}\omega_m\beta\cos\omega_m t \end{aligned} \tag{2.5.18}$$

Where the last term can be expanded

$$\begin{aligned} \frac{d\left|F\right|^2}{d\omega}\omega_m &\approx 2\omega_m\,\mathrm{Re}\left\{F\left(\omega\right)\frac{dF^*\left(\omega\right)}{d\omega}\right\} \\ &\approx F\left(\omega\right)F^*\left(\omega+\omega_m\right)-F^*\left(\omega\right)F(\omega-\omega_m) \end{aligned} \tag{2.5.19}$$

And as per (2.5.18), we have a constant term and a term that oscillates at ω_m. Using a mixer and a low-pass filter, we isolate the sinusoidal term, which we now define as the error signal:

$$\varepsilon=P_0\frac{d\left|F\right|^2}{d\omega}\omega_m\beta \tag{2.5.20}$$

And using the approximation

$$\sqrt{P_C P_S}=P_0\beta/2 \tag{2.5.21}$$

We can write

$$\varepsilon = 2\sqrt{P_C P_S}\,\frac{d\left|F\right|^2}{d\omega}\,\omega_m \qquad (2.5.22)$$

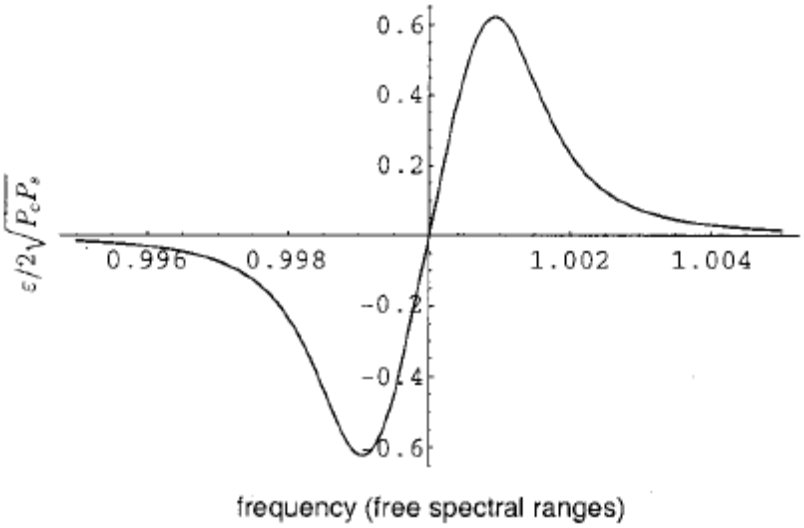

Figure 7. PDH error signal in slow modulation regime (after [12], equation (2.5.22))**.**

High modulation frequencies (fast modulation regime, $\omega_{m,\,fast} >> \Delta\nu_{\pi-FBG}$):

$$F(\omega)F^*(\omega+\omega_m) - F^*(\omega)F(\omega-\omega_m) \approx -2i\,\mathrm{Im}\{F(\omega)\} \qquad (2.5.23)$$

$$\varepsilon = -2\sqrt{P_C P_S}\,\mathrm{Im}\{F(\omega)F^*(\omega+\omega_m) - F^*(\omega)F(\omega-\omega_m)\} \qquad (2.5.24)$$

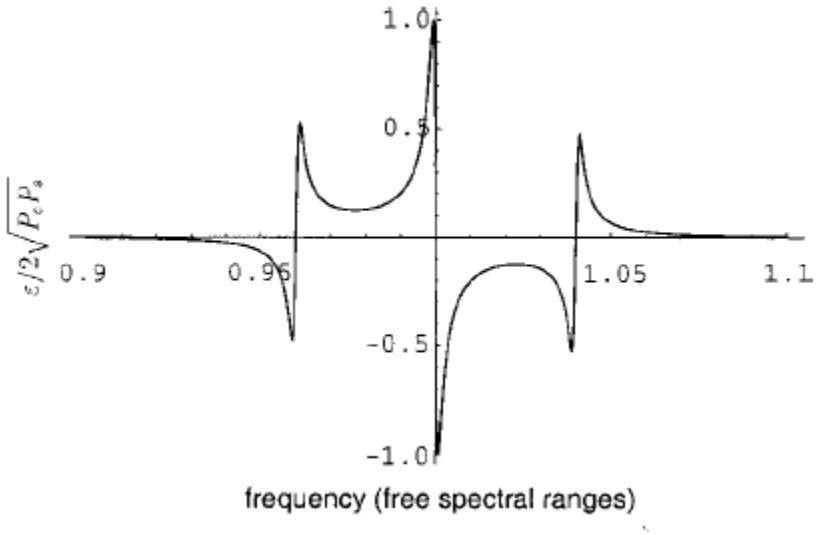

Figure 8. PDH error signal in the fast modulation regime (after[12], equation (2.5.24)).

Below I present our sensor's fringe, the error signal obtained at approximately 42 MHz frequency modulation and the voltage ramp used to drive the laser.

Wavelength-dependent laser power is responsible for the sloping baseline of Figure 9, top figure. On the bottom, we see the error signal in the slow modulation regime. Presently, only a slow modulation regime error signal can be generated owing to the frequency bandwidth limitations of our function generators.

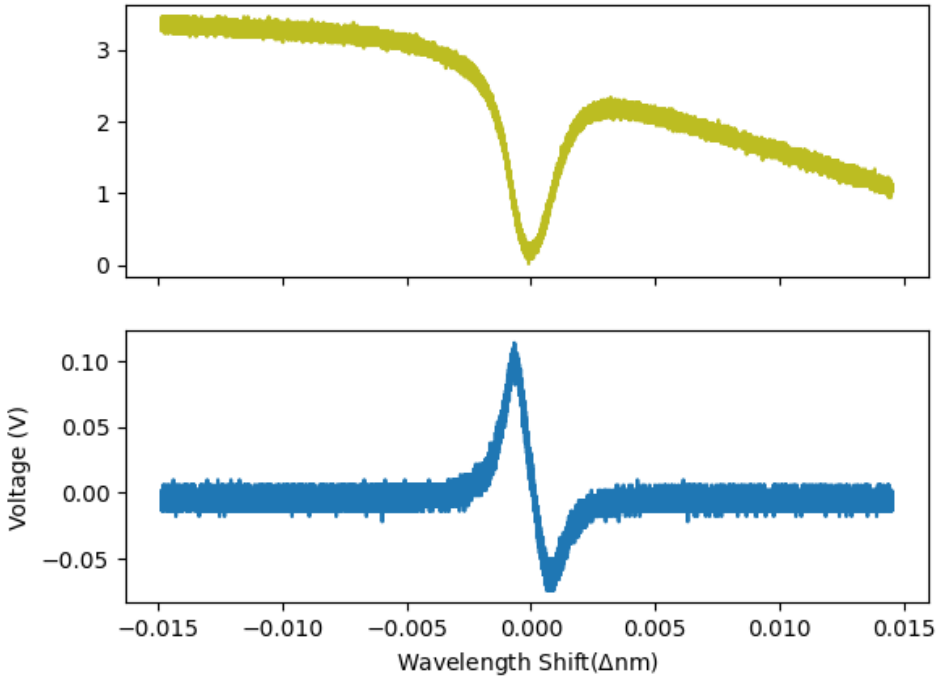

Figure 9. π-shifted FBG back-reflection signal from the photodiode, and its electronic derivative, respectively.

2.5.2 Experimental Setup

A schematic drawing of the Pound-Drever-Hall servo control is shown in Figure 10. A distributed feedback laser (DFB, AVANEX A1905LMI, 1529.55-1569.59 nm, up to 30 mW power) is scanned using a laser driver (Thorlabs IP500) and temperature stabilized using a TEC controller (Thorlabs TCM1000T). An external function generator is used to provide the frequency modulation and a Raspberry Pi B+ microprocessor controls the locking procedure. Either an oscilloscope or a lock-in amplifier can be used for detection, each with its set of advantages. For strain measurements such as system calibration and determining limits of detection, we chose to use a lock-in amplifier for its capacity for low-noise detection. The erbium-doped fibre amplifier (EDFA, denoted AMP in Figure 10) is inserted on the return trip to boost the signal so that a high-quality error signal can be generated from the π-FBG reflection spectrum.

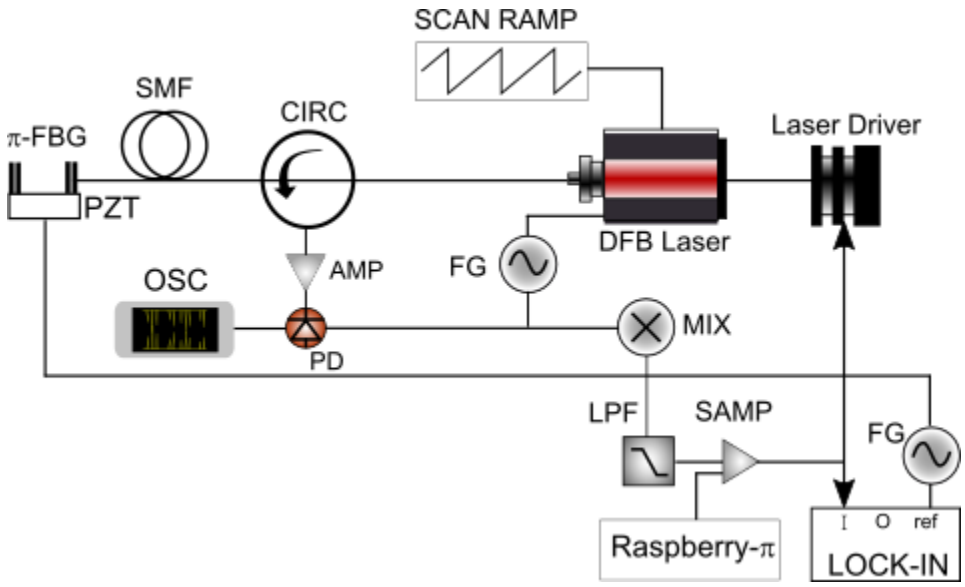

Figure 10. Schematic of the PDH setup.

In Figure 10, DFB is a distributed feedback laser scanned with a sawtooth scan ramp. A circulator (CIRC) redirects light reflected from the cavity into an erbium-doped fibre amplifier (AMP) and eventually into a photodiode (PD). The photodiode converts the signal from the optical domain to the electronic domain. The electronic signal goes into a mixer together with the function generator (FG) signal that drives the laser to produce the derivate signal used in active cavity locking. A low-pass filter (LPF) isolates the frequency components used in locking and eliminates higher-order harmonics. A proportional-Integral (PI) servo amplifier (SAMP) is used in creating the active locking circuit and is controlled by a Raspberry Pi B+. The FG on the lock-in amplifier (LOCK-IN) also drives the piezoelectric ring, at a different frequency (0.5 – 400 Hz) than the FG that modulates the laser (42 MHz). The oscilloscope (OSC) samples the reflected signal from the cavity, the error signal, and control signal from the servo amp.

2.5.3 Strain Sensing

In order to quantify the measured strain response, the π-shifted fibre Bragg grating was subjected to a known and controlled amount of strain using a piezoelectric

cylinder controlled by a sinusoidal driving voltage. The applied AC voltage is transformed into a radial expansion of the piezoelectric cylinder, which in turn stretches the cavity. In this scenario, the static strain applied to the cavity is $\varepsilon = d_{31}\frac{(ID+t)}{2t}\frac{V}{R}$ for the radial displacement of a large-radius tube with strain given as $\varepsilon = \frac{\Delta R}{R}$ as seen in Figure 11[20].

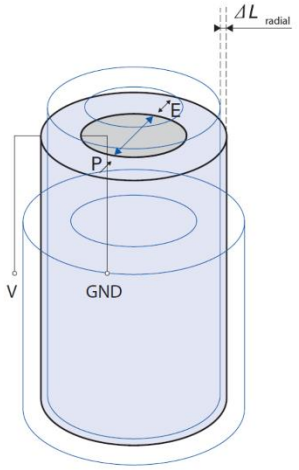

Figure 11. Piezoelectric cylinder in radial expansion mode[20].

In this equation, we see the thickness *t* and the inner diameter *ID*, as well as the d_{31} component of the strain tensor (-1.25×10^{-10} C/N for Navy Type I piezo ceramic), the applied voltage *V* and the radius R of the piezoelectric cylinder. For a modulated applied voltage, the strain

$$\varepsilon = \varepsilon(V, f)\sin(2\pi ft) \qquad (2.5.25)$$

where the strain amplitude depends on the amplitude of the driving voltage as well as its frequency. The piezoelectric cylinder acts as a driven, damped oscillator exhibiting resonances nominally at 1, 6, 10 and 23 kHz. Therefore, the best operation region for this cylinder is between these non-linear transition regions. The maximum rate of change of strain can be calculated based on the applied strain and the driving frequency:

$$\left(\frac{d\varepsilon}{dt}\right)_{\max} = 2\pi f^{*}\varepsilon\left(V, f^{*}\right) \tag{2.5.26}$$

where f^{*} is the maximum frequency that the circuitry is able to track without losing lock on the optical resonance. This unlocking frequency depends on the amplitude of the mechanical oscillation. It will be shown that it is determined, primarily, by the bandwidth of the servo amplifier and the length of the fiber tether, which determines the optical signal delays.

One can also calculate the static strain applied to a cavity from the inline equation above using the dimensions of the piezoelectric transducer (PZT), including the thickness *t*, the inner diameter *ID,* and radius *R*. Additionally, the voltage applied to the PZT (*V)* is needed to calculate the strain experienced by the cavity.

It is straightforward to predict the wavelength change that the π-shifted FBG experiences as a function of applied strain. In the following we assume that the centre wavelength, λ_B, of an FBG with pitch Λ is identical to the wavelength of the π-shifted FBG resonance. This fringe position is then given by, i.e., $\lambda_B = 2n_{eff}\Lambda$ where n_{eff} is the effective refractive index of the π-shifted FBG. Differentiating this expression with respect to *L:*

$$\begin{aligned}\frac{\partial\lambda}{\partial L} &= 2\left(\frac{\partial n}{\partial L}\Lambda + n\frac{\partial\Lambda}{\partial L}\right)\\ &= 2\left(\frac{\partial n}{\partial L}\Lambda + n\frac{\Lambda}{L}\right)\end{aligned} \tag{2.5.27}$$

And multiplying both sides by *L* allows us to rewrite the length derivative in terms of a strain derivative:

$$\begin{aligned}\frac{d\lambda}{d\varepsilon} &= 2n\Lambda\left(\frac{1}{n}\frac{\partial n}{\partial L}L + 1\right)\\ &= 2n\Lambda\left(\frac{1}{n}\frac{\partial n}{\partial \varepsilon} + 1\right)\end{aligned} \tag{2.5.28}$$

The $\frac{\partial n}{\partial \varepsilon}$ term can be expanded as

$$\frac{\partial n}{\partial \varepsilon} = \frac{-n^3}{2}\left[P_{12} - \upsilon\left(P_{11} + P_{12}\right)\right] \approx -0.297 \frac{RIU}{\Delta m / m} \qquad (2.5.29)$$

where the coefficient in front of the refractive index (n = 1.458) contains the expressions for strain-optic coefficients for SMF-28 fibre, $P_{11} = 0.116$ and $P_{12} = 0.255$ (given at 1531 nm [21]), and Poisson's ratio $\nu = 0.17$ [22].The pitch, based on the Bragg wavelength, is Λ = 531 nm with λ_B =1549.569 nm. Strain can then be reduced to the simple expression of $\varepsilon = 8.11 \times 10^{-4} nm^{-1} \times \Delta\lambda(nm)$ as per (2.5.28) and (2.5.29).We then use the tuning characteristics of our laser (3.377 pm/mA) and the transfer function of the laser driver (50 mA/mV) to convert $\Delta\lambda$ into ΔV , to wit, $\varepsilon / \Delta V = 136.9\ n\varepsilon / mV$ giving a calculated system sensitivity of 7.30 $mV / \mu\varepsilon$.

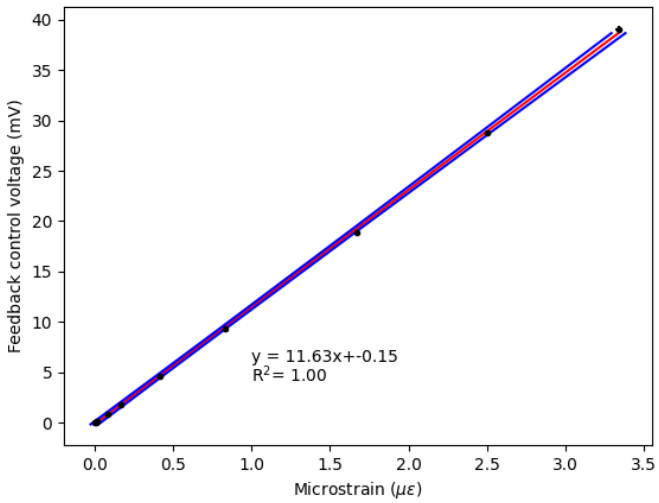

Figure 12. Strain sensitivity calibration at 10 Hz modulation for 0 km (1 m) fibre tether.

Figure 12 shows the strain response of the fibre sensor at a low modulation frequency of 10 Hz. This frequency has been selected to be far enough from the mechanical resonances of the piezoelectric transducer. In this experiment, the feedback

control voltage was measured through a lock-in amplifier as a function of the strain applied to the piezoelectric transducer at the given frequency. Peak amplitude for the sinusoidal strain was changed, and each data point was measured for a minute using a Data Acquisition System (DAQ) to obtain the standard error. The slope of the fit yields a value of 11.63 $mV / \mu\varepsilon$ for the strain experiment run without a tether between the PDH setup and the sensor head in fair agreement with the value of 7.30 $mV / \mu\varepsilon$ calculated above.

The limit of detection has been calculated using the method of calibration curves[23], which is briefly outlined here. Here, *x* stands for the applied strain and *y* is the measured voltage.

A linear regression can be performed on the data in Figure 12, Figure 14, and Figure 16. Accordingly, the slope (the sensitivity of the strain measurement) is determined by

$$m = \frac{\Delta y}{\Delta x} = \frac{n\sum x_i y_i - \sum x_i \sum y_i}{D} \tag{2.5.30}$$

and the y-intercept is given by

$$b = \frac{n\sum x_i^2 \sum y_i - \sum x_i y_i \sum x_i}{D}. \tag{2.5.31}$$

In both (2.5.30) and (2.5.31), the quantity *D* is the determinant of the matrix

$$D = \left| \begin{pmatrix} \sum x_i^2 & \sum x_i \\ \sum x_i & n \end{pmatrix} \right| = n\sum x_i^2 - \left(\sum x_i\right)^2. \tag{2.5.32}$$

The standard error of the fit is calculated from the square of the difference between the fit and an individual datum

$$s_y = \sqrt{\frac{\sum \left(y_i - rx_i - b\right)^2}{n-2}}. \tag{2.5.33}$$

The standard deviation of the sensitivity (slope) and the y-intercept can then be obtained using the standard error of the fit as per (2.5.34)

$$s_m = s_y\sqrt{\frac{n}{D}};\quad s_b = s_y\sqrt{\frac{\sum x_i^2}{D}};\quad s_{mb} = -s_y^2\frac{n\bar{x}}{D}. \tag{2.5.34}$$

The last quantity in (2.5.34) is the covariance of the slope and the intercept. The uncertainty at a given strain *x* is calculated by propagating uncertainties (2.5.35)

$$s_x = \frac{s_y}{|m|}\sqrt{\frac{1}{k}+\frac{x^2 n}{D}+\frac{\sum x_i^2}{D}-\frac{2x\sum x_i}{D}} \tag{2.5.35}$$

where most of the quantities have been defined before except for *k*, the number of repeat measurements for a single (x,y) data pair. The strain larger than the uncertainty at this strain is given by x_c:

$$x_C = ts_x \tag{2.5.36}$$

Squaring both sides of this equation and solving the resultant quadratic equation yields

$$\begin{aligned} x_{LOD} = 2x_C &= \frac{2ts_y}{nt^2 s_y^2 - Dm^2} \\ &\times\left(ts_y\sum x_i - \sqrt{\frac{D^2m^2}{k}+Dm^2\sum x_i^2 - n\frac{D}{k}t^2 s_y^2 - Dt^2 s_y^2}\right). \end{aligned} \tag{2.5.37}$$

and therefore, the quantity of the "limit of detection" – or, better, the lowest resolvable strain measurement – can be singularly determined from previously calculated fit parameters, the standard error on the fit, the determinant, and the sample size. For experiments in which the fibre tether length was only few meters, this value is x_{LOD} = 50 $n\varepsilon$.

We determine the maximum frequency of modulation and the rate of change of strain using a frequency sweep, as shown in Figure 13. In this experiment, 20 V (1.67 $\mu\varepsilon$) peak-to-peak voltage was applied to the piezoelectric transducer and the sinusoidal driving frequency was changed from 0.5 Hz to 370 Hz using 0.5, 1, 2 and 10 Hz data points to sample the initial sharp rise behavior and 30 Hz increments after. The maximum rate of change of strain can thus be calculated from this unlocking point as per (2.5.26), giving 3.6 $m\varepsilon / s$.

In the past extending the tether length has been problematic due to power-dependent Stimulated Brillouin Scattering. As per [24], SBS is a nonlinear process that involves the interactions between acoustic phonons and the photons. As light propagates in optical fibres, some of it interacts with the thermally excited acoustic phonons (waves) and is reflected. The interference of the reflected light with the incident light results in a reinforcement of the acoustic wave buildup and the reflected power, and eventually leads to clamping of the propagated power. Previous work from our group has seen the tether length limited to 10 km due to these issues. We therefore choose to keep the power level below the SBS threshold (2.5.38)

$$P_{th,SBS} = \frac{21A_{eff}}{g_B L_{eff}} \tag{2.5.38}$$

where $g_B = 5\times10^{-11} m/W$, $A_{eff} \sim 85\times10^{-12} m^2$, and L_{eff} is given by

$$L_{eff} = \frac{1-\exp(-\alpha L)}{\alpha} \tag{2.5.39}$$

and is approximately 18 km for a 50 km fibre link with 0.2 dB/km attenuation. In (2.5.38), we define the effective area of the SMF as A_{eff}, g_B is the Brillouin gain, and L_{eff} is the effective length of the SMF. As a result, the SBS threshold is approximately 2 mW for a 50 km fibre link. We keep our launched power below this level using fixed attenuators for our experiments and, for the long-tether applications, boost it in the return leg using an erbium-doped fibre amplifier (EDFA) in front of the detector.

Applications of strain sensors for remote detection of earthquakes or the stability of infrastructure requires extending the tether length to tens of kilometers. We choose the approach of passive sensing where the laser source and the control electronics are on a platform next to the nearest power outlet ashore while the sensor

head itself is entirely passive and can be placed at a remote location near a fault line. To this end, we have performed out calibration and frequency-dependent unlocking experiments with 25- and 50-km tether lengths.

Figure 14 shows the same calibration step as described above but for a tether length of 25 km, with a strain sensitivity of 11.74 $mV / \mu\varepsilon$ and an unlocking frequency of 160 Hz as per Figure 15 for the same strain applied as per Figure 13. The maximum rate of strain change is then 1.4 $m\varepsilon / s$**.** The limit of detection is 40 $n\varepsilon$ for this experiment. Similarly, Figure 16 shows the calibration done at a tether length of 50 km and sees a sensitivity of 11.47 $mV / \mu\varepsilon$ and an unlocking frequency of 100 Hz based on Figure 17, for an applied strain of 1.67 $\mu\varepsilon$. The maximum rate of strain change is 0.7 $m\varepsilon / s$**.** Table 1 shows the results from the linear fits in the figures mentioned above. The unlock frequency decreases as a function of tether length. This is expected and due to two main reasons. First, due to attenuation it is much more difficult to obtain a good error signal at longer tether lengths. Second, the optical delay of the return signal place an upper limit on the unlock frequency. The transmission delay is 167 μs for 50 km of round-trip travel in a 25 km fibre tether, and 333 μs for a 50 km tether.

Table 1. Results from the strain sensitivity calibration experiments. Errors on the fit parameters are shown and are derived via the treatment covered in 2.5.3. Systematic errors such as errors in the equations and the parameters that determine strain are not included in this calculation and might explain the discrepancy between the experimental and calculated values for the strain sensitivity.

Tether length (km)	0	25	50
Slope $(mV / \mu\varepsilon)$	11.63 ± 0.07	11.74 ± 0.06	11.47 ± 0.11
Y-intercept (mV)	-0.15 ± 0.10	-0.15 ± 0.08	-0.02 ± 0.16
R-squared	1.00	1.00	1.00
Travel time (μs)	<0.01	167	333
Unlock frequency (Hz)	350	160	100

Maximum rate of strain change $(m\varepsilon / s)$	3.6	1.4	0.7
Resolution limit $(n\varepsilon)$	50	40	60

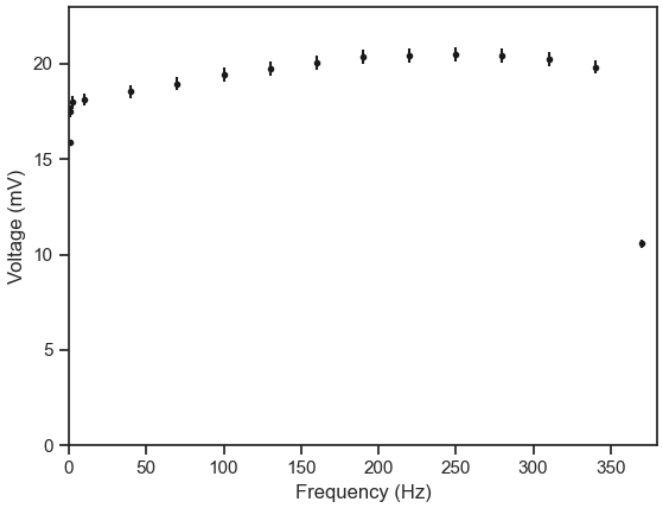

Figure 13. Frequency response of the strain sensor for 0 km fibre tether, V_{pp}=20V.

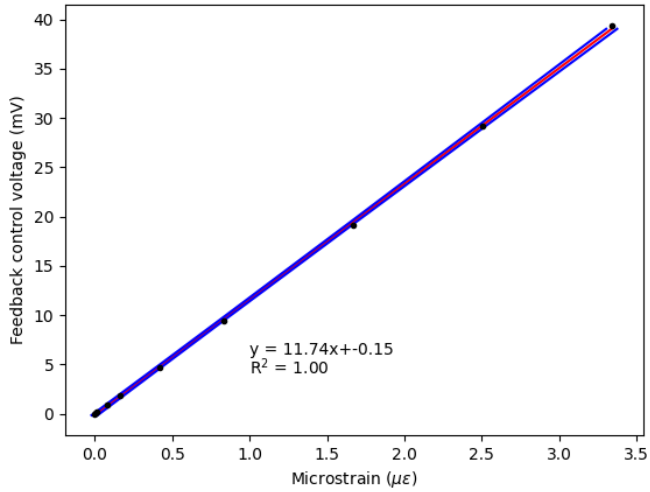

Figure 14. Strain sensitivity calibration at 10 Hz modulation for 25 km fibre tether.

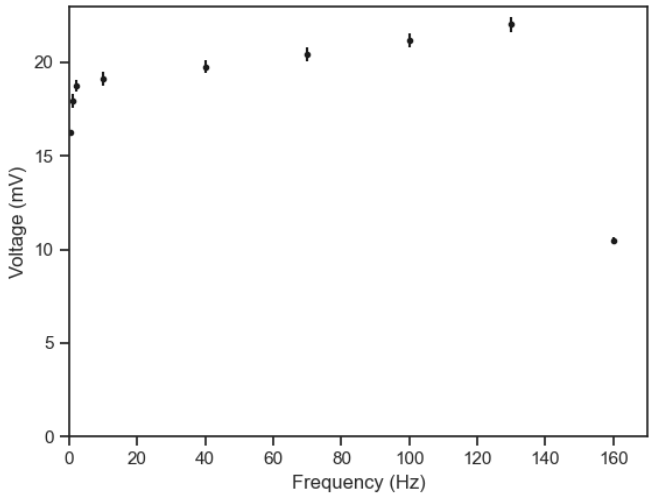

Figure 15. Frequency response of the strain sensor for 25 km fibre tether, V_{pp}=20V.

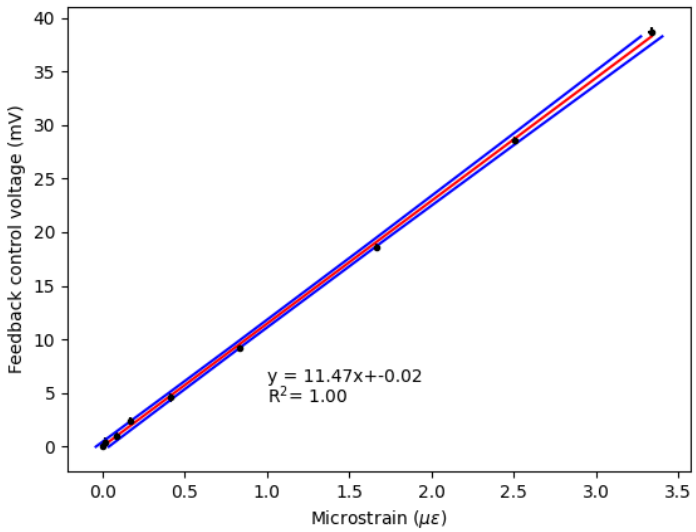

Figure 16. Strain sensitivity calibration at 10 Hz modulation for 50 km fibre tether.

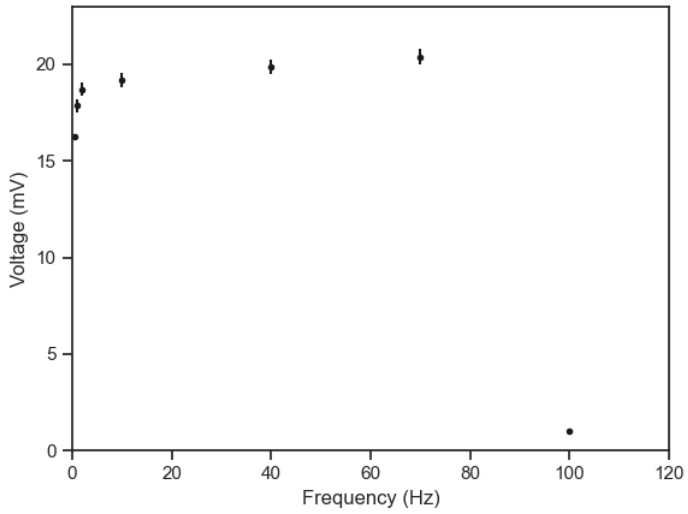

Figure 17. Frequency response of the strain sensor for 50 km fibre tether, V_{pp} = 20 V.

The measurements shown in Figure 12-Figure 17 have all been performed using lock-in detection. This method requires *a priori* knowledge of the acoustic signal frequency to allow for the extraction of same-frequency components. In actual seismic detection, there are several frequencies that would need to be detected with little knowledge of the exact values for the frequencies themselves. As a result, the collection of data from the time series of the signal is more appropriate. In our experiments this was based on detection based using an oscilloscope trace. An analysis of signal-to-noise ratio can be done based on these traces in Figure 18. In these figures, the sinusoidal feedback control voltage is shown in blue with a red fit overlaid. The black trace is the residual difference between the fit and the data, indicating the noise level for each driving voltage, where the driving voltage ranges from 0.05 V to 1 V. Of note is the fact that the total applied voltage is 20 times this driving voltage as it goes through an amplifier (1-20 V total applied voltage). Figure 18 indicates that the signal-to-noise of 1:1 is exceeded for a driving voltage of 0.3 V (6 V after amplification), so the minimum distinguishable strain value is 0.5 $\mu\varepsilon$ (500 $n\varepsilon$). This is an order of magnitude larger

than the 50 $n\varepsilon$ found through the lock-in measurements. The result is not surprising as one would expect that homodyne detection greatly reduces out-of-phase noise. Regardless, as a frequency-agnostic method of detection this method has particular trade-offs that need to be considered depending on the application. Moreover, the method of determining the LOD from signal-to-noise ratio is only good for an order-of-magnitude estimate.

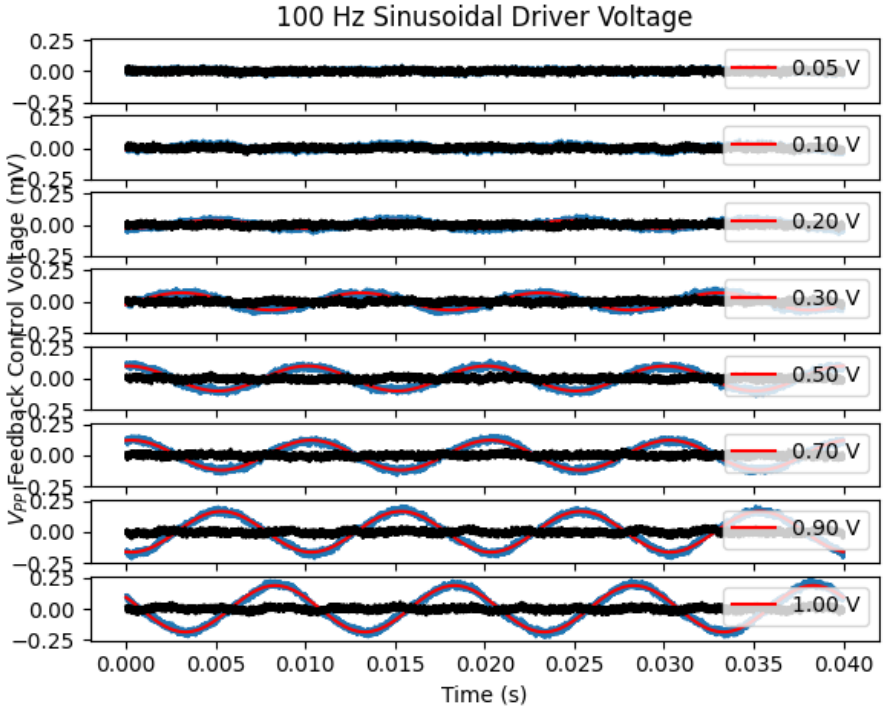

Figure 18. Oscilloscope traces for the feedback control voltage as a function of piezo driving voltage.

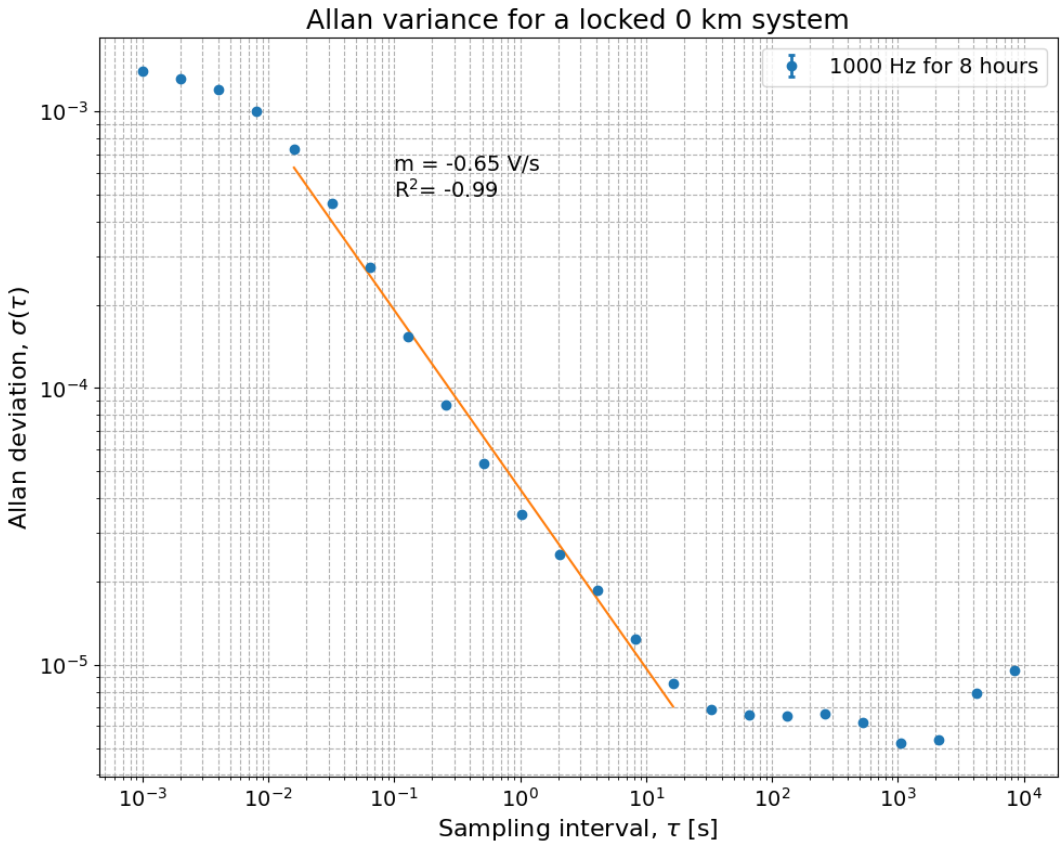

Figure 19. Allan variance for the frequency stability of the π -FBG.

In an effort to quantify frequency stability in our oscillator, we have performed Allan variance noise measurements in which we observe the frequency stability of our locked system (with no tether) over the course of 8 hours at a sampling rate (1000 Hz) faster than twice the highest frequency (350 Hz) at which the locked system can be driven, according to Nyquist's Theorem. The acquisition time is limited by the data acquisition system (DAQ). In this experiment, the feedback control voltage to keep the lock stable is sampled at 1000 Hz intervals, and the Allan variance σ_y is computed according to (2.5.40) from adjacent data points y_n, y_{n+1} or from two-step look-ahead from the x values.

$$\sigma_y(\tau) = \frac{1}{2}\left\langle (\bar{y}_{n+1} - \bar{y}_n)^2 \right\rangle = \frac{1}{2\tau^2}\left\langle (x_{n+2} - 2x_{n+1} + x_n)^2 \right\rangle \qquad (2.5.40)$$

Allan variance typically captures noise that has spectrally different origins. Traditional statistical tools such as the standard deviation are divergent for a time series with 1/f noise, also known as "pink noise"[25]. This can be seen readily upon inspection of the equation (2.5.41)

$$\sigma^2 = \frac{1}{\pi}\int_0^\infty S(\omega)d\omega \tag{2.5.41}$$

where $S(\omega)$ is a power spectral density that scales as 1/f. The integral then diverges at both limits barring the use of filtering on both ends of the spectrum.

Figure 19 then shows the Allan variance for a locked system with no tether. According to our findings, the noise is closest to being spectrally uniform white noise[25] with a variance slope of -0.65, 30% off from an ideal white noise slope of -0.5. The source of this error margin can likely be attributed to a poor-quality lock resulting from the large linewidth devices. We use the Allan deviation to solely determine the nature of noise present in our locking system, and not to inform averaging window sizes due to the nature of the short-lived oscillations that make up seismic disturbances.

2.6. Conclusions and Future Work

This work outlines the basic operating principle and some metrics related to π-shifted fibre-Bragg gratings used as strain sensors. The strain sensitivity, the frequency range of operation, the limit of absolute detection and the maximum rate of change of strain have been outlined for the bare sensor as well as two other tether lengths. The length of the tether has been extended from 10 km to 50 km, and the sensor itself has been changed to avoid polarization-related peak-splitting issues. A reliable lock has been achieved with this architecture. Since the linewidth of the π-FBG resonance is 25 times larger than that of the FP-FBGs previously used in our group [16], the limit of detection is correspondingly much larger for these new types of sensors (50 $n\varepsilon$ for π-FBG, 1 $n\varepsilon$ for FFP-FBG), and certainly are not at the limit of detection achieved compared to other groups ($p\varepsilon$)[4,9]. The frequency range of operation is also more

limited, possibly due to the same underlying issue of having obtained a looser lock with the larger-linewidth structure. The absolute bandwidth is also limited to 0 - 100 Hz in the worst-case scenario (50 km tether, Figure 17), which is sufficient in the detection of seismic waves in the field as the shakes typically happen at infrasound frequencies (< 20 Hz, e.g., 0.01-10 Hz[26]) and the audible ones oscillate at 5 - 60 Hz[27]. However, the fundamental limit posed by 100 km of round-trip fibre is 3 kHz. Mechanically isolating the piezoelectric ring from external vibrations is also of importance in experiments with frequency sweep and noise stability and is recommended as a future step. Interestingly, the experimental system sensitivity of 11.47-11.73 $mV / \mu\varepsilon$ is up to 40 % higher than the calculated value (7.30 $mV / \mu\varepsilon$)possibly due to an inaccurate transfer function, inaccuracy of the material parameters in calculating strain, or – more fundamentally - owing to a poor-quality lock resulting from the large width of the π -FBG resonance line. We strongly suggest the use of a narrower linewidth FBG (either π -FBG or FFP-FBG) that is still able to tolerate polarization-dependent peak splits within its linewidth. An additional gain in lock stability may be made by modulating the laser in the fast-modulation scheme according to Pound-Drever-Hall theory, which presents a steeper zero-crossing in the fast-modulation regime as seen in Figure 8.

The issue of noise remains relevant in the present system and is currently circumvented using an erbium-doped fibre amplifier inserted on the return trip to boost the signal so that a high-quality error signal can be generated from the amplified reflection spectrum. It is important to note that this solution to overcome the Stimulated Brillouin Scattering can be used with any type of FBG sensor. Alternative methods such as heterodyning a weak reflected signal with a strong synthetic signal to create a beat frequency, which can then be frequency-doubled. This process allows for the amplification of the original signal proportionally to the local oscillator power, and the ratio of the balanced-to-regular photodiode responsivities[28].

Noise analysis/stability of the lock, booting in noisy environments and temperature stability have not yet been characterized for our sensor. The first one can be extracted by locking the sensor to the cavity and obtaining the control voltage output

at several intervals to generate Allan variance plots as has been done previously[16]. The second is a measure of locking or re-locking ability when the sensor is placed in a noisy environment such as the bottom of a body of water. For this experiment, the piezo could be driven at a low frequency and the amplitude of the driving voltage to the piezo could be incrementally increased until a lock can no longer be achieved. Finally, the temperature is a confounding factor in strain measurements as the system can expand or shrink independently of the applied voltage as a function of the ambient temperature. To characterize and control for this, I suggest mounting the PZT tube either on a Peltier stage or using an environmental control chamber. The system can then be heated or cooled in a regulated way, paving the way to temperature calibration curves demonstrating the control voltage as a function of ambient temperature change in either direction. Furthermore, common-mode rejection can be used to delineate temperature fluctuation effects from the strain response. By using an external sensor exclusively sensitive to temperature, once can record and later reject the fluctuations common to both the π-FBG and the temperature sensor. It is also possible to use machine learning algorithms such as neural networks to post-hoc distinguish the temperature effects from the strain response of the π-FBG. These measurements may help us understand the influence of temperature variations on the instrument specifications, but neither method can be deployed in field applications. Since temperature changes occur on much longer timescales compared to the acoustic and even most infrasonic applications, they should be easily distinguishable by data post-processing.

The fiber strain sensor is only one of the elements of a seismic sensor system; other components include the transducer that converts the motion of the seafloor into strain on the fiber optic cable as well as a robust and corrosion-resistant package for the sensor head and the fiber optic cable. Both the transducers and packaging already exist for seafloor deployment. One-axis and three-axis accelerometers are most frequently used and are either microchip-based or PZT-based. It is likely that their design may be used as a starting point for a fiber-based sensor head.

Earthquake localization is an area of active research, with a number of localization methods available depending on the infrastructure available. Most notably, there is the possibility of using three component-sensing at a single station location, or using three different stations to triangulate the epicentre[29]. In the first of these methods, seismic activity along the three Cartesian spatial directions is recorded using three separate sensor heads aligned with the North-South horizontal, East-West horizontal, and vertical directions[30]. This information allows one to calculate the epicentre location, and can be used in conjunction with an array of stations for more rigorous localization[30]. In the latter method, however, at least 3 stations must be available to draw circles centred at the stations, and an intersection of the three can be found using the “circle and chord” method[29]. In both cases, a minimum of multiple sensor heads is required for a 3D picture of the activity.

Chapter 3 Critical Analysis of Fibre Interferometry

3.1. Interferometry

Interferometers are tools of measurement that typically split the intensity of a coherent light source into two different optical paths. As the light traveling in these two arms is recombined, the two waves interfere to create an interferogram whose properties depend on the difference between the interferometer arms' optical path lengths. The *Optical Path Length (OPL)* (3.1.1) depends on, both, the actual length of propagation in each of the interferometer arms as well as the effective refractive index that the propagated light experiences in each of the arms.

$$OPL = \int_C nds \tag{3.1.1}$$

As the interference pattern is sensitive to the optical length of the arms, slight variations in the optical path will reflect in the output signal. In other words, one can deduce the variation in the optical path length from the changes to the interference fringes. These variations can be caused by small refractive index changes or by length changes in one (or both) of the interferometer's arms. Since length variations that are considerably smaller than the wavelength of the interrogation light will cause measurable changes in the fringe pattern, interferometers are commonly used and are very sensitive tools for optical path length measurements. They found applications ranging from the microscopic (nanoscale optical profiling of surfaces) to the macroscopic (detection of gravitational waves). In the following paragraphs I introduce the most common classes of interferometers, before describing how they can be modified for measurements of refractive index in waveguides.

3.1.1 Mach-Zehnder Interferometers

Mach-Zehnder interferometers make use of two beam splitters (BS in Figure 20) to first split the incident intensity of light into two beams that are later recombined. The two mirrors (M in Figure 20) in the interferometer provide redirection of the light

toward the exit beam splitter. In a Mach-Zehnder interferometer the optical paths are traversed only once.

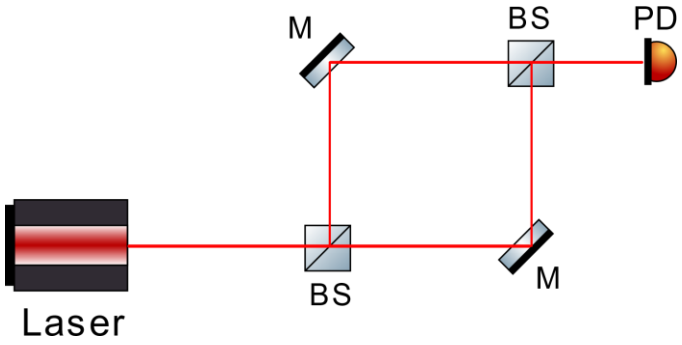

Figure 20. Schematic of a free-space Mach-Zehnder interferometer.

3.1.2 Michelson Interferometers

A Michelson interferometer is comprised of a light source, a single beam splitter, and two mirrors to reflect the light that split into two arms. Light incident from the source is split into two paths terminated in mirrors. Both beams are then recombined at the same beam splitter, and an interference pattern is created. In this configuration, the paths are traversed twice by each beam. Mach Zehnder-Interferometers and Michelson Interferometers can either be “balanced”, i.e., the two interferometer arms have the same physical length, or they can be unbalanced (not shown), if the two arms have different lengths.

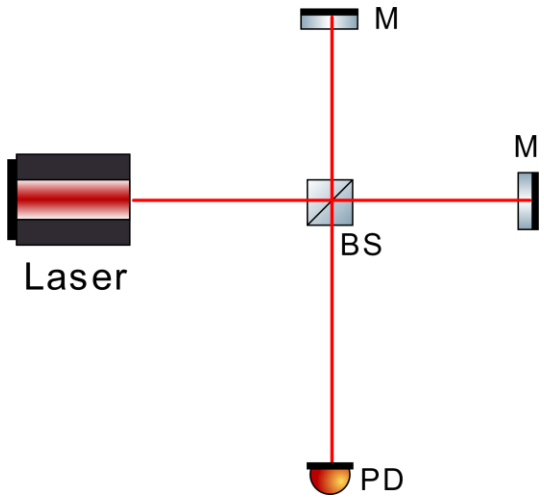

Figure 21. Schematic of a free-space Michelson interferometer.

3.1.3 Fabry-Pérot Interferometers

Fabry-Pérot interferometers are based on etalons or optical cavities that are made up of a pair of partially reflecting mirrors that can trap light and cause it to reflect multiple times at each interface. In resonance condition, the electromagnetic radiation reflected from the input mirror interferes destructively with the incident beam and there is no back-reflection. In contrast, the beam that is propagating forward is entirely transmitted, and substantial power circulates in the cavity.

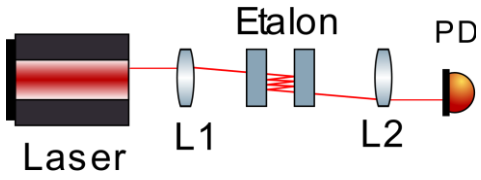

Figure 22. Schematic of a free-space Fabry-Pérot interferometer.

3.1.4 Sagnac Interferometers

In a Sagnac interferometer light split into two paths by a beam splitter (BS in Figure 23) traverses the interferometer in opposite directions and interfere at the point of recombination (BS). Rotation of the system translates to a longer path difference and

a relatively larger phase shift in one arm compared to the other and causes a shift in the interferogram (*Sagnac effect)*. As these interferometers are sensitive to rotation, they have found use as gyroscopes in a number of applications. Similar to Mach Zehnder-Interferometers (and in contrast to Michelson interferometers) light traverses each arm only once. In contrast to Mach Zehnder-interferometers and Michelson interferometers, the two light paths in a Sagnac Interferometer travel through the same medium and therefore always have the exact same physical length, i.e., a Sagnac interferometer is inherently "balanced".

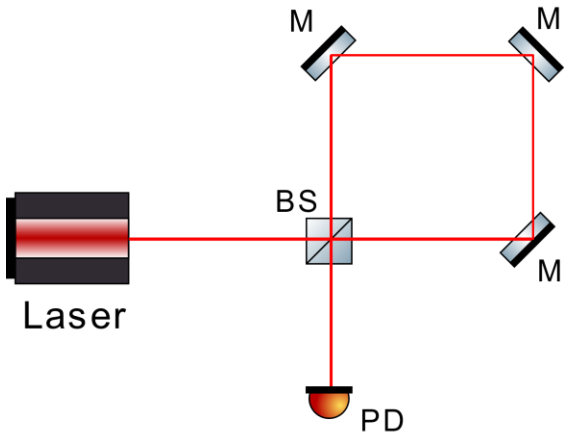

Figure 23. Schematic of a free-space Sagnac interferometer.

3.2. Fibre-Optic Interferometers

The human eye can easily detect small changes in the refractive index. For example, a mirage, an optical illusion that creates the appearance of water puddles on a hot road surface, is created by a refractive index (RI) difference of only $\Delta n = 2\text{-}3 \times 10^{-5}$ (20-30 ppm) between the hot air above the asphalt surface and the cooler air above it[31]. Schlieren images and scintillation are optical phenomena based on similarly small RI differences and are easily observable by the naked eye in both gases and liquids. It may then appear surprising that measuring *absolute* RI with the required accuracy is, in fact, quite difficult. Since every material and gas has an RI, the absolute index of a material

cannot typically be measured in isolation -- in an instrument, one would also have to know the RI of other optical components. Additionally, the RI depends on temperature, strain, pressure (or density), wavelength, and naturally on the composition of the material. Even though RI sensors for liquids and gases that can identify a *change* in the RI of 0.01 ppm have been built, absolute measurements with that accuracy are only available for a few select gases -- notably, the constituent gases of air. Depending on the wavelength, the absolute RI of most liquids is known only to within 100 ppm. In the near-infrared region, where many of the devices subject to this review operate, the RI of even common liquids have been reported to an accuracy of better than about 500 ppm only in 2016 [32]. Accordingly, very few, if any, instruments reviewed in this contribution are capable of absolute measurements leading to improved refractive index values for liquids or gases, but they instead report small changes of refractive indices.

Among the RI sensor platforms, those based on in-fibre interferometry take a special place, since many of them can be easily and inexpensively fabricated. In the last two decades many groups have built in-fibre interferometers based on a large variety of designs. From 2008-2020 alone, several hundred articles that describe the performances of various in-fibre interferometers and fibre-cavity based sensors have been published. Many research teams assessed their performance in determining the RI of liquids, or, more commonly, their ability to detect *changes* in the RI. These interferometer designs fall into three major groups. The most prevalent designs are based either on the Michelson interferometer (MI) and the closely related fibre loop mirror interferometer,

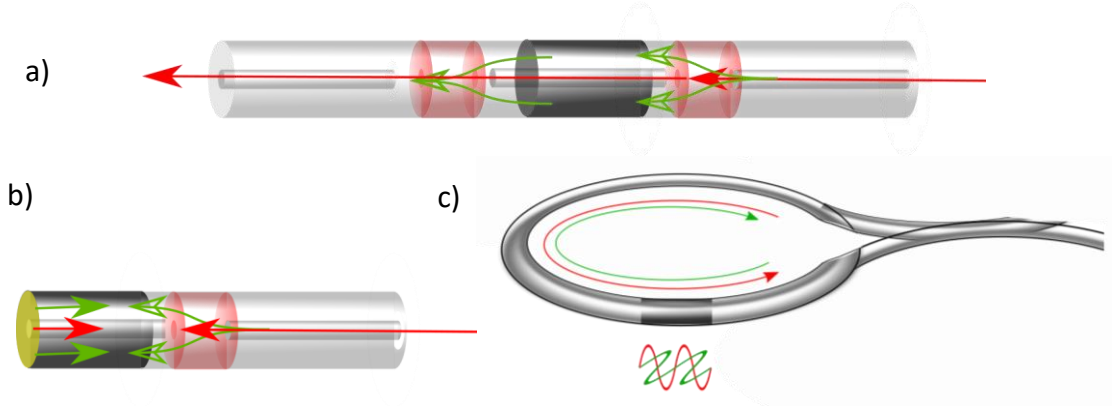

Figure 24: Schematic drawing of (a) the Fiber Mach-Zehnder interferometer (b) the Fiber-Michelson interferometer and (c) the Fiber loop mirror. Regions where an incoming propagated mode is split into two or more modes are indicated in red. The sensing region where one or both modes interact with an external analyte is given in dark grey, and a fiber mirror is shown as a yellow disk.

or on the Mach-Zehnder interferometer (MZI). In these interferometers, one of the interferometer arms is typically the core of the fibre waveguide and the other arm consists of the cladding material which propagates one or more cladding modes [33,34,35]. In these in-fibre interferometers, a coupler splits the incoming core mode into two (groups of) modes. In the Mach-Zehnder configuration, a second coupler which is typically identical to the first coupler then combines these two co-propagating modes into a single mode. In the Michelson configuration, by contrast, a retroreflector doubles the interaction length, and the recombination occurs at the same coupler.

Sagnac interferometers are even easier constructed. They can be made using a single 50:50 coupler (3 dB fiber coupler) where the two tethers between the laser and detector are connected to form a loop. Since Sagnac interferometers are inherently balanced and the light travels through the exact same fiber, albeit in opposite directions, any optical pathlength difference will have to be generated by birefringence or other polarization-dependent phenomena. Finally, a fourth design is based on the fibre Fabry-Pérot (FFP) cavity as shown in Figure 25**.** FFPs consist typically of two reflecting elements separated by a either waveguide or by a small gap in a waveguide. The light circulating in the cavity interacts with the sample. Therefore, the optical cavity resonances shift in wavelength reflecting a change in the sample's RI. This change may be brought on by interactions with the evanescent wave, changing dimensions of the resonator, or through other transduction mechanisms. Resonant ring cavities operate based on the same mechanism and are here discussed together with fibre cavity sensors. The can be made with one or two fiber couplers, which have a large split ratio (99:1).

Many of the devices discussed below were already subjected to a thorough review [36]. The previous review has a much larger scope than the present work and contains a comparative analysis of many different classes of plasmonic and photonic refractive index sensors such as surface plasmon resonance spectrometers, sensors based on nanohole arrays and local plasmonic structures, photonic crystals, whispering gallery mode resonators and dielectric (Bloch wave) refractive index sensors. Intrinsic

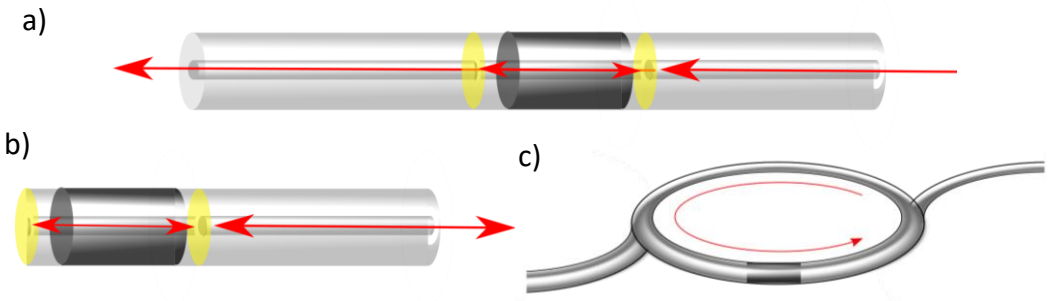

Figure 25: Schematic drawing of (a) the Fiber Fabry-Perot Cavity – in transmission (b) the Fiber-Fabry-Perot cavity in reflection, and (c) the Fiber ring-cavity.

fibre-optic devices such as regular and tilted fibre Bragg gratings, long-period gratings, and of course, fibre interferometers were discussed in some detail. The reader is referred to this review for an introduction into the field of spectroscopic refractive index sensing and a detailed discussion of the last 10 years of progress. Their list of devices was obtained from 500+ references and provide, likely, the most comprehensive comparative analysis available today. In addition, several recent reviews exist on the subclasses of these sensors, such as localized surface plasmon resonance sensors [37], optical biosensors based on plasmonic nanostructures[36], and photonic crystal[38,39] and other micro-structured[40] fibre sensors. Of particular relevance is a recent review on the (bio)chemical sensing applications of fibre gratings[41].

In this review, we select a particular class of similar spectrometric refractive index sensors -- fibre-optic based interferometers – which were identified as having high sensitivity and large figure of merit. Several of the devices were recently discussed and compared in the excellent 2019 comprehensive review [42]. Following the approach by several research groups[36,37,42,43], we adopt the figure of merit, *FoM*, and the sensitivity of the refractive index measurement, *S*, as the two most meaningful metrics when comparing the performance of these devices. In contrast to all previous reviews, we derive approximate analytical expressions for the *FoM* and the sensitivity based on the design parameters and an overlap parameter, *f*. The latter is a parameter that describes the difference of the mode field overlaps of the two propagated modes with the sample medium in each of the interferometer arms. We introduced this parameter, *f*, in a previous article [44] and found it useful when comparing devices. As such, this quantitative analysis allows us to relate many of the device performance characteristics directly to the dimensions and the design of a given device. Our comparative analysis then provides a clear path forward towards more reliable, more sensitive, and more accurate devices.

Finally, we emphasize that we only consider *spectroscopic* approaches to refractive index measurements, i.e., when a refractive index change results in a change of phase or resonant wavelength. Many more articles describe RI sensors that are,

instead, based on intensity measurements, frequently correlating the refractive index to a reflected or transmitted intensity on a logarithmic (decibel, dB) scale. These measurements do not lend themselves to a design analysis as presented here and are therefore excluded.

3.3. Fibre Interferometry Device Design

In a Mach-Zehnder Interferometer (MZI), the input light is split into two separate optical paths. Light travelling in the "sensing path" interacts with the environment in such a way that its optical phase is shifted with respect to the light in the "reference path". When these two beams are recombined after a single traversal, interference will result. Amplitude and frequency changes in the interference spectrum can be correlated to environmental changes and, after calibration, a sensor is obtained.

In fibre-based MZI, a multitude of different approaches have been developed to split and recombine the light within the device. The merit of these different approaches was discussed at length previously [42] and, therefore, only a brief overview is presented here.

Typically, light is introduced and collected via a single-mode optical fibre (SMF) where light is confined to the fibre core. This incident light must be partitioned between two or more optical paths and then recombined to generate the desired interference. In addition, the effective refractive index of at least one of these optical paths, n_{eff}, must be influenced by the sample over some interaction length, L.

Mode field mismatch is frequently used to partition light from the incident SMF core into two different propagation paths. For example, when a single-mode fibre is spliced to a fibre with different mode field characteristics, such as a multimode fibre, the incident light will be divided among the modes of the secondary sensing fibre at the splice boundary. Some light will continue to propagate in core modes, while other light will be transferred to cladding modes. Cladding modes have evanescent fields that extend into the surroundings and hence the effective index of these modes will be moderated by the external refractive index. This effective refractive index influences the

relative phase shift between the light in the core and the cladding regions of the sensing fibre. At the reverse transition splice boundary, where the multi-mode sensing fibre connects to a second single-mode fibre, a fraction of the higher-order modes re-couples to the SMF fundamental core mode where interference will occur. Such mode field mismatches have been created by transitioning from SMF to fibres with different core sizes. Examples may be transitions to thin-core fibre (TCF) [45], multi-mode fibre (MMF)[46], no-core fibre (NCF)[47], photonic crystal fibre (PCF)[48], and other micro-structured fibres (MSF)[49]. It is important to note that one can control the number of cladding modes excited only to some degree by virtue of adiabatic tapering and polarization-dependent coupling into the cladding modes.

One can also use another segment of SMF as the sensor head. For example, the core and the cladding modes of the sensing SMF can be simultaneously excited using an offset-splice SMF. In such a device, a segment of SMF is spliced to another segment of SMF and the two fibre cores are offset by a few microns [50] . The core mode of the input fibre thus irradiates both the core and cladding of the sensing fibre section. The recombination of the modes is achieved with a second core-offset splice [33,50].

Another method of transferring light between the core and cladding of a fibre involves two identical long-period gratings written in series. A long-period grating (LPG) is a structure consisting of a periodic refractive index modulation written into the core of a single-mode fibre. At wavelengths, $\lambda^{(m)}$, given by the relation:

$$\lambda^{(m)} = \left(n_{co} - n_{cl}^{(m)}\right)\Lambda = \left(\Delta n_{eff}^{(m)}\right)\Lambda \qquad (3.3.1)$$

light from the fibre core couples to a forward propagating cladding mode of order *m*.

In Equation (3.3.1) $\Delta n_{eff}^{(m)}$ is the difference in effective refractive index between the core and cladding mode with order *m*, and Λ is the grating periodicity [51]. The amount of light coupled from the core to cladding depends on the refractive index modulation depth of the grating. One LPG will couple light from the core to cladding, while the second guides light from the cladding back into the core. Interference

between the light that remains in the fibre core and the recoupled light causes transmission spectrum fringes to appear within each stop band of the LPG [52]. Since the wavelengths of the interference fringes depend on the effective RI of the cladding mode and given that the external RI affects the effective index, changes in the external RI shift the relative phase of the core and cladding modes and eventually the fringe wavelengths. The sensitivity to the external RI may be enhanced by tapering the fibre between the LPGs [53], or by reducing its diameter by etching, which extends the range of the evanescent field of the cladding modes [54].

An alternative method of transferring power between the core and the cladding modes is by using fibre tapers. For a straight bi-conical taper, the degree of coupling is a function of the taper length and waist diameter. These parameters must be optimized to achieve the optimum fringe contrast [55]. Additionally, abrupt bends in the fibre also couple core and cladding modes since the bending causes the light that would otherwise be incident at angles greater than the critical angle to escape into the cladding [56-58]. Spherical structures such as peanuts [59-61] or bulges [62-64], introduced into a fibre, have been shown to couple the fundamental core modes to higher-order cladding modes due to the abrupt change in the fibre structure. Such structures can easily be formed with a conventional fusion splicer. Spheres, for instance, might be easily formed at the end of an optical fibre by melting the fibre end in a fusion arc. The surface tension of the molten silica forms a spherical shape. The sensing portion of the interferometer can then be fused to this sphere. A second sphere re-couples the cladding and core modes, leading to modal interference in the output fibre. One can also fuse two spheres to form a ‘peanut’ shaped structure, which also serves as a mode coupler. Less pronounced bulges in fibre may be formed by gently compressing the fibre while the glass is softened [59].

Other forms of modal mixing can be achieved using laser machining [65-67] or reactive ion etching [68,65,69]. Using these techniques, a small cavity can be created in the fibre core. This disruption of the fibre core will cause a scattering of the core-mode light into cladding modes. In a similar vein, differential wet etching of the core and the

cladding will result in a depression forming in the core region of the fibre end [70]. If this etched fibre end is fused to a straight cleaved fibre, the resultant small air cavity will play the role of a mode coupler. Alternatively, a small bubble formed in the fibre core will serve the same purpose [71].

All these approaches allow the modes propagating in the core to interact with the modes propagating in the cladding. Similarly, a variety of options have been explored to let the light propagating in an interferometer arm to preferentially interact with the outside medium –usually a liquid, but solid films or gases have also been used as analytes. The most common mode-coupling elements are long tapers [72-74], abrupt tapers [66], or micro-fibres [75-77], in which the evanescent wave of the propagated light reaches far into the surrounding medium. Alternatively, hollow-core photonic crystal fibres and other hollow waveguides such as anti-resonant reflecting optical waveguides (ARROW) may be filled with an analyte to enhance interactions over a long propagation distance [44]. Especially when high order cladding modes are excited in the coupling region, it is also possible to probe the evanescent field interactions using a regular SMF. Finally, many researchers micro-fabricated notches [78], grooves [65] and gaps [79] into the interaction region to allow for maximal overlap of the propagated modes with the analyte.

3.4. Sensitivity, Accuracy, and Resolution

It appears as if there is some confusion in the literature about the terms "sensitivity of the measurement", "limit of detection", and "refractive index resolution". Of these, "sensitivity" is the easiest to understand as it is simply the slope of a linear calibration curve and is typically obtained from a linear fit of the sensor's response (usually a wavelength shift, $\Delta\lambda$) at different sample refractive indices, n_s .

$$S = \frac{d\Delta\lambda}{dn_s} \qquad (3.3.2)$$

In most articles, the sensitivity is given in units of nanometers per refractive index unit (nm/RIU). In general, the device sensitivity changes as a function of the sample refractive index. Since the response curve is then no longer linear, the sensitivity can only be approximated to be constant in a narrow refractive index range. In addition, the sensitivity is different for each interferometer fringe because of optical dispersion. In-fibre interferometers, therefore, have an inherently poorly specified sensitivity. For evanescent wave-based sensors, the sensitivity almost always increases as the refractive index of the sample approaches that of the waveguide material because of the evanescent wave extending well beyond the surface of the waveguide.

By contrast the "resolution" or "precision" of the refractive index measurement,

$$\Delta n_{\min} = \frac{\Delta\lambda_{\min}}{S} \qquad (3.3.3)$$

may be estimated from the inverse of the figure of merit, as is described below. The resolution limit in (3.3.3) typically assumes that a phase shift by $\pi/4$ is detectable with 99% certainty. In calculating the measurement resolution, it is therefore implied that the minimal detectable shift of an interferometer fringe, $\Delta\lambda_{\min}$ corresponds to one half of the fringe width $\Delta\lambda_{\min} = \lambda_{1/2}$. This is a conservative estimate, and several authors assume that they can measure phase changes much below that limit [80,81]. By inspecting the scatter of the calibration curves one can speculate by inspection that in many experiments the minimal detectable phase shift is, in fact, far better (lower) than $\pi/4$, which implies that wavelength shifts, $\Delta\lambda_{\min}$ of less than $\lambda_{1/2}$ are quantifiable. However, hardly any study quantifies the minimal resolvable phase shift or the minimal detectable wavelength shift, $\Delta\lambda_{\min}$, experimentally. We therefore use the Figure of Merit and implicitly $\Delta\lambda_{\min} = \lambda_{1/2}$ as an indicator for device performance, as explained in Section 3.5. It should be noted that it is, in fact, quite straightforward to accurately determine

the minimal detectable response of a sensor system, i.e., in this case, the minimal detectable refractive index change, $\Delta n_{\min}$ as per (3.3.4).

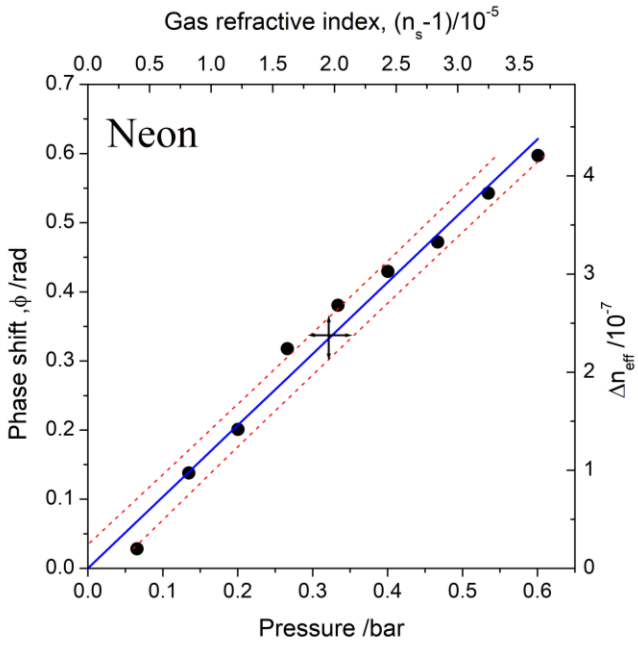

Figure 26. Calibration curve adapted from[44]. The circles are phase shift measurements obtained using a 30 cm bent hollow-core waveguide filled with neon at pressures between 0.075 and 0.6 bar. The refractive index of the sample gas, n_s, was calculated using the Lorentz-Lorenz equation and a polarizability of α_{Ne} = 0.44 ×10^{-40} J^{-1}C^{2}m^2. The slope of the linear fit is the sensitivity of the measurement, S. Similarly, the sensitivity coefficient f = 0.012 is obtained from the slope. The red dashed lines are the (95%) confidence intervals from which the lowest phase uncertainty is obtained as 2.3 ×10^{-3} rad (0.1°). This corresponds to an optimal uncertainty of the sample index of Δn_S = 3.5×10^{-6} RIU.

$$\Delta n_{\min} = \frac{1}{FOM} \qquad (3.3.4)$$

As is well known among analytical chemists, one can obtain the standard deviation of the wavelength shift measurement, $\Delta\lambda_{\min}$ in two different ways. IUPAC recommends

that one cycles between a blank (reference) solution and several *different* solutions, each containing an analyte near the detection limit for, at least, eight times, record the associated wavelength shift $\Delta\lambda$, and then determine the standard deviation of the wavelength measurement $\sigma(\Delta\lambda)$. The minimal resolvable wavelength shift is then $\Delta\lambda_{\min} = t\,\sigma(\Delta\lambda)$, where the Student's *t*-factor is typically approximated as $t = 3$ for a 99% confidence interval and $\sigma(\Delta\lambda)$ is the average uncertainty of the measurement. This method has been used less than 10 times in the 500+ studies that we reviewed. Alternatively, one may determine the average standard deviation of the wavelength shift measurement from a linear calibration curve. Assuming that *N* measurements were obtained at different and exactly known refractive indices, the standard deviation of the signal may be calculated from the ($\Delta\lambda_i, n_{s,i}$) data pairs, the sensitivity (slope), *S*, and the intercept, *b*, of a linear fit to the calibration curve as follows

$$\sigma(\Delta\lambda) = \sqrt{\frac{\sum_i \left(\Delta\lambda_i - S\,n_{s,i} - b\right)^2}{N-2}} \tag{3.3.5}$$

Again, the minimal resolvable wavelength shift is given by $\Delta\lambda_{\min} = t\sigma(\Delta\lambda)$. This method was also used less than 10 times in the reviewed work.

Note that the resolution calculated with (3.3.5) is only valid near the centre of the calibration range. Since confidence intervals diverge near both ends of the measurement range, this average value then overestimates the abilities of the instrument at the limits of the calibration range. Importantly, it is not possible to extrapolate the resolution limits beyond the calibration range, firstly because of the divergence of the confidence intervals, and secondly because one cannot assume the sensitivity, *S*, and intercept, *b*, in (3.3.5) to remain constant outside that range.

In the reviewed literature it is much more common to find an estimate of the precision (resolution) which is calculated from the spectral resolution of the optical spectrum analyzer, $\Delta\lambda_{OSA,\min}$, and the experimental sensitivity, *S*. This "resolution" or "detection limit" is frequently given as $\Delta\lambda_{OSA,\min} / S$. This is incorrect, as it assumes that

the slope and intercept of the calibration curve are completely free of error, i.e., the main uncertainties of the measurements are neglected. Trivially, this approximation fails if the calibration curve is even slightly non-linear. We therefore suspect that almost all reported resolution limits are rather optimistic guesses and recommend that they be ignored in future work.

When reporting the accuracy of the measurement, i.e., the reliability of the *absolute* values for the measured refractive index, one also must consider the accuracy with which the refractive indices of the calibration solutions are known. Quite recently, the refractive indices of many solvents and solutions (NaCl, sucrose) were determined at 1550 nm to within 100 ppm (10^{-4} RIU) [32]. Prior to this 2016 study, the uncertainty was much higher, and many researchers simply used refractive index values obtained at 589 nm instead of those at the measurement wavelength. This alone will give an error of typically larger than 1000 ppm (10^{-3} RIU). In addition, many authors appear to neglect that the refractive indices of liquids are not linearly additive. Even if one used the Lorentz-Lorenz equation and added the polarizability terms (which are proportional related to the $(n^2-1)/(n^2+2)$ terms) one would still have to consider the excess volumes of mixing and non-linear density relationships (see Appendix). Once these terms are accounted for, the Lorentz-Lorenz equation may be applied and produces values within 1% accuracy. The Lorentz-Lorenz model assumes linear additivity of the polarizabilities and then allows for a calculation of the refractive index [32].

Temperature fluctuations can also change the refractive index. For measurements on gases with a typical polarizability of $\alpha = 6.5 \times 10^{-40}$ the refractive index changes by about 3.5×10^{-6} /K. Liquids and solids have thermo-optic coefficients on the order of 10^{-5}/K. It is therefore difficult to perform measurements with an accuracy of better than 10^{-4} RIU, if the temperature of the sample and optical setup is not actively stabilized to be within 1 K.

All these effects conspire to produce non-linearity and scatter of points in the calibration curve, which are frequently found to deviate by more than 10^{-3} RIU from a linear fit.

3.5. Metrics for Interferometer Performance

Since we aim to compare an exceptionally large number of proposed designs, it is useful to define common metrics that capture the performance of different devices. To that end, two metrics are commonly used: (1) the sensitivity of the device, e.g., the wavelength shift of a cavity response peak or an interferometer fringe dependent on the external refractive index, and (2) the resolution that this sensitivity affords.

Both metrics are necessary but not sufficient to describe these devices. Consider that a high sensitivity can be achieved for short interferometers (and fibre cavities) when fringes are hundreds of nanometers in width. Only shifts by a few nanometers may then be distinguishable and the high sensitivity does not necessarily allow for a high measurement resolution. The same wavelength shift in a longer device that has much narrower fringes is easily observable. Instead of the sensitivity, we therefore use a Figure of Merit (*FoM*) derived from the ratio of sensitivity and peak width. The Figure of Merit then serves as a device characteristic that is independent of the interrogation instruments and helps assess the performance of the reported devices. Analytical expressions for the Figure of Merit and the sensitivity are derived in the following paragraphs. As mentioned above we disregard previously reported resolution limits since most of these reported values were obtained incorrectly by our estimation.

For a Michelson interferometer and a Mach-Zehnder interferometer, the accumulated optical phase shift in each arm depends on the length of the arms and the effective refractive index of the propagated mode(s) in each arm,

$$\phi_i = \frac{2\pi}{\lambda} n_i^{eff} L_i \qquad (3.4.1)$$

where n_i^{eff} is the phase index of the propagated mode, i, L_i is the geometrical length of the respective arm, and λ is the wavelength of light in vacuum. If only two modes (i = 1, 2) co-propagate, interference occurs when the two fields are coherently combined and give rise to a wavelength-dependent interferogram of intensity, I, as described in the literature[82,83]

$$I = I_1 + I_2 + 2\sqrt{I_1 I_2}\cos\left(\phi_1 - \phi_2\right) \qquad (3.4.2)$$

where I_1 and I_2 are the respective intensities and φ_1 and φ_2 are the phases of the co-propagating modes. The difference in the effective mode indices, Δn^{eff} is therefore proportional to the difference of the propagation phase $\Delta\varphi = \varphi_1 - \varphi_2$

$$\Delta n^{eff} = \frac{\lambda\Delta\phi}{2\pi L} \qquad (3.4.3)$$

Interference results from a differential phase shift accumulated by light traveling through alternate paths through the device. When used for refractive index sensing, fibre interferometers are designed in such a way that the effective index of at least one of the interfering modes is influenced by the refractive index of the environment. This is usually accomplished by a thinning of the fibre through tapering, etching, or micromachining of holes or grooves, allowing for enhanced evanescent mode penetration into the surroundings. In-fibre interferometers are inherently "balanced interferometers", i.e. the geometrical lengths (but not the optical paths) of the two arms are identical, $L = L_1 = L_2$, and the two arms expand and contract nearly identically with temperature and strain [84].

As was shown before [44] it is straightforward to derive the sensitivity with which an interferometer can measure the refractive index of a sample, n_s. The sensitivity of the phase shift measurement of the sample's refractive index depends on the extent with which either one of the two modes can interact with the sample medium. Previously, we defined a sensitivity coefficient f_i such that [44]

$$n_i^{eff} = \left(1 - f_i\right) n_i^w + f_i n_s \qquad (3.4.4)$$

In Eq. (3.4.4) we assume that the effective phase index in each arm, n_i^{eff}, is a weighted sum of the indices of the sample, $f_i\, n_s$, and the waveguide material $(1 - f_i) n_i^w$ nb. This implies that the sensitivity coefficient, f, is a measure for the fraction of guided light that interacts with the sample. The mode field distribution for a number of different modes are shown in Figure 27, which can be used to visualize the f number for different mode orders. If the shaded areas represent the evanescent field interaction with the

sample the lowest *f* numbers are expected from LP01 Gaussian modes as they would have the lowest overlap with the sample.

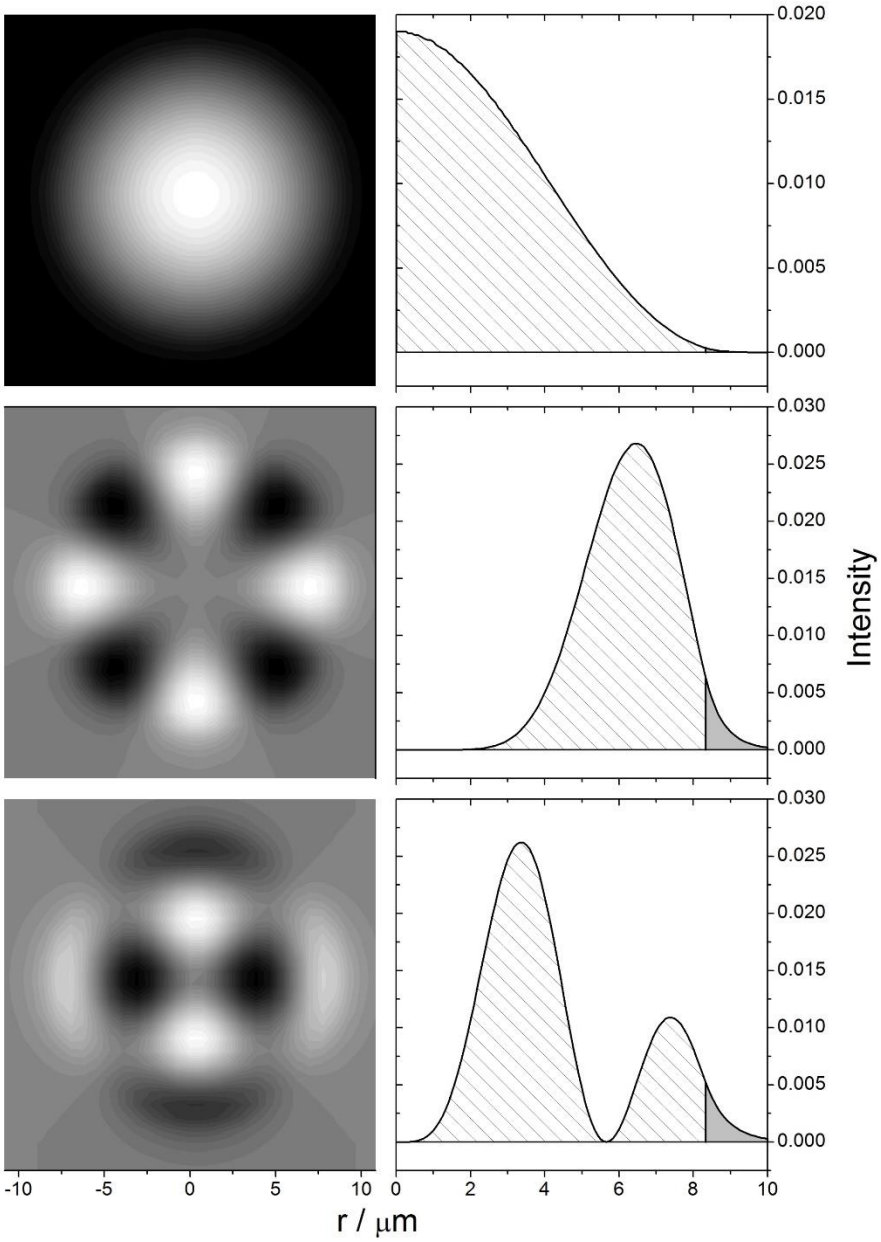

Figure 27. Contour plots of $\psi_{lm}(r,\theta)$ for the LP_{01}, LP_{41}, and LP_{22} modes in a cladding-less fiber waveguide (left panels from top) and the radial distribution of the associated intensity, ψ_{lm}^2, normalized to unity (right panels). The hatched fraction of the mode field resides inside the core of the fiber (n_{core} = 1.46242) whereas the shaded

portion is inside the cladding (n_{clad} = 1.45742). The fiber radius is assumed to be a = 8.335 μm and λ = 632 nm[85].

Equation (3.4.4) allows us to express the sensitivity of the phase measurement in terms of the relative interaction of the two modes with the sample as the derivative of (3.4.3):

$$\frac{d\Delta\phi}{dn_s} = \frac{2\pi L}{\lambda}\frac{d}{dn_s}\left(n_1^{eff} - n_2^{eff}\right) = \frac{2\pi L}{\lambda}\frac{d}{dn_s}\left(\left[\left(1-f_1\right)n_1^w + f_1 n_s\right] - \left[\left(1-f_2\right)n_2^w + f_2 n_s\right]\right)$$
$$= \frac{2\pi L}{\lambda}\left(f_1 - f_2\right) \qquad (3.4.5)$$

The sensitivity of the interferometer's phase measurement is therefore greatest, if light in one of the arms propagates only through the sample (f_1 = 1) and modes in the other arm remain fully contained in the waveguide (f_2 = 0). The sensitivity also increases linearly with the length of the interferometer arms, L, and with the inverse of the wavelength, λ.

Only the magnitude of the phase shift, $|\Delta\phi|$, can be measured experimentally. Since the sign of the phase is therefore arbitrary, we can set $f = |f_1 - f_2|$ and (3.4.5) can be written as

$$\frac{d\Delta\phi}{dn_s} = \frac{2\pi}{\lambda} f L \qquad (3.4.6)$$

In most previously reported works the sensitivity of the measurement is given as the wavelength shift associated with a selected fringe as a function of the sample's refractive index. The sensitivity is then the ratio of the wavelength shift, $d\lambda$, of an interferometer fringe (i.e., at constant $\Delta\phi$) and the change of the sample index, dn_s. The sensitivity is then best determined by taking the derivative of (3.4.3) but now with constant $\Delta\phi$,

$$S = \frac{d\lambda}{dn_s} = \frac{2\pi}{\Delta\phi} f L \qquad (3.4.7)$$

where for attenuation maxima

$$\Delta\phi = 2\pi\left(m+1/2\right) \tag{3.4.8}$$

with *m* being an integer. With (3.4.7) and (3.4.8) it is apparent that the sensitivity depends on the mode order of the interference fringe

$$S = \frac{fL}{m+1/2} \tag{3.4.9}$$

Fundamentally, it is therefore incorrect to characterize an interferometer by its sensitivity alone, since this sensitivity is different for each interference fringe as (3.4.9) clearly shows. This expression can of course also be used to determine the sensitivity coefficient, *f*, if the sensitivity, *S*, has been measured and *m* is known.

Finally, by substituting (3.4.3) into (3.4.6), we can give the sensitivity coefficient as

$$f = \frac{d\Delta n^{eff}}{dn_s} \tag{3.4.10}$$

This simple expression shows that the sensitivity coefficient, *f*, relates the change in sample index to the difference between the effective indices of the two propagated modes.

When two neighboring attenuation maxima at λ_1 and λ_2 are obtained from the interferogram, one can use Eqns. (3.4.8) and (3.4.3), to calculate difference in effective index:

$$\Delta n^{eff} = \frac{\lambda}{L}\left(m+1/2\right) \tag{3.4.11}$$

The mode number *m* differs by one between neighbouring peaks (assuming $\lambda_1 < \lambda_2$) such that

$$\lambda_1(m+1/2) = \lambda_2(m-1/2)$$
$$m = \frac{1}{2}\frac{\lambda_2+\lambda_1}{\lambda_2-\lambda_1} \tag{3.4.12}$$

where *m* is the larger mode number of the two adjacent peaks.

Equation (3.4.11) can then be expressed as

$$\Delta n^{eff} = \frac{\lambda}{L}\left(\frac{1}{2}\frac{\lambda_2+\lambda_1}{\lambda_2-\lambda_1}+\frac{1}{2}\right) \qquad (3.4.13)$$

where λ may be approximated by the average of λ_1 and λ_2. Similarly, the sensitivity coefficient is determined from (3.4.13) by taking the derivative of (3.4.10)

$$f = \frac{d\lambda}{dn_s}\frac{1}{\lambda L}\frac{1}{\lambda_1^{-1}-\lambda_2^{-1}} = \frac{S}{\lambda L}\frac{1}{\lambda_1^{-1}-\lambda_2^{-1}} \qquad (3.4.14)$$

Equation (3.4.9) illustrates that the sensitivity, *S*, of balanced fibre interferometers does not depend on the materials' refractive indices of either of the interferometer arms, but it does depend on how strongly the modes are interacting with the sample. For example, if the index of the sample liquid n_s is probed through the sample's interactions with the evanescent field of the cladding modes, the sensitivity coefficient *f* depends on the exponential decay length of the evanescent field. In fibre sensors where the sensing arm of the interferometer consists of the fibre cladding, the depth of the evanescent field (and therefore *f*) is related to the cladding mode number. This latter is associated with the total internal reflection angle in the ray picture of light. On the other hand, the depth of the evanescent field (d_{evan}) in the surrounding medium also depends on the refractive indices of the waveguide material, n_0 and that of the surrounding medium, n_s as per (3.4.15) [86].

$$d_{evan} = \frac{\lambda}{4\pi}\frac{1}{\sqrt{n_0^2 sin^2\theta - n_s^2}} \qquad (3.4.15)$$

where θ is the incident angle. These relations show that one cannot expect the sensitivity associated with a particular fringe to be constant over a large range of sample indices. Indeed, for almost all reported sensors the sensitivity increases as the sample index approaches that of the waveguide material.

In (3.4.9) the sensitivity depends linearly on the interaction length, *L*, and a naïve researcher may be prompted to increase the measurements' sensitivity by increasing the length of the interferometer arms. This is only effective if the propagated light in at least one of the arms interacts with the sample over its entire length. If the length of the

interaction region (e.g. a taper or a micromachined gap) remains fixed, *f* decreases as the arm length increases such that the product of the two, *f L,* and the sensitivity, *S*, remains constant in (3.4.9).

Importantly, the sensitivity, and the smallest detectable refractive index change, $\Delta n_{\min}$, in this approximation are independent on the type of couplers that are used. The sensitivity also does not depend on the fringe contrast which depends on the relative intensity of the modes, although low contrast may make it difficult to distinguish the interferometer fringes and thereby also reduces the reliability of the measurements.

Importantly, Eq. (3.4.9) shows that the route to high sensitivity measurements involves increasing the "effective interaction length", *fL*, i.e. a parameter that is related to the actual length of the interferometer arm and to the fraction of light that interacts with the sample.

Considering that the use of the sensitivity as a metric for the quality of a fibre sensor is fraught with problems, we propose to instead use the "figure of merit", *FoM*. The figure of merit is calculated as $FoM = S / \lambda_{1/2}$, i.e., as the ratio of the sensitivity and the half-width-at-half-maximum (HWHM) of the spectral feature, $\lambda_{1/2}$.

In optical resonators the linewidth, $\lambda_{1/2}$, of a cavity resonance is already frequently used to determine the *FoM*. In interferometers it would be most practical to use the halfwidth of an interference fringe, $\phi_{1/2} = \pi / 2$ which, can be combined with the sensitivity of the phase measurement in (3.4.6) to give the Figure of Merit as:

$$FoM = \frac{d\Delta\phi}{dn_s}\frac{1}{\phi_{1/2}} = \frac{4fL}{\lambda} \qquad (3.4.16)$$

The same equation is obtained when using the sensitivity, *S*, in (3.4.7) obtained from the wavelength shift at constant phase difference, $\Delta\phi$.

The half-width $\lambda_{1/2}$ corresponds to

$$\lambda_{1/2} = L\Delta n_{eff}\left(\frac{1}{m} - \frac{1}{m+1/4}\right) \approx \frac{L\Delta n_{eff}}{4m^2} = \frac{\lambda^2}{4L\Delta n_{eff}} \qquad (3.4.17)$$

where we rearranged (3.4.11)

$$\lambda = \frac{L\Delta n_{eff}}{m + 1/2}$$

(3.4.18)

and assumed that *m* is large. The Figure of Merit is therefore readily expressed in experimentally observable parameters

$$FoM = \frac{S}{\lambda_{1/2}} = \frac{4\,fL}{\lambda} \qquad (3.4.19)$$

where we combined (3.4.17) with (3.4.7) and (3.4.3) to derive (3.4.19).

Equation (3.4.19) shows that the *FoM* is related only to the effective interaction length, *fL*, and the operational wavelength, λ. Importantly, the mode number no longer affects the Figure of Merit as it does not enter the derivation of (3.4.19). Hence, the *FoM* is a characteristic of the instrument at a given operational wavelength range and does not depend on which of the interferometer fringes are used. We note that the sensitivity coefficient *f* for evanescent field sensors is dependent on the evanescent field length which in turn is dependent on both λ and n_s as discussed above and illustrated in (3.4.15).

An estimate for the minimum resolvable refractive index change, $\Delta n_{\min}$, is usually taken as the reciprocal of the *FoM* (see also (3.3.4))

$$\Delta n_{\min} = \frac{1}{FoM} = \frac{\lambda_{1/2}}{S} = \frac{\lambda}{4\,f\,L} \qquad (3.4.20)$$

The smallest resolvable index change, $\Delta n_{\min}$, by this calculation tends to be much larger than the values that are typically reported. A discussion of these differences is given below.

Finally, we note that the above points remain valid, if the spectra are Fourier transformed and instead of optical resonance frequency shifts and intensity changes, one records the Fourier transform of the interferograms in the form of inverse frequency (or inverse wavelength) and phase changes. In the best case, the Fourier transform occurs without loss of information and the Figure of Merit (or equivalently

the signal to noise ratio) is then not degraded. On the other hand, if several modes beat against a core mode or if the interferogram is noisy, Fourier filtering may help increase the signal-to-noise level and even the sensitivity of the measurement [87] [63].

3.6. Mathematical Treatment and Interpretation of Publications

3.6.1 Mach-Zehnder Interferometers and Michelson Interferometers

To compare the performance of single-pass Mach-Zehnder interferometers or double-pass Michelson interferometers we extract the values for the sensitivity coefficient, *f*, the effective interaction length, *fL,* and the figure of merit, *FoM*, from published spectra. All three parameters can be determined from the experimentally obtained sensitivity, *S,* and the difference in the effective index between the two interferometer arms, Δn_{eff} , which we calculate from published spectra as described below.

In the reviewed literature interference spectra are typically published on a logarithmic (dB or dBm) scale. From these spectra we can extract the modulation depth of the interferometer as

$$M = \frac{I_{\max} - I_{\min}}{I_{\max}} = 1 - 10^{0.1(dB_{\min} - dB_{\max})} \qquad (3.5.1)$$

Here, I_{max} and I_{min} refer to the maxima and minima of the signal on a linear scale, whereas dB_{max} and dB_{min} are the corresponding intensities on a logarithmic scale. Many articles provide two transmission maxima or minima for analysis. The wavelength difference between two neighbouring minima can be used with (3.4.3) and (3.4.12) to determine the effective index difference of the interfering modes.

$$\Delta n_{eff} = \left(L \left(\frac{1}{\lambda_1} - \frac{1}{\lambda_2} \right) \right)^{-1} \qquad (3.5.2)$$

In other articles only a small part of the spectrum is given. In these cases, a single fringe (“dip”) can be used for analysis. If the spectrum is given on a linear intensity scale,

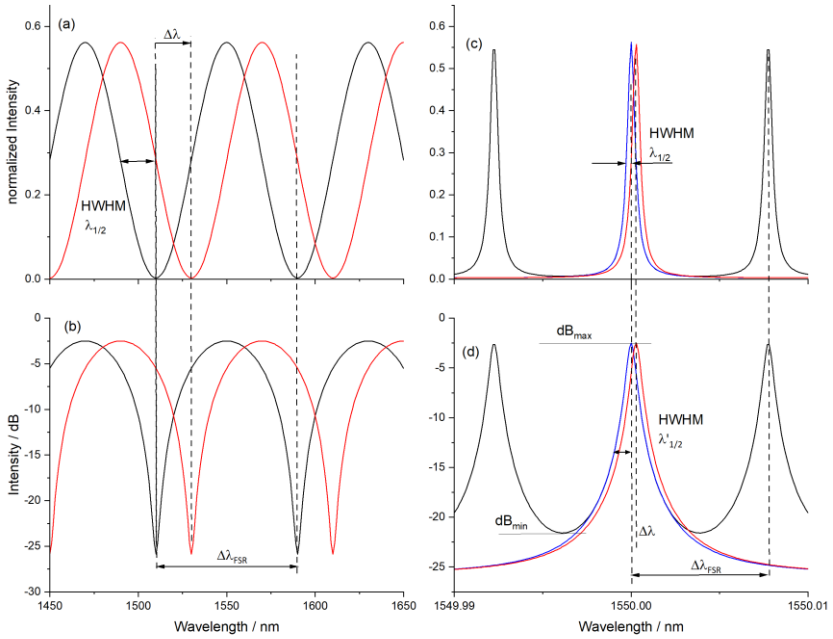

Figure 28: Synthetic spectra of a fiber interferometer (left) and a fiber cavity (right). Panels (b) and (d) display the spectra of (a) and (c) on a dB scale.

The blue curves in panel (c) and (d) are Lorentzian fits to the Airy-spectrum of the fiber cavity. The red curves illustrate a wavelength shift by one-half width at half-maximum (HWHM), $\lambda_{1/2}$.

the value Δn_{eff} can be obtained from the half-width-at-half-maximum (HWHM), $\lambda_{1/2}$, of the fringe given periodic fringes (as per Fig. 4a)

$$\Delta n_{eff} = \left(L \left(\frac{1}{\lambda_1} - \frac{1}{\lambda_1 + 4\lambda_{1/2}} \right) \right)^{-1} \qquad (3.5.3)$$

It is far more common, however, to find the spectrum displayed on a logarithmic (dB) scale. On this scale the HWHM of a fringe, $\lambda_{1/2}^{'}$, can be converted to the half-width-at-half-maximum (HWHM), $\lambda_{1/2}$ of the fringe on a linear scale using (7.4.4) or (7.4.8) in the Appendix:

$$\lambda_{1/2} = \frac{\pi}{2}\left(\lambda'_{1/2}\right)\left(\cos^{-1}\left(2M''-1\right)\right)^{-1} \qquad (3.5.4)$$

where the modulation depth is

$$M'' = \frac{10^{\left(dB\left[I_{\max}\right]+dB\left[I_{\min}\right]\right)/20} - 10^{dB\left(I_{\min}\right)/10}}{10^{dB\left(I_{\max}\right)/10} - 10^{dB\left(I_{\min}\right)/10}} \qquad (3.5.5)$$

With Δn_{eff} calculated either from two minima using (3.5.2), or from one dip using (3.5.3) and with the reported sensitivity, *S*, it is then straightforward to determine the sensitivity coefficient using (3.4.3) and (3.4.7)

$$f = \frac{S\Delta n_{eff}}{\lambda} \qquad (3.5.6)$$

We found that Δn_{eff} can vary by as much as a factor of 3 depending on whether it was derived from two adjacent fringe wavelengths or from the HWHM of a single fringe and the calculated value of *f* is therefore similarly affected. The variations are likely related to the neglect of dispersion effects in the calculation of (3.4.3) and (3.4.7), experimental inaccuracies, and our difficulty in obtaining values for HWHM from experimental spectra. When values for *f* differ, we use an average in our meta-analysis.

The above analysis applies for Michelson interferometers and Mach-Zehnder interferometers, with one difference. For Michelson interferometers the length *L* used to calculate the Figure of Merit in (3.4.19) and the effective index Δn_{eff} from (3.5.2) or (3.5.3) is twice the physical length of the probe.

3.6.2 Fibre Loop Mirrors and Sagnac Interferometers

Fibre loop mirrors and Sagnac interferometers are closely related to Michelson interferometers. A coupler splits the incoming mode into two beams which then counter-propagate before recombining at the same coupler. If the two beams accrue the same phase shift, the resulting interference will be perfectly constructive and 100% of the intensity will return to the light source. Any variation in phase, for example, due to rotation of the loop in an external rotating frame or due to birefringence, produces a phase difference and creates an interferogram, i.e., an intensity oscillation that depends both on the wavelength and the induced phase shift. One can interpret the effect of the

Sagnac loop in the context of equation (3.4.2) where, in this case, I_1 and I_2 are the intensities of the clockwise and counterclockwise propagating beams and ϕ_1 and ϕ_2 are the accrued phases after one transit through the loop mirror. The commonly used 3-dB-coupler produces nearly identical intensities in both propagation directions and with $I_1 = I_2 = I_0/2$ equation (3.4.2) reduces to

$$I = I_0\left[1+\cos\left(\phi_1-\phi_2\right)\right] \tag{3.5.7}$$

Neglecting the rotation of the reference frame (e.g., due to Earth's rotation) the phase difference depends on the birefringence, β

$$\phi_1-\phi_2 = \Delta\phi = \frac{2\pi}{\lambda}\beta L \tag{3.5.8}$$

in complete analogy to (3.4.3). If the device is used as a refractive index sensor, the counter-propagating light paths must be differentiated by inducing a phase shift in one path which is dependent on the refractive index of the external sample. To accomplish this, a section of birefringent fibre is usually incorporated into the loop, along with a polarization controller. In this way the two counter-propagating beams are differentiated by polarization state and the refractive index of either the slow or fast axis of the birefringent fibre is modified by exposure to a sample, where the birefringence

$$\beta = n_{fast}\left(n_s\right)-n_{slow}\left(n_s\right) \tag{3.5.9}$$

is the difference between the refractive indices along the fast and slow axes, respectively. Here, it is assumed that the refractive indices of the fast axis and of the slow axis have a different dependence on the external sample refractive index, n_s. It can be shown that the transmission of the fibre loop mirror is then given by [88]

$$\begin{aligned} T &= \left[\sin\left(\frac{\Delta\phi}{2\pi}\right)\cos\left(\theta_1+\theta_2\right)\right]^2 \\ &= \left[\sin\left(\left(n_{fast}\left(n_S\right)-n_{slow}\left(n_S\right)\right)\frac{L}{\lambda}\right)\cos\left(\theta_1+\theta_2\right)\right]^2 \end{aligned} \tag{3.5.10}$$

where θ_1 and θ_2 are the angles between the polarization of the clockwise and counterclockwise propagating light and the fast or slow axis of the birefringent fibre. From (3.5.10) it is apparent that the transmission will vary, at a given wavelength, with n_s, or else the wavelength of a transmission maximum (or minimum) will shift with n_s.

Considering the equivalency of Δn_{eff} and β and therefore the equivalency of (3.5.8) and (3.4.3), we therefore interpret refractive index sensors based on (single-pass) fibre loop mirrors identically to Mach-Zehnder and Michelson interferometers, using *f* as a coefficient to quantify the extent of the interaction of the light in the "signal" arm with the sample, and the Figure of Merit from (3.4.19) to assess the resolving power of the measurement.

3.6.3 Fabry-Pérot Resonators and Fibre Ring Resonators

Fabry-Pérot cavities and fibre ring resonators are resonating optical cavities which are formed either by fibre reflectors, as in the case of fibre Fabry-Pérot (FFP) cavities, or by a ring cavity. Interference in either resonant cavity arises from the superposition of waves having traversed the linear cavity or ring cavity multiple times.

The transmission spectrum of an FFP cavity (in terms of wavelength, λ) follows, to a good approximation, the Airy equation [89]

$$I(\lambda) = \frac{T^2}{(1-R)^2} \frac{I_0}{1+\left(\frac{2\sqrt{R}}{1-R}\right)^2 \sin^2\left(\frac{\pi c_0 t_r}{\lambda}\right)} \qquad (3.5.11)$$

giving a comb of equally spaced resonances dependent on the transmission, *T*, and reflectance, *R,* of the two (identical) mirrors as well as the round-trip time

$$t_r = \frac{2n_{eff}L}{c_0} \text{ (FFP cavity)} \qquad (3.5.12)$$

The inverse of the round-trip time corresponds to the free spectral range, $t^{-1} = \Delta\omega_{FSR}$ in units of angular frequency. For a fibre ring resonator, the corresponding roundtrip time is similarly given by

$$t_r = \frac{n_{eff}L}{c_0} \text{ (ring resonator)} \qquad (3.5.13)$$

and the transmission and reflectance terms, *T* and *R*, account for the corresponding round-trip loss. With (3.5.11) one can obtain the wavelengths at which the interference minima and maxima occur. That is

$$\lambda_{\max,m} = \frac{2n_{eff}L}{m}, \text{ and } \lambda_{\min,m} = \frac{2n_{eff}L}{(m+1/2)}, m = 0,1,2.... \quad (3.5.14)$$

In most FFPs used for refractive index sensing only a part of the mode travelling through the cavity interacts with the environment. By inserting (3.4.4) into (3.5.14) we obtain:

$$\lambda_{\max,m} = \frac{2L}{m}(1-f)n^w + \frac{2L}{m} f\, n_s, \quad m = 0,1,2... \text{ and}$$

$$\lambda_{\min,m} = \frac{2L}{m+1/2}(1-f)n^w + \frac{2L}{m+1/2} f\, n_s, \quad m = 0,1,2.... \quad (3.5.15)$$

In the context of a refractive index sensor, the location of interference maxima and minima shift in wavelength as the refractive index within the cavity changes. For an intensity maximum, the sensitivity of this measurement to refractive index changes is calculated as the derivative of (3.5.15)

$$S = \frac{d\lambda_{\max,m}}{dn_s} = \frac{2fL}{m}, m = 0,1,2.... \quad (3.5.16)$$

The index *m* corresponds to the number of nodes inside the cavity and is related to the free spectral range $\Delta\lambda_{FSR} = (\lambda_{m+1} - \lambda_m)$ through

$$m = \sqrt{\frac{2n_{eff}L}{\Delta\lambda_{FSR}}} \quad (3.5.17)$$

which is an approximation for the common case where $L \gg \Delta\lambda$.

Insertion of (3.5.17) into (3.5.16) yields the sensitivity, *S*, of the Fabry-Perot cavity to refractive index changes of the cavity medium:

$$S = \frac{d\lambda_{\max,m}}{dn_s} = f\sqrt{\frac{2L\,\Delta\lambda_{FSR}}{n_{eff}}} = f\frac{\lambda}{n_{eff}} \text{ for a Fabry-Pérot cavity} \quad (3.5.18)$$

In this approximation the sensitivity therefore depends linearly on the sensitivity coefficient, *f*. As before the sensitivity coefficient, *f*, describes the resonant cavity mode overlap with the surrounding medium.

In (3.5.18) in the far right we substituted $\Delta\lambda_{FSR} = \lambda^2 / 2n_{eff}L$ for a Fabry-Pérot cavity. The sensitivity is therefore not dependent on the cavity length. Again, the approximations in (3.5.17) and (3.5.18) assume that the cavity is long compared to the wavelength of the light and, as before, that dispersion can be neglected. In our meta-analysis of previously reported parameters we rearrange (3.5.18) and use the reported sensitivity and the resonance wavelength together with the free spectral range to determine

$$f = \frac{S\,\lambda}{2L\ \Delta\lambda_{FSR}} \text{ for a Fabry-Pérot cavity} \qquad (3.5.19)$$

The corresponding equations for a ring-cavity instead use $\Delta\lambda_{FSR} = \lambda^2 / n_{eff}L$ and the values are then

$$S = \frac{d\lambda_{\max,m}}{dn_s} = \sqrt{2}\,f\,\frac{\lambda}{n_{eff}} \text{ for a ring-cavity} \qquad (3.5.20)$$

$$f = \frac{S\,\lambda}{\sqrt{2}L\Delta\lambda_{FSR}} \text{ for a ring-cavity} \qquad (3.5.21)$$

The full-width-at-half-maximum of the cavity resonances in either system

$$\nu_{1/2} = \frac{c_0}{\pi n_{eff}L}\frac{1-R}{\sqrt{R}} \qquad (3.5.22)$$

can be obtained by approximating the resonance lineshapes in (3.5.11) with Lorentzian functions [90]. Written in terms of wavelengths, (3.5.22) can be expressed as (3.5.23):

$$\lambda_{1/2} = \frac{\lambda^2}{n_{eff}L}\frac{1-R}{\pi\sqrt{R}} \qquad (3.5.23)$$

The full width at half maximum, $\lambda_{1/2}$, and the free spectral range $\Delta\lambda_{FSR}$ can be used to determine the finesse of the cavity,

$$F = \frac{\Delta\lambda_{FSR}}{\lambda_{1/2}} = \frac{\pi\sqrt{R}}{1-R} \qquad (3.5.24)$$

where the right relation holds in the limit of a high finesse ($F > 4.5$), i.e. for cavities with an average reflectivity of $R > 0.5$.

Most articles either provide the resonance linewidth, or they permit the extraction of this number from published spectra. When spectra are provided on a dB scale, it is necessary to first convert the reported resonance width into a resonance linewidth on a linear scale. One can readily show that the HWHM on a linear scale, $\lambda_{1/2}$, can be determined from the HWHM on the dB scale, $\lambda_{dB,1/2} - \lambda_0$, using (7.4.8) derived in the Appendix

$$\lambda_{1/2} = \left(\lambda_{dB,1/2} - \lambda_0\right)\left(\frac{1}{M''} - 1\right)^{-1/2} \qquad (3.5.25)$$

As before we use (3.4.19) to determine the Figure of Merit for both types of cavities as the ratio of sensitivity and resonance linewidth.

$$FoM = \frac{S}{\lambda_{1/2}} = \frac{2 f L F}{\lambda} \text{ for a Fabry-Perot cavity} \qquad (3.5.26)$$

and

$$FoM = \frac{\sqrt{2} f L F}{\lambda} \text{ for a ring-cavity} \qquad (3.5.27)$$

In some implementations of a fibre Fabry-Perot refractive index sensor the sample is not allowed to enter the cavity, but rather the sensor is partially immersed in the sample. In this case, the reflectivity R in (3.5.11) and (3.5.22) usually arises from Fresnel reflection from the fibre end. Immersion of this fibre end in a sample changes R, thus changing the reflected power at a given wavelength. Here, authors usually provide dI/dn_s as the relevant sensitivity. These sensors have a more complicated dependence on the refractive index since the effective index of the cavity is changing at the same time as the the effective length of the cavity. The effective cavity length extends into the sample liquid due to the large evanescent penetration depth at the reflecting fibre end.

These sensors are particularly sensitive when the sample has a refractive index close to that of the fibre material, i.e., when the evanescent field extends far into the liquid.

3.7. Review of Literature on Interferometry

3.7.1 Meta-Analysis and Methodology

We analysed spectra and tables from 369 publications on Mach-Zehnder interferometers, 64 publications on Michelson, fibre-loop mirror or Sagnac interferometers, and 114 publications on fibre Fabry-Perot or fibre-ring cavities. From these publications we extracted the width and centre wavelength of the interferometer fringe or cavity resonance. The spectra with maximum and minimum intensities, given either on an absolute scale or, more commonly, on a dB-scale, are then used to determine the HWHM of the corresponding interferogram or cavity resonance. Equation (3.5.4) was used to determine the HWHM, $\lambda_{1/2}$, if the interferogram was given on a dB-scale. Similarly, we used (3.5.25) to determine the HWHM, $\lambda_{1/2}$, for fibre cavities. From these values we determined Δn_{eff}, using (3.5.3).

In case of MZ and Michelson interferometers we used Δn_{eff} to determine the sensitivity coefficient, *f*, with (3.5.6) and finally the Figure of Merit with (3.4.19). When multiple interferometer fringes were reported we additionally used (3.5.2) to determine Δn_{eff} and followed the above procedure to calculate *f* and *FoM*.

For fibre cavities such as FPI, we determined the abovementioned metrics from published spectra, as well as the finesse, *F*, from equation (3.5.24). Notably, in all subcategories of interferometers we observe that the value for *f* at times can be greater than one, despite the fact that it represents a fraction as per (3.4.4). We attribute this to a number of potential sources; the mostly likely source lies in our difficulties in obtaining the fringe widths and modulation depths from the published spectra. Our calculation is based on several assumptions, notably that there are only two modes interfering and that the mode numbers are quite large. In reality, many published spectra are asymmetric and exhibit a sloping baseline, likely due to the interference of several

different modes. In cases where we can obtain independent values for Δn_{eff} and for *f* (as described in (3.5.3) and (3.4.14)) we obtain values that are similar, i.e. typically with a factor of 2, leading us to believe that the method is accurate - especially for interferometers in which the arms are much larger than the wavelength of the propagated light.

In the following discussion we focus on the Figure of Merit as the most meaningful parameter as it allows us to compare vastly different devices in their ability to resolve refractive index changes. Recall that the Figures of Merit are inversely correlated to the refractive index resolution of the measurement. As described in (3.4.19) the Figure of Merit is the ratio of the sensitivity, *S*, and the half-width at half maximum, $\lambda_{1/2}$, of a fringe.

Our analysis shows that the Figures of Merit depend to a large extent on the overlap of the propagated mode field with the sample medium – indicated by the value of *f*. In cases when *f* approaches 100% the Figure of Merit tends to large. However, since many of the interferometers and resonators that maximize mode-field overlap only use miniscule grooves, holes, trenches, or gaps and usually have $L < 1$ mm, the effective interaction length *fL* is nevertheless quite small. While previous work aims to minimize the divergence of the mode in the sample by reducing the path through the sample, we argue that an optimal design for an interferometer- or cavity-based fibre sensor should instead aim to confine the mode either by focusing [75,76,91] or by using photonic bandgap materials. Only then can one hope to increase the effective interaction length, *fL*. So far, the largest *FoM* were obtained for devices that maximize *fL* and therefore *FoM* by extending the length of the interferometer arm to $L > 10$ mm and thereby compensate for a lower value of *f*. In the following section we highlight several representative devices that illustrate different paths to optimal refractive index resolution (minimal $\Delta n_{\min}$, maximal *FoM*).

3.7.2 Mach-Zehnder Interferometers

Figure 5 describes the correlation between the length of the interferometer arms and the overlap coefficient, *f*, for several hundred in-fibre Mach-Zehnder Interferometers. One can see that larger overlap coefficients have usually been obtained by building small interferometers. The devices highlighted with red points outliers with high *f* and short *L*; the devices highlighted in blue are devices with the opposite trade-off of low *f* and high *L*, and finally, the orange data point illustrates an "alternative" design which can escape the trade-off between *f* and *L*.. Not surprisingly, instruments in which the light is not guided through the samples do not permit long interaction lengths, and those which rely on light guiding through a long interferometer arm, conversely require larger confinement in the waveguide and less interaction with the sample.

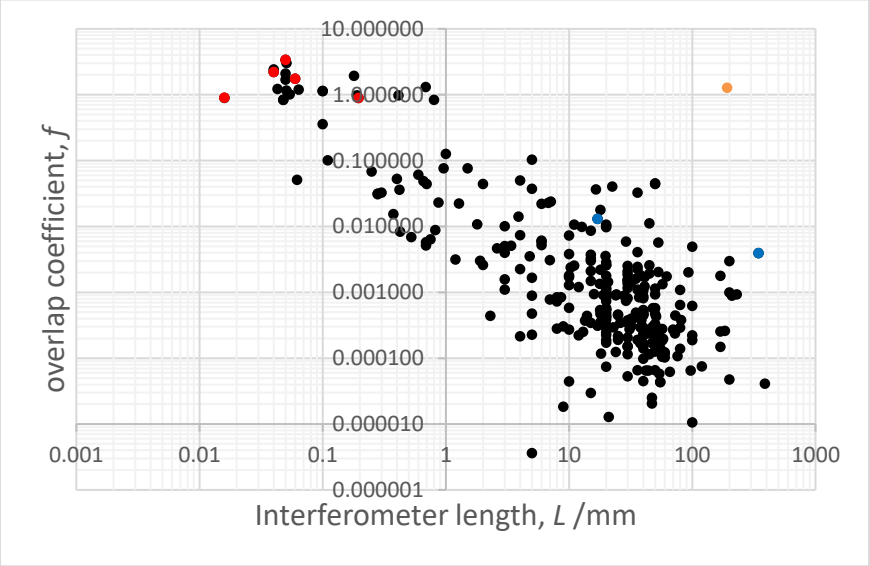

Figure 29. The overlap coefficient, *f*, correlates inversely with interferometer arm length for Mach-Zehnder interferometers indicating stability in the product *fL*. The overlap coefficient is expected to decay with propagation length due to attenuation. The red dots indicate a number of high-performing devices for this type of interferometer that have large *f* values and short interferometer length, *L*. The blue dots indicate an alternative design with smaller *f* values and a longer *L* which are still able to achieve a high *FoM*. The orange dot is the highest *FoM* device in this category.

To maximize the overlap coefficient *f*, Mach-Zehnder interferometers can be fabricated by microfabrication of grooves or holes into the fibre, which are filled with sample liquid. Several of these devices are based on the partial removal of the cladding and a part of the optical fibre core. The light that propagates then splits into two paths: the light that travels through the

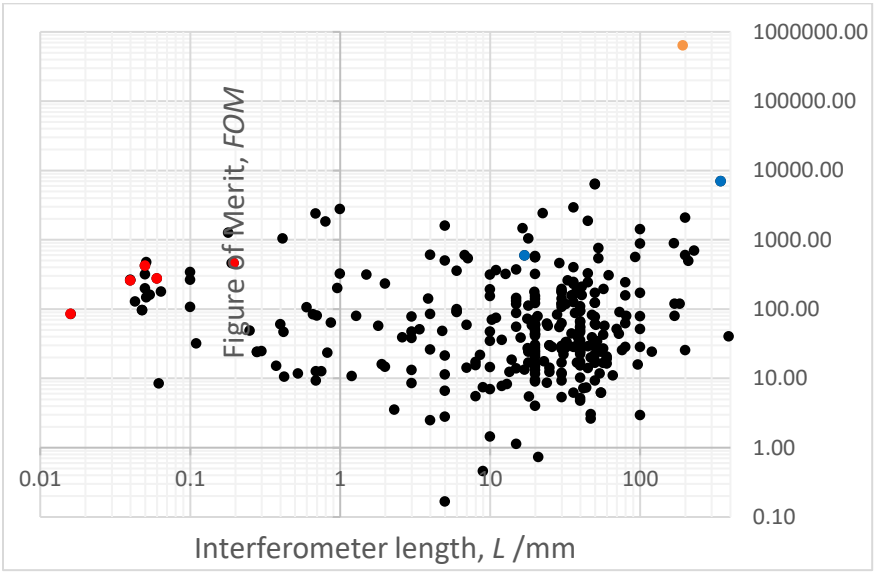

Figure 30. The Figure of Merit is around *FoM* =100 (Δn_{min} = 0.01) for most devices, indicating that for most designs, an increase of the interferometer arm lengths is offset with a corresponding reduction of the overlap coefficient, *f* (See Fig 5). Since the effective interaction length is dependent on the product of *fL*, one expects a similar *FoM*. Notable outliers are those indicated by the blue dots, which indicate a high *FoM* device taking advantage of its long length, and the orange dot, which has the largest *FoM* for the MZI category.

sample liquid in, say, an etched groove and the light that travels in the core. These two paths then combine to create an interferogram at the output of the fibre. As the sensing arm is directly immersed in the liquid to be sensed, the overlap coefficient, *f*, for these devices tends to be very high – typically well above 10%. By comparison, the

average overlap coefficient for evanescent wave devices is between 0.01% and 0.1%. As is shown in Figure 29, these devices therefore achieve a good Figure of Merit, since the product *fL* is large, even if the interferometer length is less than *L* = 1 mm. Of note are the devices highlighted in blue as they achieve a large interaction length through hollow-core structures. Authors in [44] used two core modes in a hollow core photonic crystal fibre to generate the interferometer. Unfortunately, since the two core modes *both* travel through the sample their refractive index contrast Δn_{eff} is small and *f* is only 0.1%. Meanwhile, the device that achieves the highest *FoM* = 640,000 in Figure 30 is a device taking advantage of high *f* = 1.3 and an *L*= 195 mm in a hollow-core photonic bandgap fibre referenced with an SMF to create a Mach-Zehnder interferometer. The *f* is high in this configuration owing to the direct interaction between the bandgap-guided mode and the sample in the hollow core. Since the mode is in fact waveguided in the core of the HC-PBF, one can increase both the propagation length and the *f* simultaneously and create the outlier in the typical negative correlation seen in Figure 29.

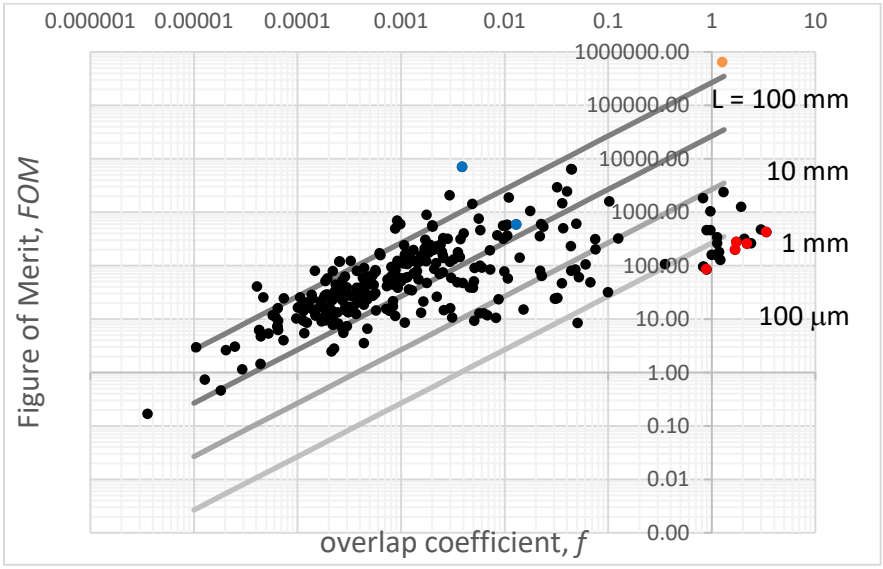

Figure 31. FoM positively correlates with the overlap coefficient for MZI. The grayscale lines show the expected correlation of the two parameters for given

interferometer lengths and for an operation wavelength of 1500 nm. As before, red dots indicate high *FoM* devices with short lengths, whereas the blue dots indicate the other end of the tradeoff between *L* and *f*. The orange dot shows the highest *FoM* device achieved in this analysis.

Figure 31 also demonstrates the correlation between overlap coefficient and Figure of Merit. Given (3.4.19) we expect that the correlation between FoM and *f* is linear with the slope given by the ratio of interaction length and the operating wavelength. The lines show these correlations for devices operating at λ = 1500 nm and with four different lengths. Figure 31 also succinctly shows the shortcoming of all MZI devices available today. Most devices use interactions through the evanescent wave and, with the comparably low overlap coefficient are not able to achieve *FoM* > 1000 corresponding to $n_{\min} > 0.001$ (see equation (3.4.20)). A FoM of more than 100,000 ($n_{\min} < 10^{-5}$) is only achievable if the interferometer arms are at least *L* = 100 mm and *f* ≈100%. Smaller overlap factors can only be compensated by much larger interferometer arms.

Figure 32 shows that there is a correlation between the sensitivity and the Figure of Merit. From (3.4.19) an exact linear correlation is expected, if the width of the

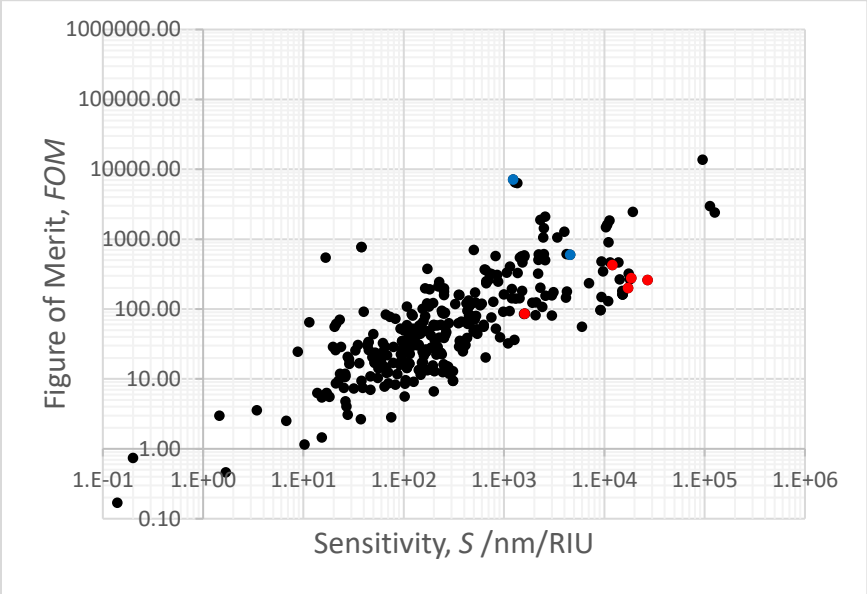

Figure 32. FoM correlates positively with device sensitivity for MZI. The highest *FoM* device is omitted from this figure due to a lack of data on its sensitivity. In general, high *FoM* devices also tend to have high *S*. Moreover, the two are related by the linewidth of the analyzed fringe, so devices that have better *FoM* for the same sensitivity tend to have narrower $\Delta\lambda_{1/2}$.

fringes, $\lambda_{1/2}$, was identical. The observed wide distribution of the FoM for devices with identical sensitivity is indicative of their different effective interaction lengths *fL*. Again, we wish to emphasize that the sensitivity, *S*, is not a good metric for the performance of an interferometer and the *FoM* is a much more meaningful measure. While Fig 8 shows that these two quantities are somewhat correlated, we note that *FoM* =100 can be obtained with devices whose sensitivity ranges from 30 nm/RIU to 10,000 nm/RIU.

Several of the perfoming devices were highlighted in red based on their high overlap coefficient. Out of these, several score highly across multiple evaluation metrics as can be seen in Figure 30, Figure 31 and Figure 32. We present an overview of these devices below and outline the reasons for their high performance.

In [92], a femtosecond laser was used to fabricate a hole in the optical fibre, which was then treated with reactive ion etching to improve its wettability and smoothen its bottom surface. The drilling process removes part of the fiber core. The two arms of the interferometer consist of the light travelling through the core of the fiber and light interacting with the sample, presumably by direct transmission through the sample liquid. The geometry used in the MZI is shown schematically in side-cut and cross-section as well as top-view below in Figure 33. In-line Mach-Zehnder interferometer used in work92. The overlap coefficient *f* = 2.2 is large and is therefore responsible for a moderate Figure of Merit *FoM* = 260 and a large sensitivity of 27000 nm/RIU (see (3.4.9) and (3.4.19)). *FoM* is limited for this short-length (*L* = 0.04 mm) interferometer as discussed above.

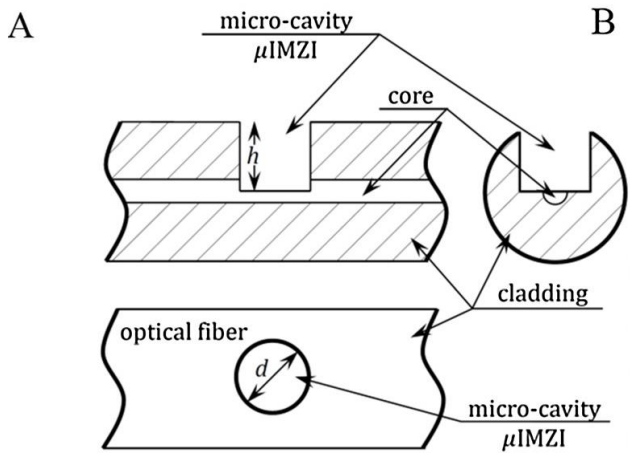

Figure 33. In-line Mach-Zehnder interferometer used in work[92].

In a similar design other workers create a micro-cavity using femtosecond laser etching, which is then oxygen-plasma treated to increase its wettability[93].. This in-line Mach-Zehnder interferometer (MZI) has a high overlap coefficient *f* = 1.7 and the derived quantities of *S* = 19,000 nm/RIU and *FoM* = 276. The device is fabricated by etching a precise cavity in the fibre as seen in Figure 34 to increase Δn_{eff_1} which increases the index contrast and improves *f*. The sensitivity, *S*, is large due to the linear

relationship between *f* and *S*, but the *FoM* is nevertheless moderate because the length *L* is quite short at 0.06 mm.

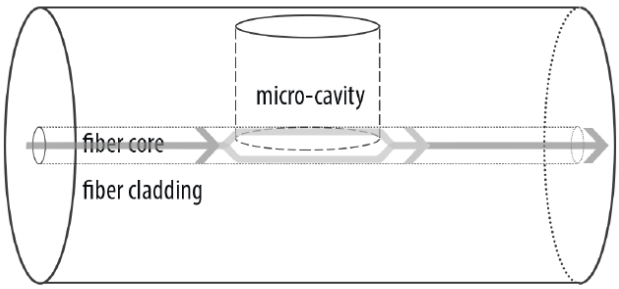

Figure 34. Microcavity in-line MZI [93].

Another type of MZI can be created by completely offsetting the cores of two subsequent pieces of SMF [94] such that light in one arm of the interferometer travels exclusively through the sample (Figure 35), as in the case of etched grooves and trenches. With this improved index contrast between the two arms, very high *f* = 0.89, and *S* = 11,000 nm/RIU can be achieved. Since the light is no longer guided through the sample, the interferometer arm length is short (*L* = 0.195mm), Nevertheless a respectable Figure of Merit, *FoM* = 463, is achieved.

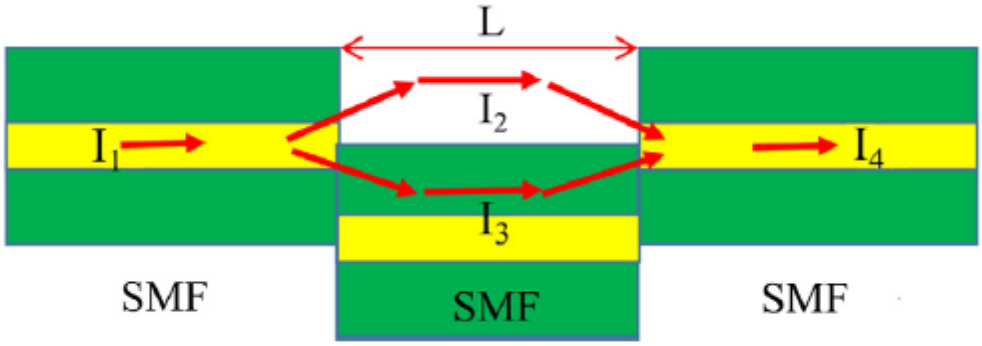

Figure 35. Offset-core fibre MZI [94]. The core mode propagating in the input fibre (I_1) propagates in the air gap created by the offset (I_2) and couples into a cladding mode in the offset SMF (I_3) before being recombined at the entrance facet of the output fibre (I_4).

Many more fiber interferometers that rely on a gap through which light in the sensing arm propagates and interacts with the sample have been built. Several different approaches have been used to create these gaps including machining an air gap into a twin-core fibre [95], femtosecond laser micromachining an air gap in a fibre-Bragg grating [96], etching V-grooves down to the core of the fibre [65], and machining V-shaped grooves in prisms that couple light out of multi-core fibres (MCFs) [97]. These latter two are shown in Figure 36 and Figure 37 and are briefly discussed here.

Authors of some works[65] use a femtosecond laser machining process to inscribe a V-shaped groove down to an SMF core and enhance overlap of sample media and the mode traveling through the etched section, as seen in Figure 36. This achieves an extremely high f = 3.3 for the short sensor length of L = 0.05 mm, and results in a high sensitivity of S = 12,000 nm/RIU and a respectable FoM = 424. This design is similar to previous designs that take advantage of differential phase shift between air gap propagation and fibre-core propagation.

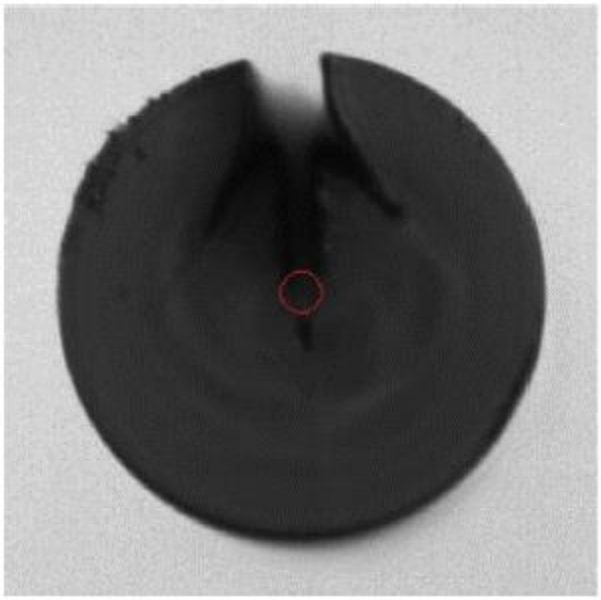

Figure 36. V-shaped groove etched into the core and cladding of an SMF using femtosecond laser and HF etching, from [65]. High pulse energy is responsible for the

wings in the cladding which are created during scattering in the femtosecond ablation process. The centre V-groove partly etches down to the fibre core (shown in red circle).

Meanwhile, authors in [97] have built a coupler on the end facet of a 7-core optical fibre as seen in Figure 37. In this design, the light propagating in one of the cores is prism-coupled into a unique Mach-Zehnder interferometer fabricated into the prism coupler as a V-groove. Light that propagates in the V-groove will accrue differential phase shift depending on which section it travels through and will interfere at the output facet of the V-groove. This light is coupled back into an adjacent core using the prism coupler, and an interferogram is obtained. A high overlap coefficient of f = 0.9 is obtained with this design, but despite its large sensitivity of S = 1600 nm/RIU the Figure of Merit remains moderate (FoM = 85), likely due to the very short interaction length L = 0.02 mm.

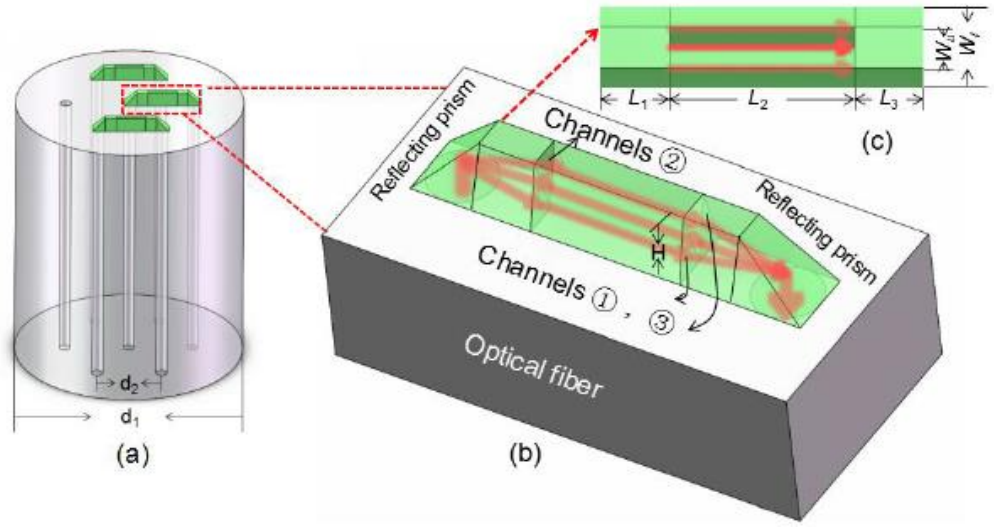

Figure 37. (a) Three prism-based MZIs manufactured on the end facet of a 7-core fibre. (b) Close-up of a singular prism-based MZI with the V-groove for sensing [97].The trapezoid body with an inverted V-shaped groove is shown in the inset along with lower and upper surface length and width dimensions of L_u, W_u, L_l, W_l. The height of the trapezoid is H, and the length of the groove is L_2 while its width is Wu and the depth H.

The entire length of the prism is $L_1+L_2+L_3$. Finally, the pitch between the air holes in the PCF is indicated with d_2 while the diameter of the PCF is d_1.

The majority of devices we reviewed were designed such that interactions with the sample occur through interactions of the evanescent wave of light propagating in the sensing arm. Devices that employ evanescent wave responses tend to be associated with low values of *f*. Since the overlap coefficient depends on the interaction depth of the evanescent field, it is advantageous to match the index of the sensing arm to that of the sample liquid. [55]. Since *f* is strongly dependent on the RI of the surrounding medium, the sensitivity is strongly dependent of the refractive index. Indeed, many of the reported values for S are specific to a particular wavelength and sample index. Of course, at sample refractive index values above those of the cladding, the wave is no longer guided.

Even though the overlap coefficient is much smaller compared to the direct sensing devices described above, the waveguiding through the sensing arm permits much larger interferometer lengths leading to an increase of the sensitivity *S* and, consequently of the *FoM*. Examples of works benefiting from a long sensing arms are [98] shown in Figure 39 and [44] in Figure 40[99].

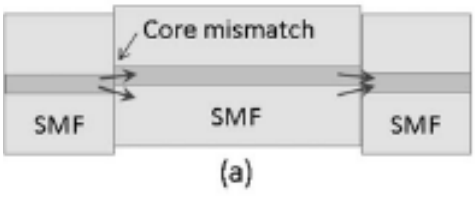

Figure 38. Core-offset evanescent wave MZI sensor [100].

Figure 38 shows a core-mismatch sensor fabricated in an offset stub of SMF between two regular pieces of SMF. This design is used as a RI sensor based on its evanescent field extending out into the surrounding. Despite its low overlap coefficient

of f = 0.01, the increased sensor arm length of 17 mm compensates for this metric to increase the sensitivity to 4577 nm/RIU and the *FoM* to a value of 596.

Hollow core fibers are unique waveguides which allow guiding of light through the sample itself and are therefore poised to combine the advantages of direct sample interactions in the sensing arm with long interactions lengths. One might then expect exceptionally large *FoM* if the refractive index contrast between the sensing arm and the reference arm was high and the overlap coefficient was close to unity. Indeed authors recently demonstrated such an interferometer [44], but since the interference occurred between two different guided *core modes*, which both interacted with the gas samples to a different extent, the overlap coefficient was comparably low (f =0.008). This was partially offset by the large interaction length (L= 346 mm) and lead to a respectable *FoM* = 7046. The device could measure the refractive index of Helium gas at reduced pressures ($\Delta n_{\min} = 0.00014$).

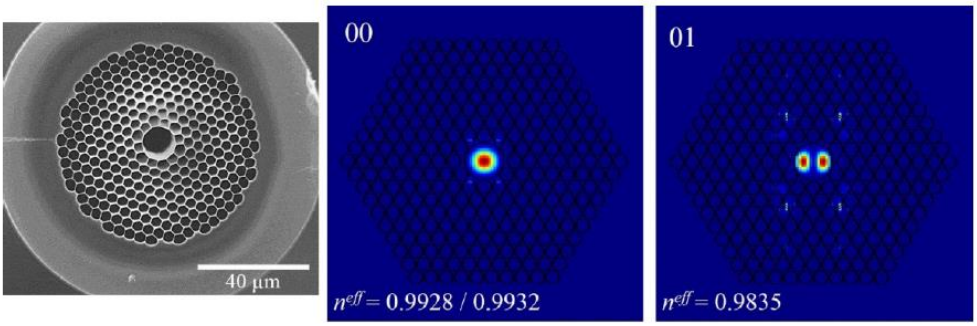

Figure 39. Two interfering core modes in a hollow core fibre [44], produce a long sensing arm which partly compensates for a low overlap coefficient to result in large FoM.

The highest *FoM* device we reviewed (Figure 30, Figure 31, and Figure 32) is a Mach-Zehnder interferometer with an architecture deriving from balancing a length of SMF with a hollow-core photonic bandgap fibre (HC-PBF) seen in Figure 40 [99]. This device has an *FoM* = 636620, while the *S* could not be calculated due to the nature of the interferograms. The mode propagating in the bandgap of the photonic crystal fibre interacts directly with the sample introduced into the holes of the HC-PBF and therefore f = 1.27 is high. Owing to waveguiding in the photonic bandgap rather than evanescent

wave propagation, the interaction length with the sample is as long as the HCF (L = 195 mm). To our knowledge HCF-based sensors appear to be the only device architectures that are currently capable of circumventing the fL product tradeoff seen in evanescent-wave and fiber-notch sensors.

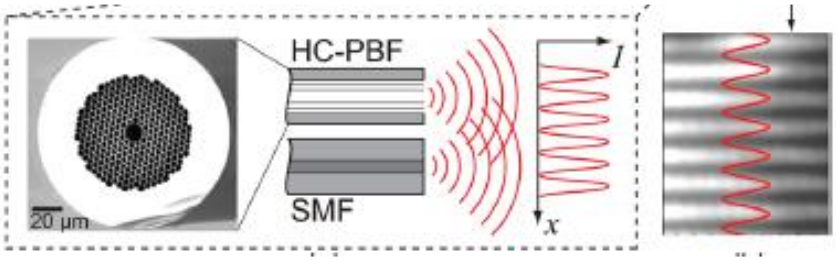

Figure 40. Hollow-core photonic bandgap fibre-based MZI creating a free-space dual-slit interferogram [99].

3.7.3 Michelson Interferometers

The main difference between the in-fibre Mach-Zehnder interferometers and the Michelson interferometers lies in the reflection element that allows the light in the sensing arm and reference arm to reverse direction and recombine at the (single) coupler. Given their similarities it is maybe not surprising that Figure 41-Figure 44 for Michelson interferometers show the same trends as Figure 29-Figure 32 for Mach-Zehnder interferometers.

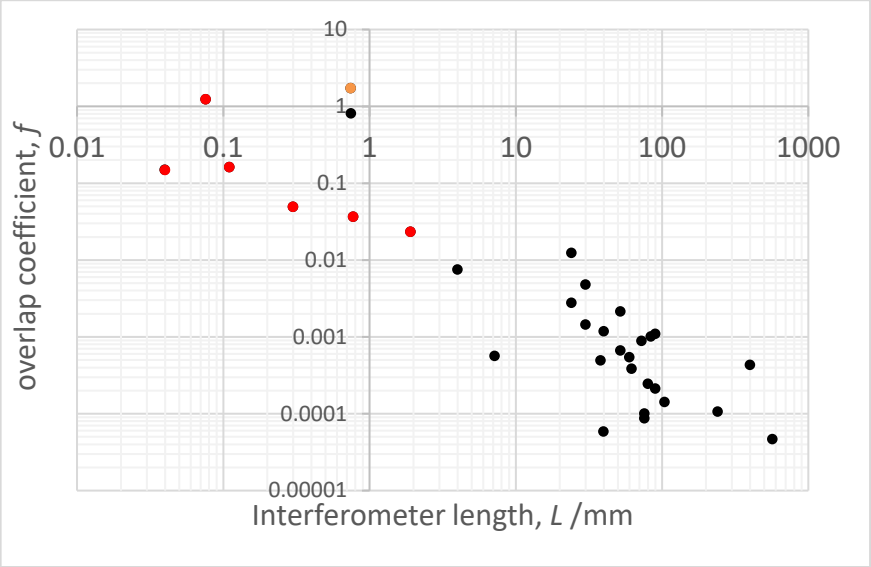

Figure 41. Overlap coefficient is inversely correlated with interferometer length for Michelson interferometers, as also seen in Mach-Zehnder interferometers. Outlined in orange is the highest *FoM* device, which also has the highest *f* number.

A number of Michelson fibre interferometers have been highlighted in Figure 41 to Figure 44 to provide an overview of the different types of devices. Figure 41 shows again that devices based on holes gaps and trenches achieve high overlap coefficients, *f*, but are not able to guide the light in the sensing arm over long distances (small *L*). This is similar to what was observed in Figure 29 for Mach-Zehnder interferometers. Since in most devices a large *f* implies that *L* is small, it is not surprising that Figure 42 shows no discernible dependence of the Figure of Merit (*FoM* = $4fL/\lambda$) on the lengths of the interferometer arms – as was also observed for Mach-Zehnder interferometers in Figure 30.

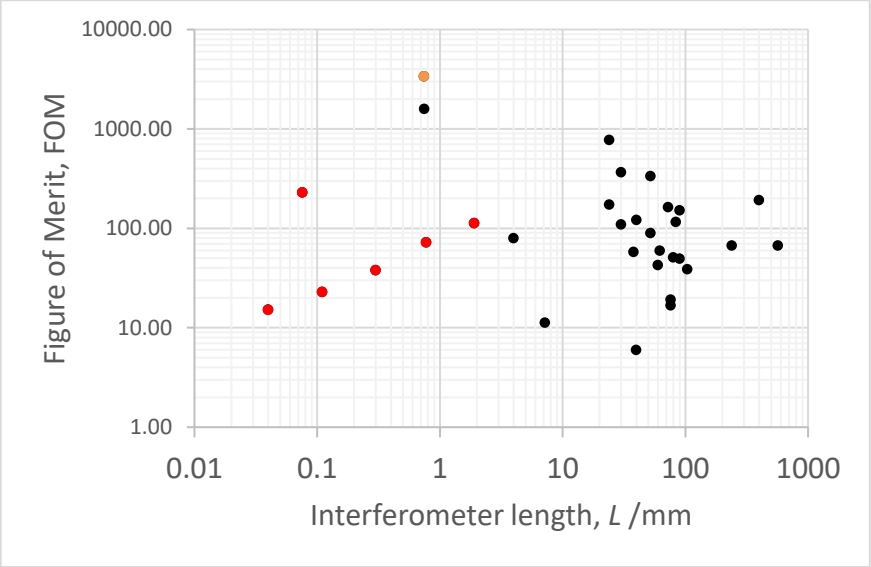

Figure 42. The FoM for a given Michelson device is dependent on the product *fL*. As a result, the devices with a high *fL* value perform well on this metric. Due to a limited number of publications on Michelson interferometers, the lack of correlation between *FoM* and *L* is not clearly seen in this figure as in Figure 30 but is expected as most of these methods rely on evanescent wave interactions with the sample. For similar *f* values, increasing the length increases the *FoM*. Conversely, for similar interferometer lengths, increased *f* means a larger *FoM* overall. The highest *FoM* (orange) device has a moderate length of *L* = 0.37 mm.

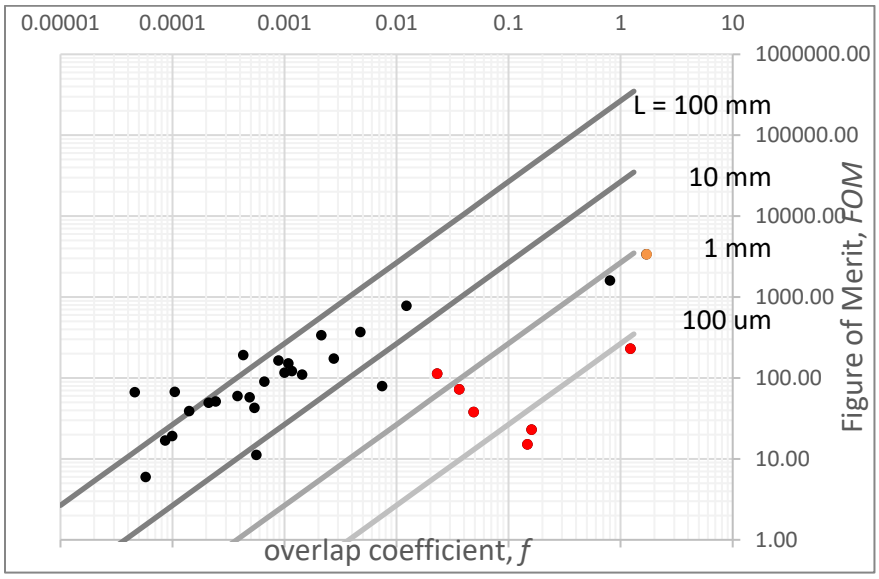

Figure 43. The expected FoM-overlap coefficient correlation for a given device length is shown in grayscale lines for Michelson interferometers. Devices behave as expected from their calculated correlations. The highest *FoM* (orange) device takes advantage of direct wave propagation in the sample through an etched gap in the tapered fibre tip that creates the Michelson interferometer, as opposed to evanescent wave sensing.

Figure 43 demonstrates that several of the Michelson interferometers employing direct unguided light propagation through the sample liquids can achieve large Figures of Merit. Just as in Figure 31, the solid lines are drawn to provide an indication which *FoM* might be expected from devices operating at 1500 nm and having the respective interaction lengths.

Finally, a number of devices with high *f* values despite using evanescent wave interactions have been fabricated using S-tapers [101], HF-etched tapers [102] or collapsed regions [103], sharp tips [79] and micromachining using femtosecond lasers [104] These configurations exhibit large evanescent interactions with the surrounding medium (highlighted in red in Figure 43) and have large *f* values. Conversely, evanescent wave

sensor designs with lower overlap coefficients can take advantage of waveguiding in the sensing arms to create long interferometer arm lengths as in [55] to achieve high *FoM*.

In the following we showcase several devices as examples of their kind, be it large *f* and shorter *L*, or the opposite. A number of these structures are based on tapers, which when done adiabatically are used as power couplers, sensors, and add-drop filters. However, in order to get a good mixing of core and cladding modes, one typically has to manufacture non-adiabatic structures such as abrupt tapers as per [35]. In this work, a gold-terminated end facet acts as the reflection mirror that forms the Michelson interferometer. Despite the large evanescent field, the overlap coefficient is moderate (*f* = 0.0002) but the sensitivity is fair (*S* = 29 nm/RIU) with *FoM* = 19 owing to the very long interaction length (38 mm). Of note is the fact that increasing the overlap coefficient *f* might be more practical than increasing the interferometer arm length in achieving a high *FoM*.

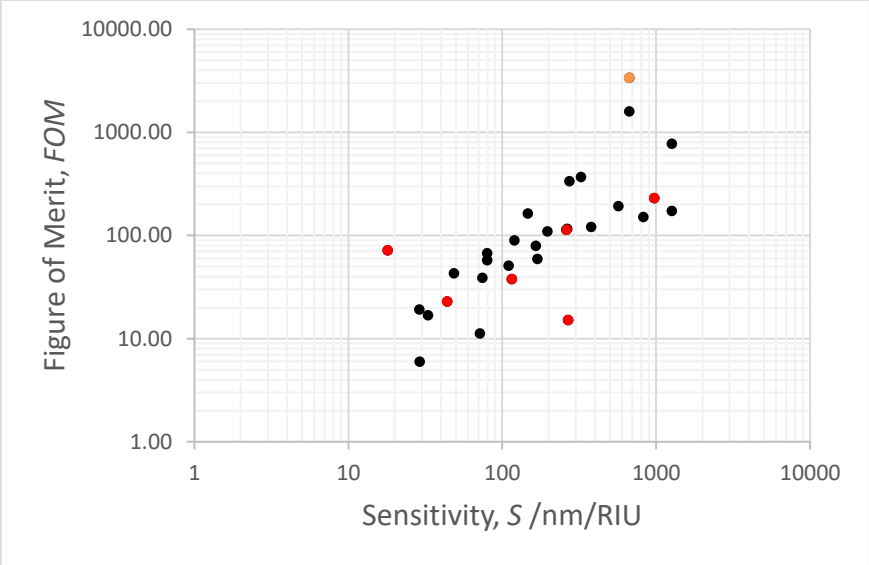

Figure 44. FoM is positively correlated with device sensitivity for Michelson interferometers, as per (3.4.19) via the linewidth of the fringe analyzed.

Reflective fibre tips as seen in [79] have achieved exceptionally high *FoM* = 1589 and *S* = 670 nm/RIU owing to their high overlap coefficient, *f* = 1.6 for *L*= 0.37 mm. In the design shown in Figure 45, an etched trench creates the reflections necessary for

exciting cladding modes, which in turn couple with the core modes at the tapered tip upon retroreflection. The large evanescent field at the trench provides an enhanced overlap with the sensing material, and contributes to the sensor performance.

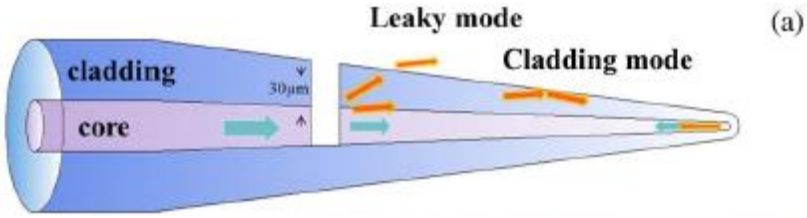

Figure 45. Schematic of a fibre-tip Michelson interferometer with a femtosecond laser machined trench [79].

Another type of tip is seen in Figure 46, created using a fusion arc splicer. The Kagomé PCF was fused at the tip using the splicer, and an air-bubble was created at the fully collapsed region. This defect excites cladding modes, which, combine with the core modes upon reflection from the spherical tip. The evanescent field out of the collapsed region is responsible for the moderately high f = 0.07, which combined with a short length of 0.39 mm give a S = 18 nm/RIU with FoM = 72.

Figure 46. Microscopic image of a PCF formed into a spherical cap to create a Michelson interferometer. An air bubble was formed at the junction of the intact PCF and the collapsed region using a splicer to excite cladding modes [105].

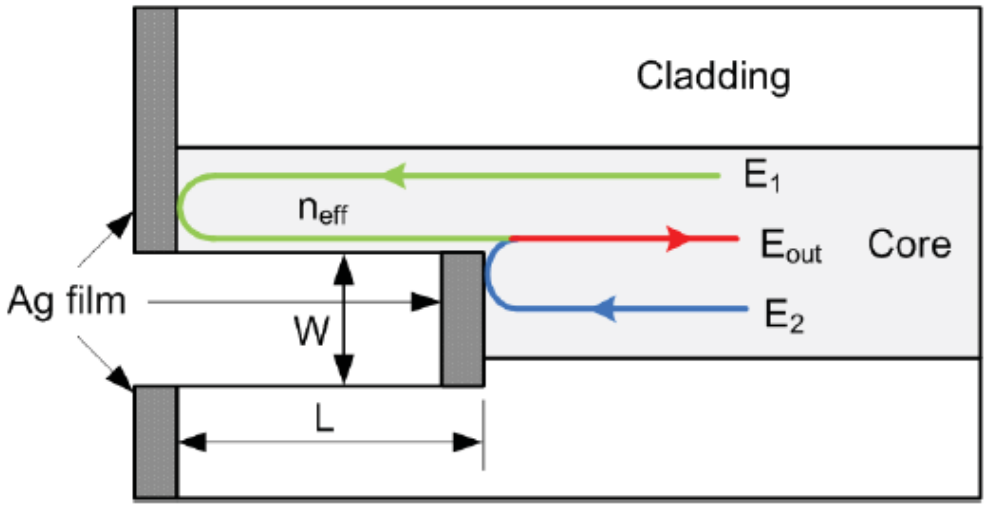

Figure 47. In-line fibre Michelson interferometer after [104].

The design in Figure 47 [104] is based on differential reflection from two end facets of a Michelson interferometer fabricated in a regular SMF Figure 47. The evanescent field in the micromachined gap greatly contributes to a large value of f = 2.5, which translates to high S = 975 nm/RIU and FoM = 229, despite the extremely short (L = 0.04 mm) length of this sensor.

Tapered structures can improve the overlap coefficient by the large evanescent field extension into the surrounding area. An example of this is seen in the S-taper that has been used in [101] (shown in Figure 48). Owing to the bent fiber, there is a large evanescent field extending into the surrounding environment which improves the f metric and the FoM as a result. At a compact length of L = 0.02 mm, this sensor also has a high S = 269 nm/RIU and FoM = 15. Another use of tapered structures in reflective sensing is seen in Figure 49 [102] with the tapered core of a multi-mode fibre (MMF) creating the retroreflection structure at the tip. The reflection from the conical end and the reflection from the tapered core tip interfere to create a Michelson interferometer. The evanescent field at the tip (2 in Figure 49) boosts f to near 0.1 at a short interaction length of 0.15 mm. The sensitivity, correlated with f, is S = 116 nm/RIU for an overall FoM = 38 at this sensor length.

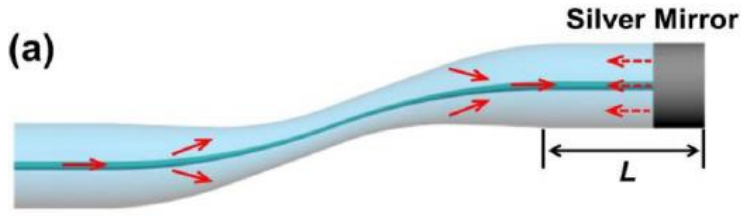

Figure 48. Schematic of an S-tapered Michelson interferometer with a silvered end facet.

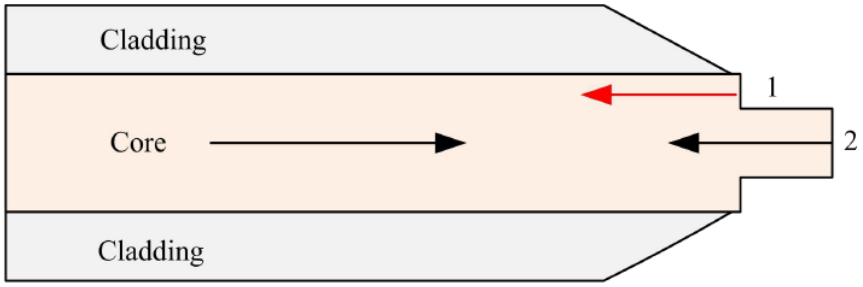

Figure 49. Schematic of a single-cone MMF taper.

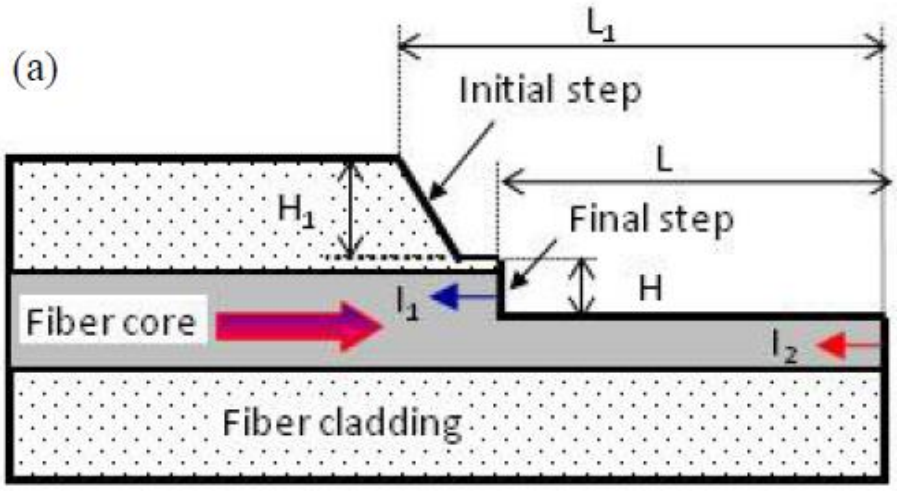

Figure 50. Schematic of a step-structure Michelson interferometer after the study in [106].

A step-structure interferometer is fabricated using femtosecond laser micromachining as shown in Figure 50 by cutting down to the fibre core centre. Light propagating into the step and the light reflected from the core tip interfere upon recombination at the final step. The short length of 0.06 mm, and the comparably high

overlap coefficient of f = 0.16 contribute to the sensitivity of S = 44 nm/RIU and a moderate *FoM* = 23.

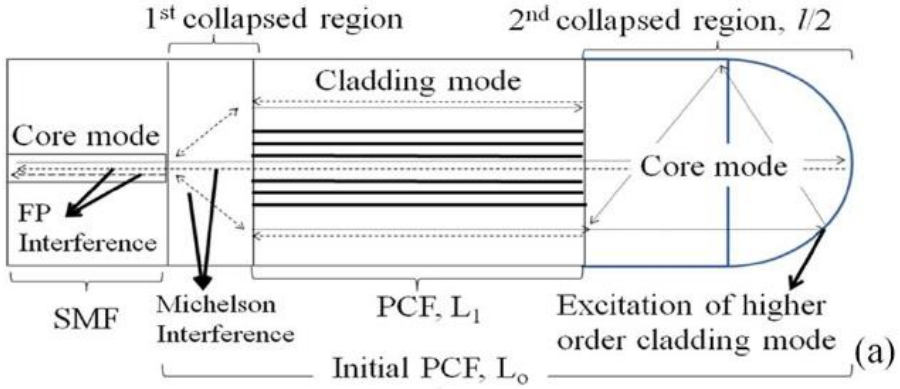

Figure 51. Collapsed PCF-SMF fusion to create a Michelson interferometer, after the work done in [103].

In reference [103] a PCF segment has been spliced to an SMF and fused to create a collapsed region between the two (Figure 51). This region creates a strong mode coupling between the core and the cladding modes of the PCF. The spherical cap at the end of the PCF is used to excite higher order modes in the second collapsed region. The propagating cladding modes couple with the core modes at the first collapsed region, creating a Michelson interferometer. For a moderately high value of f = 0.05 and a comparably long L = 0.95 mm, we get a high sensitivity of 262 nm/RIU and a high *FoM* = 113. As mentioned before, the overlap coefficient decreases with increasing propagation length as the evanescent field cannot stay localized over large distances.

Overall, we observe that the best Michelson interferometer shown in Figure 45 [79] has direct mode propagation similar to the best MZI featuring free-space waveguiding based on a photonic bandgap discussed on the previous section [99]. All other sensors base their detection on evanescent wave sensing, where the product fL needs to be maximized in a trade-off that involves waveguiding through the sensing arm, and the overlap of the evanescent field with the analyte. We note that the metrics cited in this section are not as high as those of MZI, which may be attributable to the limited number of data points that could be included in this analysis.

3.7.4 Sagnac Interferometers

Figure 55 shows several high sensitivity Sagnac interferometers that mostly operate based on polarimetric interference, with the exception of one modal interference example shown by the blue data point [107], see Figure 60. By employing high-birefringence fibres many groups have succeeded in using accumulated optical phase difference in two counter-propagating waves to improve sensitivity. This improvement is also reflected in the *FoM* metric. Overlap coefficients, *f*, for these devices are not as high as those seen in the other types of interferometers, mostly due to inherent limitations in building evanescent sensors based on high-birefringence waveguides. It is difficult to discern a trend in *FoM* given the limited data in Figure 54, but overall, we would expect to see the high-*f,* short-*L* devices to have about the same *FoM* as this latter is a product of the two. Moreover, the high-*L* devices for the same *f* values, as highlighted between *L* = 10 – 100 mm, would have correspondingly increasing *FoM* values as observed. We note that the highest *f* device in Figure 52 does not result in the highest *FoM* in this category, since this work [108] uses a very short length (*L* = 0.02 mm) which limits the *FoM*.

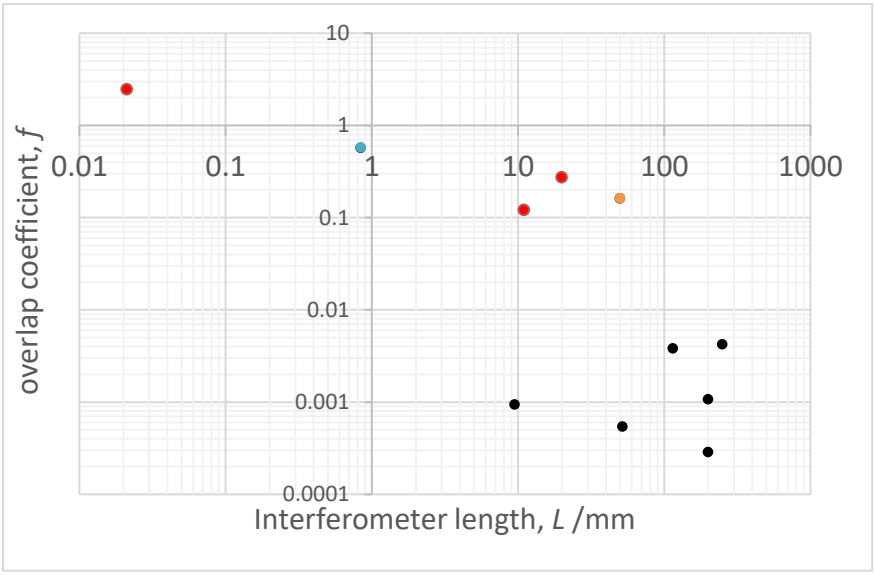

Figure 52. Overlap coefficient as a function of interferometer length for Sagnac Interferometers. Highlighted in orange is the highest *FoM* device in this category, and blue the only non-polarimetric Sagnac interferometer. The highest overlap coefficient

does not result in the highest *FoM* for Sagnac interferometers due to its length *L* = 0.02 mm. In general, the overlap coefficients are much lower in this evanescent wave sensing method than in direct sensing architectures used in other categories of sensors, such as MZI and MI.

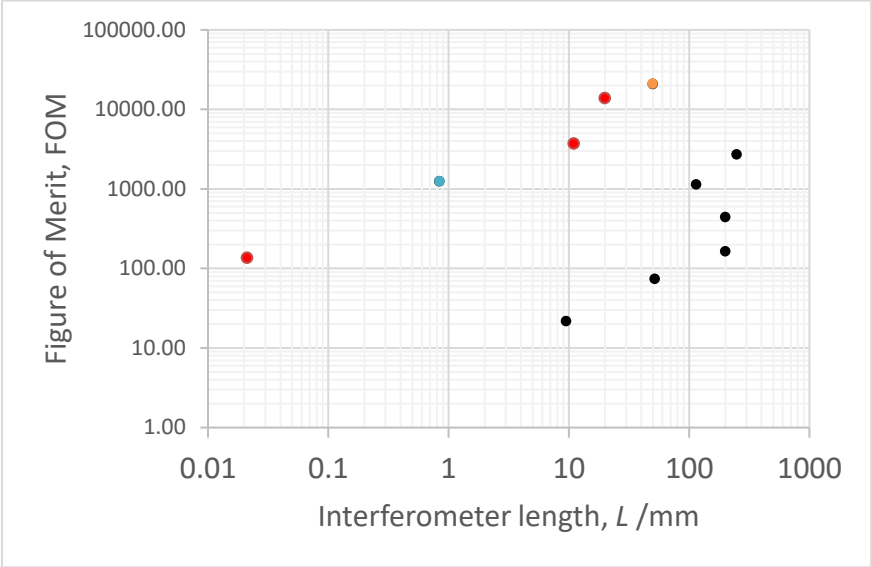

Figure 53. Figure of Merit for Sagnac loops based on polarimetric interference. For similar *f* values, devices that are longer have higher *FoM* values. The modal Sagnac interferometer is shown in blue, whereas the best performing device is shown in orange.

The positive correlation between *FoM* and *f* is apparent in Figure 54. The expected correlations are given in the grayscale lines for given device lengths and appear to hold true. As the device lengths scale down in order of magnitude, one moves from the 10-100 mm correlation lines to the 0.1-1 mm correlation lines.

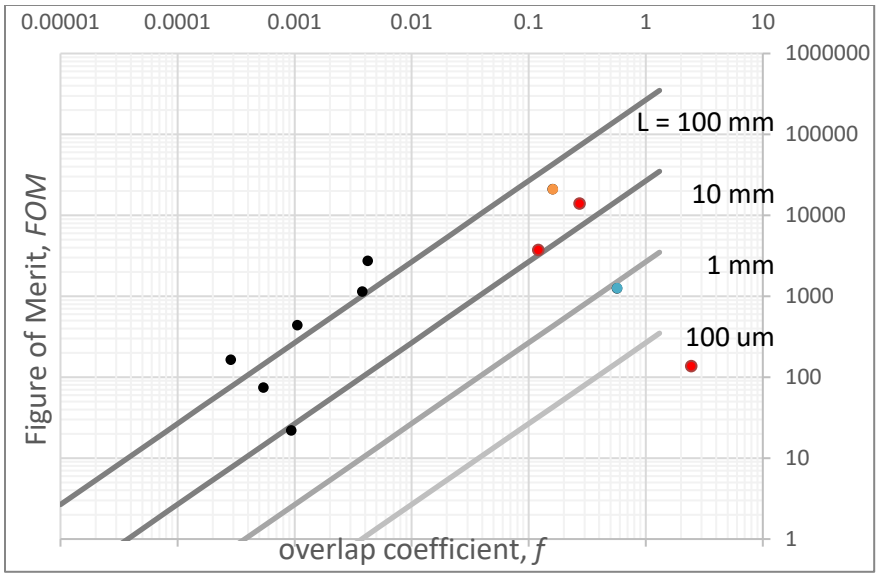

Figure 54. Figure of Merit as a function of overlap coefficient for Sagnac loops follows a positive correlation, despite the limited number of studies in this area. The *FoM* increases with the device length for a given overlap coefficient. The highest *f* device (*f* = 2.46, *FoM* = 135) does not result in the highest *FoM* in this category (*FoM* = 20904).

The *FoM* is expected to be positively correlated with the sensitivity in Figure 55. As previously discussed, the *FoM* is largely dependent on the product *fL* and as we have devices that span 4 order of magnitudes in *L* and 2 orders in *f*, it follows that the FoM also spans several orders of magnitude. Some examples of these devices are discussed in terms of their metrics and principles of operation.

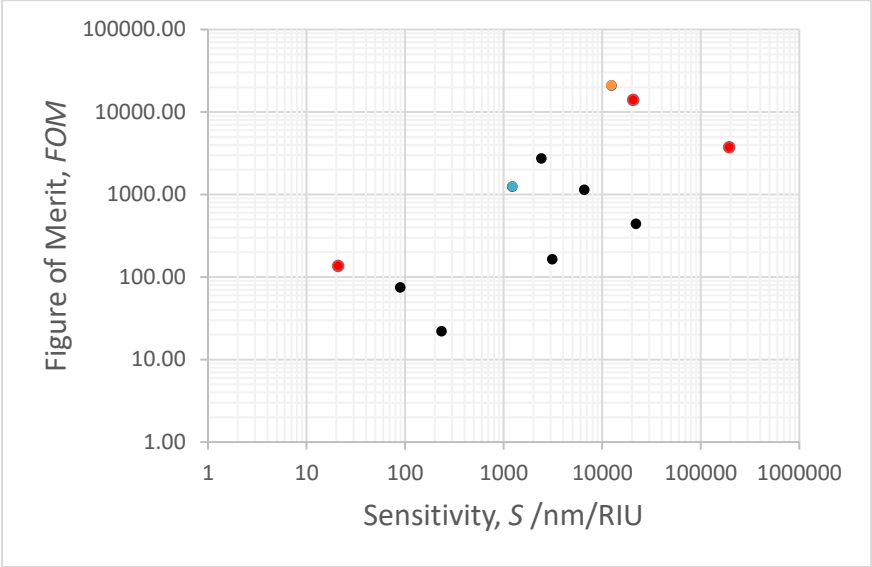

Figure 55. Figure of Merit appears to correlate positively with sensitivity for Sagnac loops, as expected from (3.4.19). The highest *FoM* device shown in orange also has one of the highest sensitivities in this category. The highest *f* device (*f* = 2.46) only has a *FoM* of 135. While most of the highlighted data points show polarimetric Sagnac interferometers, the blue dot indicates a modal interferometer that still has a *FoM* = 1245, competitive with the polarimetric methods with similar *S* values.

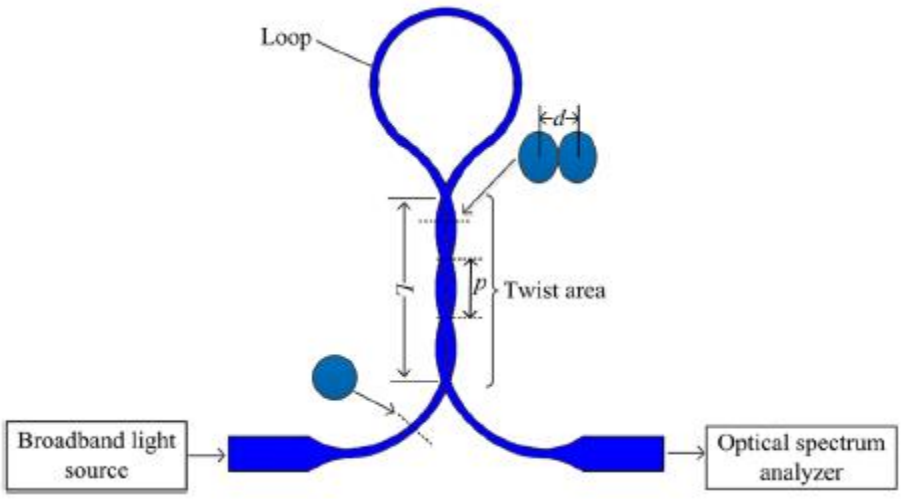

Figure 56. Schematic of a single-mode microfibre loop interferometer, after the work in [109].

Figure 56 shows a long, tapered section of single mode fiber (Corning SMF-28) that is twisted into a loop. At this 3-dB-coupler the incident beam is split into two counterpropagating waves which recombine at the same twisted section. Each counterpropagating beam is split into two polarization states due to the birefringence, resulting from the distortion of the fibre in the twisted fibre area. The optical phase difference that accumulates along this interferometer is dependent on the birefringence introduced by the twisted section, which, in turn depends on the pitch and the number of the twists in the coupling region. Immersing the twisted section in the sample liquid changes the birefringence, and therefore the position of the interference fringes. Owing to the taper, the field evanescing out of the twist area is considerable f = 0.16 and coupled with the sensor length of L = 50 mm, the sensitivity S = 12,500 nm/RIU and the FoM = 20904 are both very high. This sensor is unusual since the length of the loop is irrelevant to the performance of the sensor and the sensing occurs through interaction of the sample with the birefringent coupler.

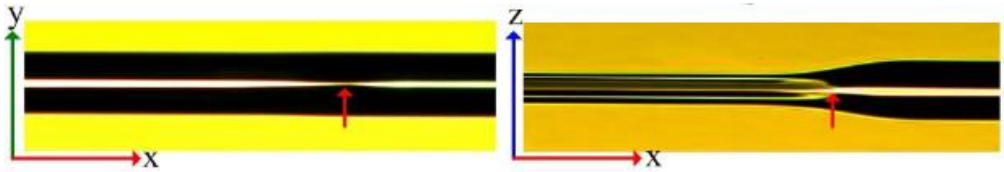

Figure 57. Schematic of CO_2 laser machined fibre, before and after machining [110].

It is far more common to insert the birefringent sensing region into the loop section of the fiber and use a conventional 3-dB coupler. In reference [110] the silica fibre in the loop section has been ablated using a CO_2 laser while it is fixed on translation stages. As can be seen from Figure 57, the cladding part of the fibre is removed under laser exposure, leaving a milled taper with an elliptical geometry. By putting this highly birefringent fibre in a fibre loop configuration, a phase difference is induced between the orthogonal polarizations of light traveling along the fibre, and polarimetric interference is obtained. The relatively long sensing section (L = 11 mm) compensates

for the rather moderate overlap coefficient (f = 0.12) achieved with this design, thereby obtaining a high Figure of Merit (*FoM* = 3700).

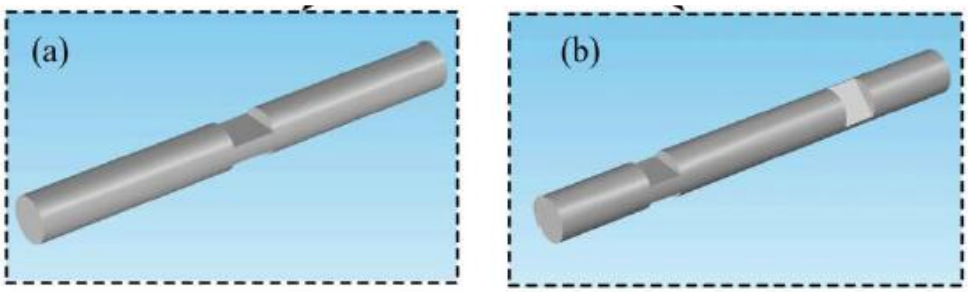

Figure 58. Single- and double cascaded high birefringence fibres in Sagnac loops, after the study in [111].

The use of highly birefringent (HiBi) microfibre-based Sagnac loops as shown in Figure 58 also enables polarimetric interference. The light split into two beams at the coupler will experience a differential phase shift at the HiBi section(s) and will recouple at the polarization controller to create interference fringes. For the length of L = 20 mm and moderately large overlap coefficient of f = 0.27, this design boasts a large *FoM* = 14,000 and an extremely high sensitivity of S = 21,000 nm/RIU.

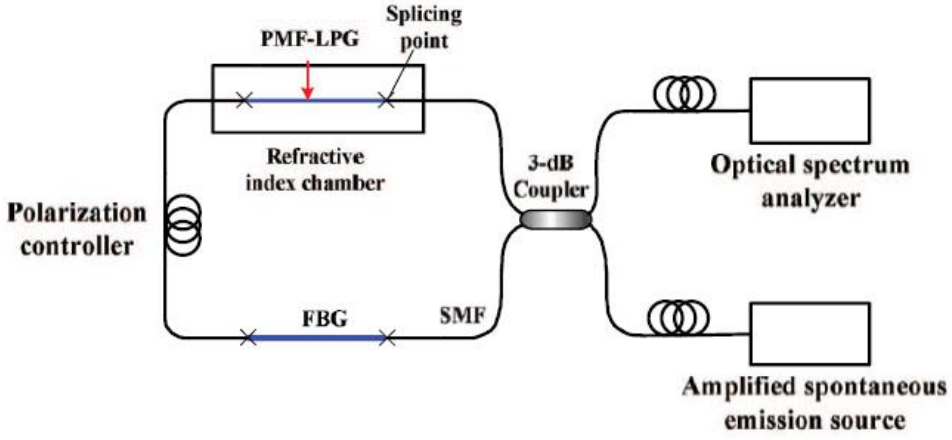

Figure 59. Schematic of the long-period grating and fibre-Bragg grating Sagnac interferometer as per [108].

A similar Sagnac loop has been created[108] in a fibre-loop mirror with a long-period grating (LPG) inscribed in a polarization-maintaining fibre in one arm and a fibre-Bragg grating in the other arm for temperature compensation (Figure 59). The LPG is sensitive to changes in the external refractive index, and the temperature compensation by the FBG coupled with the interferometer structure allows for higher sensitivities than an LPG sensor alone. In this design, the extremely large overlap coefficient of f = 2.46 coupled with the short length of L = 0.02 mm result in a moderate sensitivity of S = 21 nm/RIU but a moderately large FoM =136. We note that the f is unlikely to be truly this large due to a lack of direct interaction of the sensing mode with the analyte. Rather, in this design, the evanescent wave extending out of the LPG interacts with the analyte in the RI chamber indicated in the figure to accrue a differential phase shift compared to the FBG section spliced in the reference arm.

Figure 60. The taper section of a taper-fibre Sagnac loop interferometer as seen in [107].

Tapers, as discussed in Michelson Interferometers, result in the enhanced evanescence of the core mode out of the tapered section into the surrounding medium Figure 60. In this study[107], a non-adiabatic taper has been drawn for modal mixing. Inside a Sagnac loop, this taper functions to create a differential phase shift between the LP_{01} core mode and the LP_{01} and LP_{02} cladding modes, whose coupling efficiencies are polarization dependent. The extremely narrow tapered section has an overlap

coefficient f = *0*.57, sensitivity S = 1200 nm/RIU and *FoM* = 1200 for its length L = 0.84 mm.

Sagnac interferometers discussed in this section are mostly based on birefringent structures creating a differential phase shift between the two orthogonal polarizations of light counterpropagating in a loop. Using polarization controllers, these counterpropagating, orthogonal polarization beams are aligned again to interfere at the coupler that creates the Sagnac loop. The exception to this method is the modal interferometer presented by [107] where a Sagnac loop is created with a tapered fibre section shown in Figure 60 creating a modal interferometer between the fundamental core mode and the first two modes of the cladding counterpropagating in the loop. The performances of these devices are once again mostly predicted by their *fL* product given that all the devices discussed in this section are all based on evanescent wave detection.

3.7.5 In-Fiber Cavity Sensors

As we observed for MZ-interferometers in Figure 29 and Michelson interferometers in Figure 41, some Fabry-Pérot cavities in Figure 61 also show high overlap coefficients, *f*, especially for short cavity lengths. In these works, the high overlap coefficient is achieved using taper splices [112], hollow core structures [113], offset splices [114], and bare cores [115] as described below. The analysis of metrics also includes other types of cavities such as ring laser cavities; however, these cavities did not perform exceptionally in the *FoM* metric and are therefore not reviewed here.

Figure 62 shows that the devices with similar *fL* products values have similar *FoM* values as well. The small *fL* product (f = 0.01, L = 0.025 mm) publication shown as the blue data point only has an *FoM* = 4.47 [116]. Conversely, a large *fL* product (f = 0.07, L = 18 mm) seen in [117] has an *FoM* = 29,000. In Figure 63 the high-finesse outliers are due to a combination of high free-spectral range (FSR) and low HWHM features. The FSR can be increased by decreasing the interferometer length while the HWHM increases with the roundtrip losses in the cavity. Moreover, we see that a high finesse does *not* necessarily imply a higher *FoM* sensor [116]. In fact, the overlap coefficient *f* and finesse tend to be

competing quantities because modes extending out of waveguides contribute to the resonator losses, and in turn reduce the finesse.

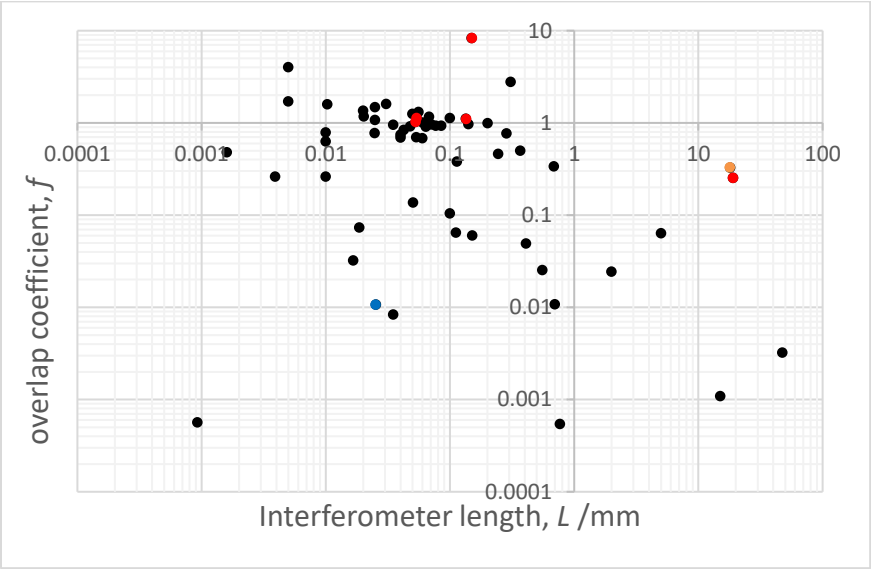

Figure 61. Overlap coefficient as a function of interferometer length for Fabry-Pérot cavities. High *f* devices are typically also high in *FoM*, as per Figure 64. The red dots indicate devices that are discussed in the text, whereas the orange is the highest *FoM* device of this category. The blue data point indicates a high-finesse resonator that has low *FoM.*

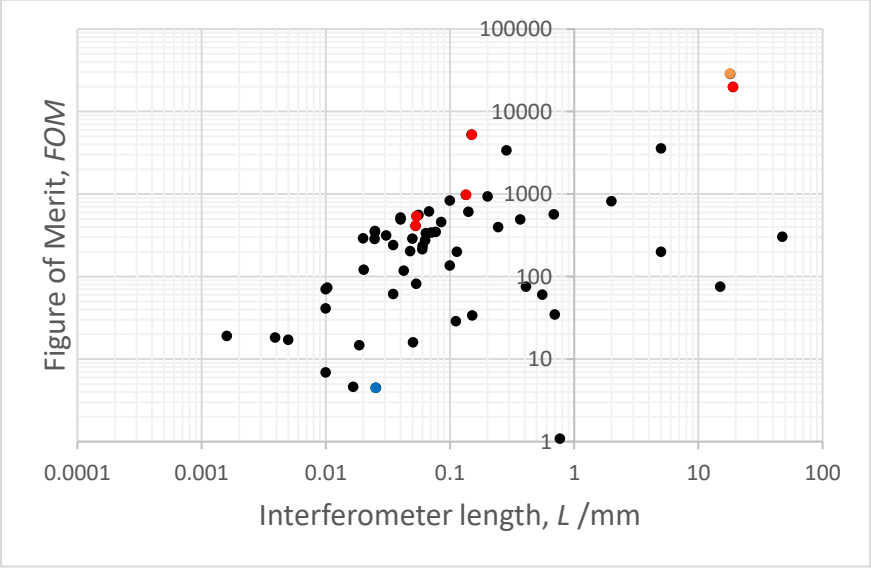

Figure 62. *FoM* can be increased by increasing *f* as in Figure 61 or by increasing *L* as per the right-most data point in this figure. The low-*FoM* data point in this figure is a

high-finesse cavity of F = 131, albeit with a L= 0.025 mm and f = 0.01. The expression for the *FoM* of ring resonators differs slightly as per (3.5.27).

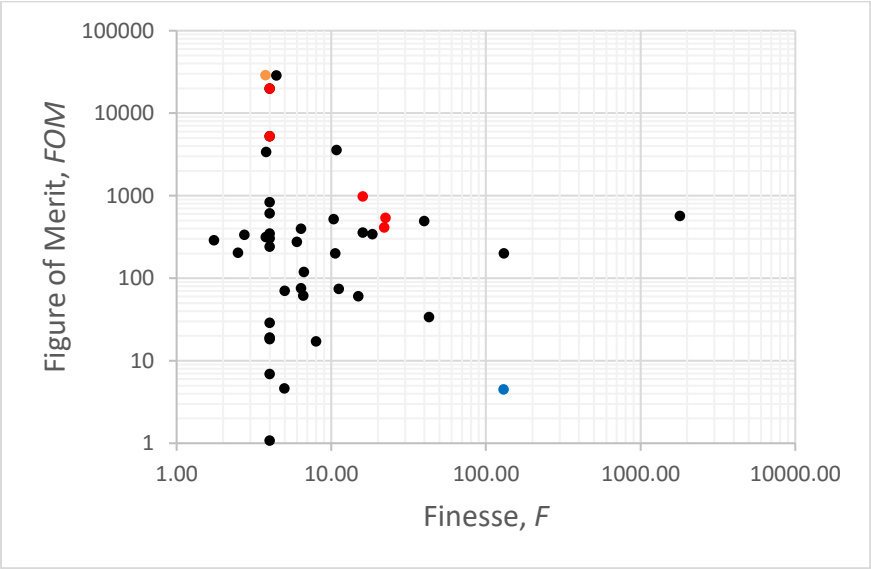

Figure 63. Finesse is one of the three design terms factoring into the equation for *FoM* for FP cavities, as per (3.5.26). Given a particular finesse, the product *fL* determines the *FoM* for a FP or ring resonator cavity.

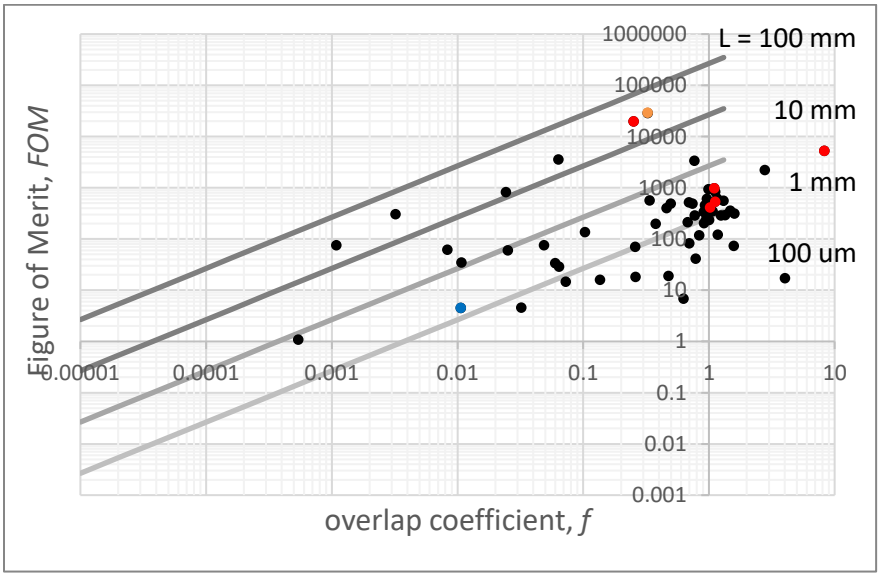

Figure 64. *FoM* correlates with the overlap coefficient, and the devices with a given *f* perform as a function of their length in the *FoM* metric as anticipated by the gray lines.

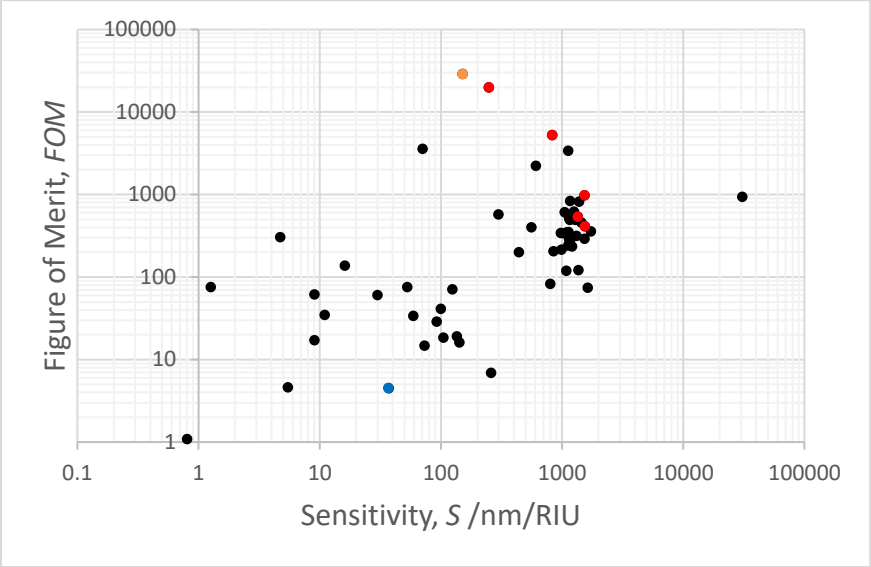

Figure 65. *FoM* and the FP cavity device sensitivity are correlated metrics as per (3.4.19). For a given *S,* the *FoM* performance of the device improves with narrower fringe linewidth. As before, the orange dot indicates the highest *FoM* device, whereas the blue dot indicates a low *FoM* device with high *F*.

A number of devices have been highlighted in Figure 61-Figure 65. These publications are reviewed below for their performance and specifications.

Figure 66 shows a bare-core in-fibre Fabry-Pérot interferometer delineated by two in-fibre mirrors. This cavity has an extremely high overlap coefficient of $f = 8.3$ and high finesse, $F = 4$, resulting in resonant peaks with narrow HWHM and, through equation (3.5.26) in a very high *FoM* = 5220. The *f* value is higher than unity, likely, due to underlying assumptions of a linear and dispersion-free response. The sensor also has a comparably high sensitivity, $S = 830$ nm/RIU, due to the short sensing length of 0.15 mm.

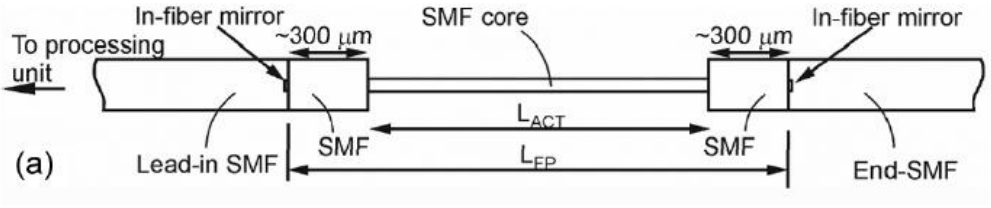

Figure 66. Schematic of a Fabry-Pérot interferometer using an SMF core microfibre [115].

In-fibre cavities containing sensor heads made from either offset-spliced fibres or microfiber gap junctions are other forms of high-*f* cavities (*f* close to unity in both cases) where the light inside the cavity largely overlaps with the sensing medium. Examples are the gas sensor depicted in Figure 67 (L = 0.135 mm, f = 1.10 F = 16, leading to S = 1540 nm/RIU, and *FoM* = 974), Figure 69 (L = 0.053 mm, f = 1.02, F = 22 leading to S = 1550 nm/RIU, *FoM* = 411), and the liquid sensor in Figure 68 (L = 0.054 mm, f = 1.12, F = 22.5 leading to S = 136 nm/RIU, *FoM* = 535) respectively. All these cavities have resultant high S and *FoM* as expected.

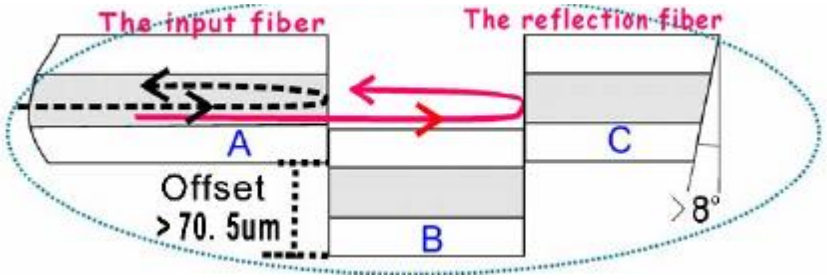

Figure 67. Schematic of an offset-splice FP cavity [114]. The cavity is formed by the Fresnel reflections from the end facets of the input and reflection fibres. The device shown is used as a gas sensor placed inside a chamber, and the reflected mode interacts directly with the sample.

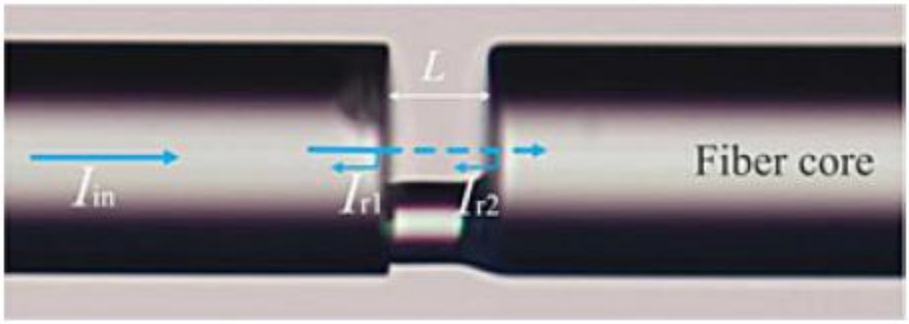

Figure 68. Schematic of a microfibre-enabled FPI [112]. A microfibre cut from a fibre taper waist is spliced between two sections of standard SMF. The cavity is again formed by Fresnel reflections from the parallel SMF fibre facets at the input and reflection fibres. Spectral response to axial force and temperature controlled RI of index-matched oils are measured. There is direct mode interaction with the analyte.

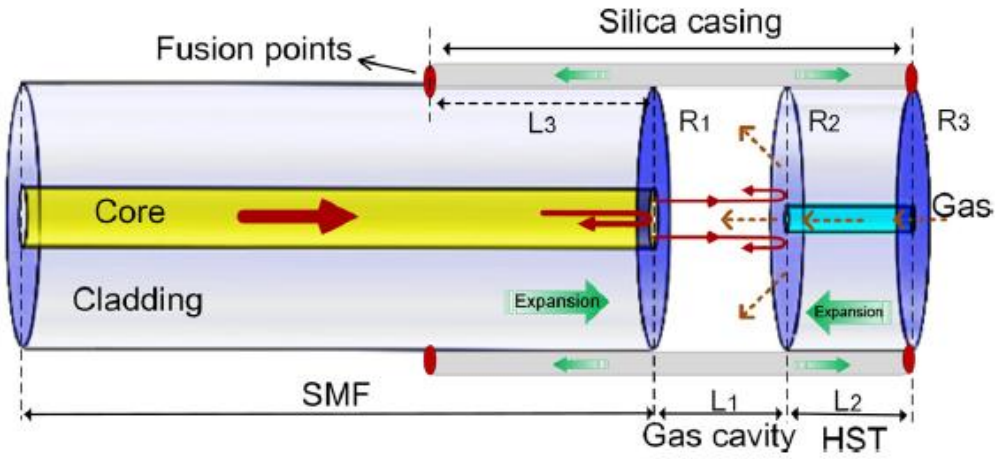

Figure 69. Schematic of an FPI gas refractive index sensor, from [118]. The cavity is filled from the HST end with gas, and as such, the reflections interact directly with the sample.

High finesse (F = 131) cavities such as the one shown in Figure 70 do not necessarily perform well in terms of the Figure of Merit. While the HWHM is quite small ($\lambda_{1/2}$ = 0.83 nm), a lower overlap coefficient of f = 0.01 and a short length (L = 0.025 mm) result in a comparatively low sensitivity S = 37 nm/RIU, and FoM = 4.47.

On the other hand, long interferometer arm lengths (*L* = 19 mm) can compensate for moderate-to-low overlap coefficients (*f* = 0.25) in Fabry-Pérot of interferometers (Figure 71) [119]. For a *F* = 4, we see a high sensitivity of *S* = 250 nm/RIU for this device to produce *FoM* = 19,800. The narrow fringe HWHM of $\lambda_{1/2}$ = 0.01 nm contributes significantly to this extraordinarily large *FoM*.

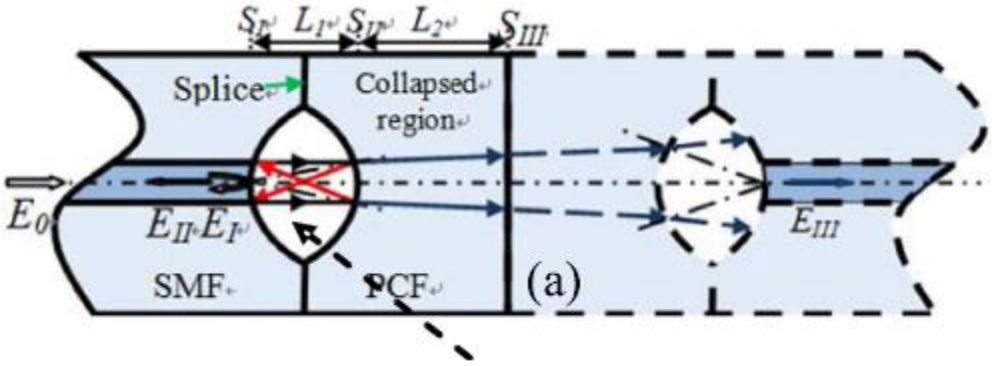

Figure 70. FP cavity with air gaps as mirrors, from [116]. This sensor is used as an evanescent field sensor while immersed in a liquid.

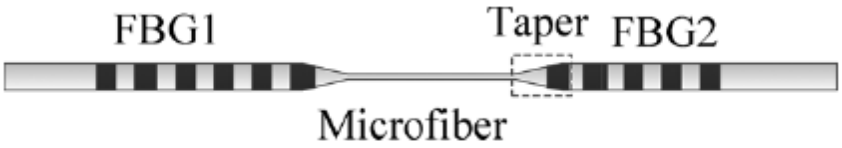

Figure 71. Microfibre-based FPI after [119]. The entire length of the microfibre, the tapered regions, and the two FBGs is *L*= 19 mm. The diameters of the microfibre is 2 μm. This sensor uses an evanescent field detection.

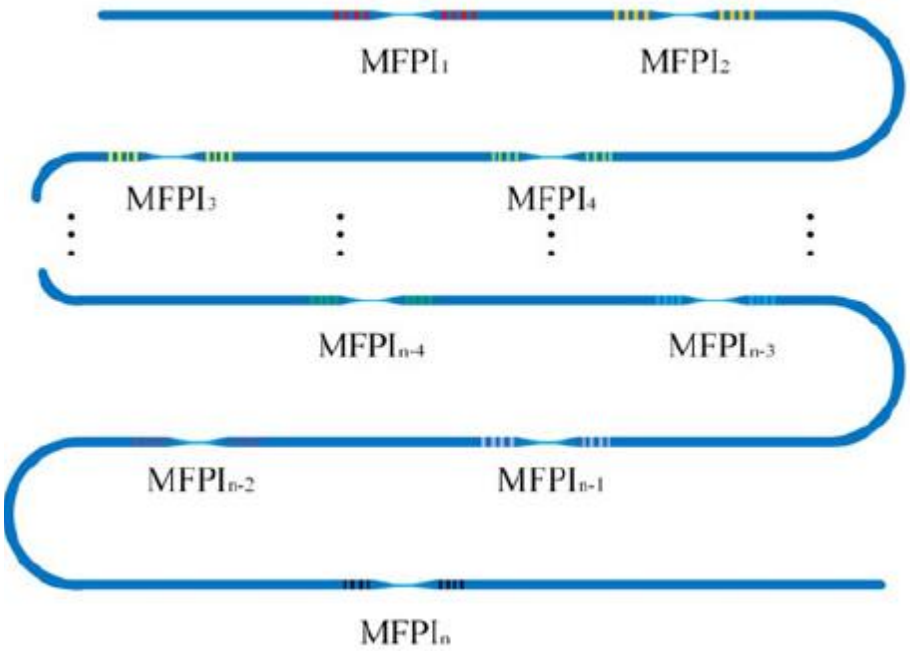

Figure 72. Quasi-distributed dual-parameter sensor based on a chain of tapered-microfibre FP interferometer. A quasi-distributed sensor is one made up of several local sensors joined by a single optical fibre. RI of liquids have been measured using evanescent field sensing. Taper diameter is 1.6 mm and the length is L = 18 mm[117].

A long chain of tapered-microfibre FPI used in [117] is shown in Figure 72. This work uses a quasi-distributed sensing scheme where each sensor's centre wavelength is located at a different part of the optical spectrum, but the optical response is combined in a single optical fibre. These different peaks can be tracked for localization of the sensing. This work achieves a f = 0.07 for a sensing length L = 18 mm and a finesse F = 3.78, resulting in S = 152 nm/RIU for the highest sensitivity sensor, and *FoM* = 28,600. It is reasonable that the different peaks have different sensitivities owing to dispersion in different parts of the spectrum.

Overall, we find that the FPI are governed by the familiar fL product, but the finesse F of the cavities also factor into this product in the determination of the *FoM.* We analyze a number of studies combining direct sensing methods with evanescent field sensors. The quasi-distributed sensor that has the highest *FoM* in this category has

the largest product owing to its extremely narrow fringes ($\lambda_{1/2}$ = 0.005 nm) achievable with the FBG structures combined with its *S* = 152 nm/RIU, despite not being a direct-sensing architecture.

3.8. Conclusions and Future Work

In this chapter, we assessed the performance of hundreds of in-fibre interferometers that belong to four different categories. We identified the Figure of Merit to be the most meaningful metric to characterize device performance and were able to tie this metric to design parameters that can be adjusted to increase device performance. We note that the Figure of Merit is based on the umbrella metric of refractive index as the physical changes of interest such as temperature, strain, concentration, and density can all be expressed in terms of this measurand. In this context, the devices with the highest Figure of Merit were those that allowed for sustained interaction of the propagated light with the sample, i.e., those devices for which both the interaction length, *L*, and the parameter governing the interaction with the sample, *f* are large. Maybe not surprisingly, the best-performing devices are based on photonic bandgap fibers, specifically hollow-core waveguides, although other designs can certainly be envisioned.

Hollow-core waveguide designs have currently only been implemented for Mach-Zehnder interferometers which then appear to be the most performant based on the highest achieved *FoM*, followed by similarly performant Fabry-Pérot and Sagnac interferometers. As Michelson interferometers are typically evanescent field based, they have lower *f* values, and the propagation length also cannot be lengthened indefinitely due to scattering losses. As a result, their *FoM*s are lower than for other types of RI sensor interferometers'.

Future designs may be based on custom designed waveguides that contain both a hollow core (as a sensing arm) and a solid core as a reference arm. They may be understood as a monolithic version of the Mach-Zehnder interferometer developed by

previous students in our group[44], which is one of the best-performing devices overall in terms of its refractive index resolution and FoM. The advantage of the proposed future design of the published device lies in its single waveguide structure. The length of both interferometer arms is identical, making this balanced interferometer immune to temperature and mechanical disturbances. Increasing the length of the instrument is therefore only limited by the practical ability to fill the hollow core with the sample.

Our FoM is a metric that draws from quantities that do not depend on the optical loss. Loss in this context would reduce the fringe visibility and therefore the modulation depth of an interferometer. Despite this degradation, the FoM defined here based on the overlap coefficient and the interferometer length is expected to be unaffected, except in the case of the FPI. The FPI-type sensors also include a metric which takes into account the finesse. This metric depends on the HWHM of the cavity in question, which would inevitably by degraded (increased) by the presence of loss.

The effect of birefringence is also not treated outside of the operation principle of the Sagnac interferometers. It is important to note that for significant differences in the refractive indices for the two orthogonal polarization states will necessitate the coupling scheme to include a polarization controller to select the higher sensitivity polarization state. Also of note is the polarization-dependent peak-splitting mentioned in Chapter 2, which is expected to affect cavity-type interferometers. Fabricating future cavity type-interferometers in polarization maintaining fibres and controlling the SOP might overcome this issue.

Chapter 4 Emission in Dye-loaded Microdroplet Resonators

4.1. Introduction

Linear cavities are the mainstay of resonator optics in that they provide a simple architecture used in the majority of lasers and cavity-enhanced spectrometers even today. In this work, we aim to demonstrate the use of a circular, traveling-wave cavity in the form of a spherical microdroplet suspended from a piece of optical fibre that can guide cavity modes via total internal reflection (TIR). These so-called Whispering Gallery Modes (WGMs) are described below in some detail (Section 4.3). The choice of a droplet microcavity is based on its easy and low-cost "fabrication", its simple alignment, and its high-quality surface owing to surface tension effects. Moreover, small modal volumes allow for strong interaction of light with the material making up the droplet, paving the way for low-threshold lasing applications[120].

A WGM can be excited in any spherical-geometry structure that can confine light via TIR. The quality of these resonators is typically measured by defining the quality factor, or the Q-factor as

$$Q = \frac{\omega}{\Delta\omega} = \frac{\lambda}{\Delta\lambda} \tag{4.1.1}$$

where ω is the resonant frequency and $\Delta\omega$ the resonant linewidth. As an example, the side-profile of a WGM in a microdroplet of paraffin is shown in Figure 73.

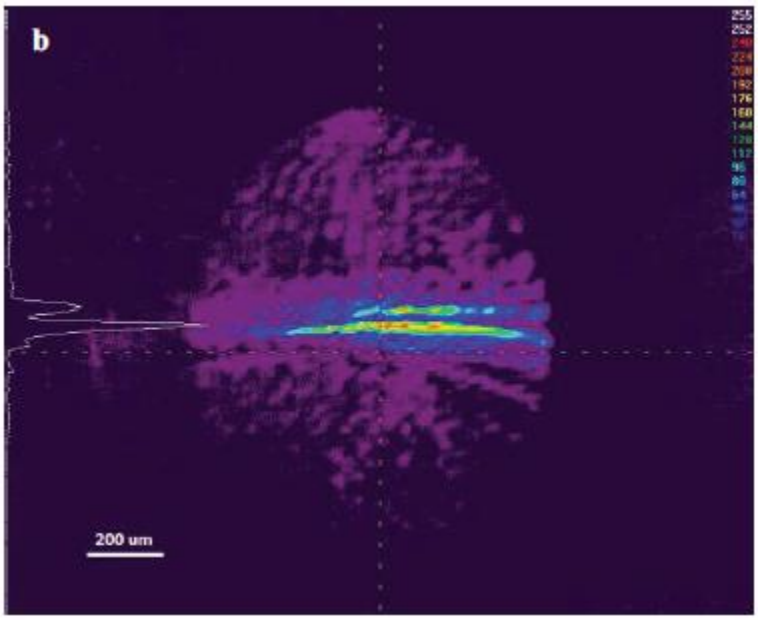

Figure 73. Whispering gallery modes excited along the circumference of a liquid paraffin microdroplet of 1.3 mm diameter taken with an infrared camera. The WGMs are excited with a 1560 nm laser. The second, fainter equatorial "belt" shows higher-order modes. Reused from [121] with permission.

Previous works have shown WGM in solid microspheres and microtoroids with quality factors (Q-factors) of up to 10^8-10^{10}, which are among the highest observed[122,123]. Dye lasing is shown in these microdroplets in the 1984 seminal work which shows continuous-wave lasing in Rhodamine 6G-loaded ethanol droplets[124]. More recent work has shown dye lasing in droplets suspended in optical traps using a pulsed laser (5 and 20 ns of pulse duration respectively) [125,126], and in droplets resting on superhydrophobic surfaces using a pulsed laser (100 ns)[127]. As can be surmised, works expanding on droplet lasing in a *continuous wave* system is lacking.

A major shortcoming of microdroplets as cavities is their changeable size resulting from solvent evaporation. In this work, we propose the use of polyethylene glycol as a low vapour pressure medium that can circumvent some of these size stability problems. This medium doubly serves as a good solvent in which to dissolve DCM, which is initially dissolved in glycerol. Previous works involving binary mixtures of water and glycerol necessitated the use of a humidity control chamber to stabilize the size of the

droplet[128-130]. We circumvent this problem for the most part using an alternative mixture based on low molecular weight polyethylene glycol[131]. Moreover, as previously mentioned, most of the previous literature works on pulsed lasers pumping the lasing medium[126,132-134], which is alternative to the continuous-wave work done in this project, but does not take full advantage of the very high Q-factor (narrow laser resonance) that these spherical cavities afford.

4.2. Literature Review

The field of lasing cavities has boomed after the first demonstration of the ruby laser by Thedore Maiman in 1960, which demonstrated emission at 692.9 nm and 694.3 nm[135]. This ground-breaking experiment has employed a 1-cm long ruby crystal that has been silvered on its two parallel faces to provide a linear resonator cavity. From there, it only took a year for the first demonstration of lasing in a solid spherical cavity in the form of lanthanide-doped calcium fluoride glass (CaF_2:Sm^{++})[136].

On the macroscopic scale, circular-path lasers were demonstrated in ring cavities using organic dyes[137], fibre loop lasers[138], and even fibre loop lasers stabilized to WGM cavities[139]. This latter combines a macroscopic ring cavity emission with a microscopic resonator to stabilize the laser operation. On the other hand, purely microscopic designs are also entirely possible. Examples of these include microscopic ring resonators [140], race-track lasers[141], and microtoroids[142]. These topologies often provide an excellent platform for the study of circular resonators however, their fabrication remains cumbersome. Here, we propose the use of a simple droplet loaded with an organic dye that maintains its surface quality through surface tension. Of all spherical resonators microdroplets are the easiest to “assemble” and allow for rapid proof-of-principle tests in the laboratory.

Liquid microdroplets are a promising platform that have first started seeing use in the 1980s with work demonstrating lasing in a free-falling stream of droplets generated from a vibrating-orifice aerosol generator. In a landmark study, Chang and

colleagues produced lasing above 595 nm in a 60 μm microdroplet pumped with a 514.5 nm CW argon-ion laser loaded with Rhodamine 6G dye dissolved in ethanol[124]. In a 1986 paper on free-falling droplets by the same group[143], Rhodamine 590 in ethanol is excited with a frequency doubled Nd:YAG at 532 nm with pulses of 10 ns width to obtain red emission at 595 nm. Partially polarized red lasing, and orange fluorescence is observed in this work. Building on this work, one needs to consider the "flow" state of these droplets: the lasing is not localized. Additionally, the variable size and shape of the droplets fabricated using this method is a cause for concern in applications that require stability.

The advent of optical traps pioneered by Ashkin and colleagues[144] paved the way for localization. This group also demonstrated the observation of WGM in liquid droplets of silicone oil[145], which has a low vapour pressure allowing for a relatively stable droplet size throughout the experiment. This effectively laid the groundwork for resonator modes that emissions could couple into, even though lasing in WGM modes was not demonstrated by this group.

More recently, a group succeeded in acoustically levitating a Rhodamine 6G-loaded ethylene glycol droplet and observing laser emission in this droplet when pumped with a frequency doubled Nd:YAG (532 nm) of 5 ns pulse width with an emission located at 577 – 580 nm[125]. This work explored the effect of different hydrophobic surfaces for droplet localization and found that lasing could be observed with all three methods for a droplet size of about R = 300 μm. The droplets places on black silicon (BS) surfaces were deformed after being optically pumped. Given that it was also difficult to obtain lasing on the grooved BS surfaces, fluorocarbon deposited silicon surfaces were the best localization option explored.

Meanwhile, a 2009 study showed both lasing and achieved a 3.6 kHz colour-switching rate by mechanically controlling the localization of droplets of R = 10 - 20 μm in a microfluidic channel[132]. In this study, droplet mixtures were flowed into a T-junction channel in alternate, and subsequent emissions at 582 - 594 nm for Rhodamine 560 and

670 - 690 nm for Rhodamine 640 droplets in benzyl alcohol were achieved following excitation with a frequency-doubled and pulsed (20 ns) Nd:YAG at 532 nm.

There has been continuous interest in droplet lasing leading into the last decade. In a 2013 study, Dil(3)-loaded droplets with R = 13.5 μm in microscope immersion oil were localized using an optical trap[126]. Emission at approximately 575 nm was observed upon excitation with a frequency-doubled Nd:YVO_4 laser at 532 nm with 20 ns pulse width.

In a follow-up study in 2015, authors have used quantum dots dispersed in aqueous borate buffer [134] to avoid photobleaching effect which so commonly plague organic dye optofluidics. In this study, an optofluidic ring resonator of an inner radius R = 35 – 45 μm was used and the ring was used as a container, or its inner surface was immobilized with commercial quantum dots in two subsequent experiments. The excitation laser used was an optical parametric oscillator (OPO) emitting at 433 nm with a pulse width of 5 ns. Emission was observed in the 660 – 665 nm region.

Raman lasing was also shown recently in glycerol-water microdroplets[146]. As opposed to previous works that build on cavity fluorescence to start the lasing process, this work focuses on Raman scattering coupled to WGMs of a glycerol-water microdroplet resonator.

The fluorescence and Raman processes that might be at play in building a dye-loaded microdroplet resonator are shown in Figure 74. In part (A) of the figure, a simple absorption process is shown. Absorption contributes to some of the losses observed in any resonator cavity. In (B), the elastic Rayleigh scattering is shown as a photon is absorbed to a virtual state and a photon with the same energy difference between the ground (GS0) and virtual excited state is emitted. In (C), we show Raman scattering as a photon is absorbed to a virtual excited state, and another photon corresponding to a lower energy difference between the virtual excited state and the first vibrationally excited level of the ground electronic state (GS1) is emitted. In this process, it is important to note that the energy difference between the excitation and emission photons (the Stokes shift) corresponds to the energy difference between two vibrational

energy levels of the dye molecule in its electronic ground state. Conversely, in (D), a photon is also absorbed to a virtual state, but now the emission of a higher energy photon occurs. This is only possible if the ground state is in originally in a higher vibrational level (GS1) than the final ground state (GS0). Again, the energy difference (anti-Stokes shift) is indicative of the vibrational energy level differences of the dye molecule in its electronic ground state. In (E), resonant Raman process takes place as the excitation and the subsequent emission happens with an actual electronic state involved in the transition, from the lowest ground state (GS0) to an intermediate excited state (ES1) and down to a higher vibrational level of the electronic ground state (GS1). (F) shows a basic fluorescent process where a photon is absorbed to a higher electronically excited state (ES2), and then non-radiatively relaxes to a lower vibrational level of the same excited state (ES1) before emitting a photon corresponding to the energy gap between the lower excited state (ES1) and one of the many vibrational levels of the ground state (GS0-GS2). Finally, in (G) we see coherent anti-Stokes Raman Scattering (CARS) take place as a photon is excited to a virtual state, and then decays to a ground state (GS1). This process is then followed by a re-excitation, again to a virtual state, and is followed by a decay to the lowest ground energy state (GS0). In this process two identical photons are used for excitation and are converted in two photons with energies that are Stokes-shifted and anti-Stokes-shifted from the excitation energy.

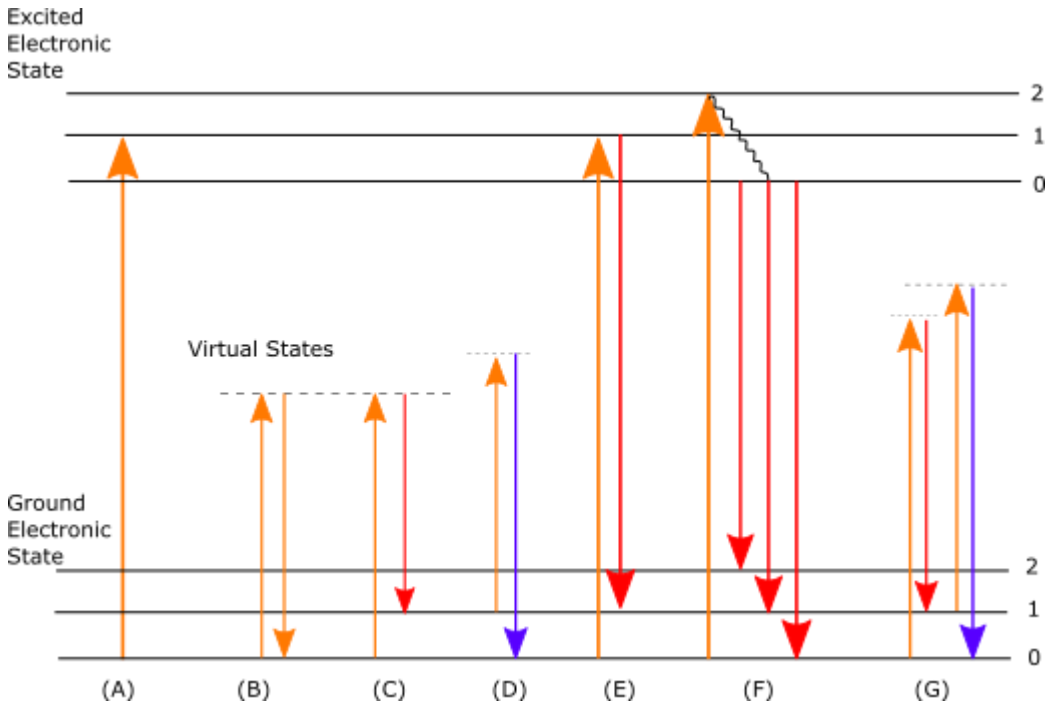

Figure 74. Jablonski diagram showing different emission processes, adapted from[147]. The diagram shows (A) absorption, (B) Rayleigh scattering, (C) Raman Stokes shift, (D) Raman anti-Stokes shift, (E) resonant Raman scattering, (F) fluorescence, (G) coherent anti-Stokes Raman spectroscopy. The numbers represent the level of vibrational energy state.

4.3. Whispering Gallery Modes

A "whispering gallery" is a dome-like structure in which the whisper of a person can be heard by a second person standing at the opposite side of the dome. Sound travels along the curved wall of the dome by reflection until it reaches the ear of the listener. This phenomenon has been observed by Lord Rayleigh in St. Paul's Cathedral in London[148], but many other historic documents on the phenomenon exist. The Whispering gallery modes (WGM) refer to acoustic and optical resonances confined by these circular cavities and are found in both macroscopic and microscopic cavities. Optical WGM correspond to light waves that are trapped inside circular or spherical optical cavities via total internal reflection (TIR). If the incident light is coherent and the cavity is not too large, an optical resonance is formed whenever the wavelength of the

light is an integer multiple of the cavity length, i.e., the circumference of the droplet. Cavities that sustain WGM are examples of traveling wave cavities and fall under the class of non-reflective cavities. Most WGM resonators described to-date are low-loss, high-Q, small mode volume cavities that allow for low lasing thresholds with narrow linewidth emissions. The low-threshold lasing is particularly useful in biological and living tissue applications where damage thresholds are low[149].

Optical cavities are usually characterized by their quality (Q) factor. The Q-factor, as described in (4.1.1) for resonators, is a measure of the damping of a system. As such, the Q-factor is related to the ring-down time.

The Q-factor can also be described as the ratio of the energy stored in a resonator over the dissipated energy. Alternatively, it is the ratio of the resonant frequency over the resonance linewidth.

$$Q = 2\pi \frac{E_{stored}}{E_{dissipated}} = \frac{\nu_0}{\Delta\nu} \tag{4.3.1}$$

As the imperfections in the material and surface of the resonator reduce the Q-factor by reducing the resonance lifetime[150], it is of utmost importance to produce cavities that are exceptionally uniform. In this work, we take advantage of the surface tension of liquids to suspend microdroplet cavities in which chemical dyes are dissolved for lasing applications.

Silica microspheres have been frequently used to characterize the ability of microscopic optical cavities to sense refractive index changes[151], surface coverage, temperature changes, etc. Silica spheres having a diameter of 10's to 100's of micrometers frequently reach Q-factors can 100 million, limited only by the transparency of silica[152]. Liquid microdroplets have lower Q-factors of up to 16 million [153,154], but their ability to dissolve chemical dyes allows for simple "assembly". By contrast to solid spheres, microdroplets have a few pervasive problems: hygroscopicity of the liquid may change the composition of the sphere over time, especially in humid environments. Solvent evaporation conversely reduces the size of the droplet and thereby also changes the resonance frequencies. Many solvents either absorb moisture

from air and thus increase the cavity size or have high vapour pressure such that they evaporate and reduce the cavity size. In this work, we dissolve a fluorescent dye (4-(Dicyanomethylene)-2-methyl-6-(4-dimethylaminostyryl)-4H-pyran, DCM) in glycerol before incorporating it into polyethylene glycol liquid droplets (PEG 400). PEG is viscous liquid with a low vapour pressure (low volatility) and low hygroscopicity. The fluorescent dye DCM is a common laser dye, and it was our intention to achieve continuous-wave (CW) lasing in these microdroplets.

In order for lasing action to start, the net optical gain in a cavity needs to surpass the losses in that cavity. This can be expressed as

$$\begin{aligned} &2\pi r\left(1-\alpha\right)\exp\left(2\pi r g_{threshold}\right)\exp\left(-2\pi r\alpha\right)<1 \\ &g_{threshold}<\alpha-\frac{1}{2\pi r}\ln\left(2\pi r\left(1-\alpha\right)\right)\Big|_{\alpha=\alpha_0} \end{aligned} \tag{4.3.2}$$

where in (4.3.2) both the exponent form and the linear form are given as per [155], adapted for a WGM laser. In this equation, α is the absorption coefficient per unit length, $2\pi r$ is the circumferential cavity length, and $2\pi r\left(1-\alpha\right)$ is the reflectivity of a circular cavity, in other words, the proportion of power that remains circulating. An estimate for the output power at threshold can then be found by multiplying both sides of the linear equation by the circular resonator length, $2\pi r$:

$$P\propto 2\pi r g_{threshold}=2\pi r\alpha_0-\ln\left(2\pi r\left(1-\alpha_0\right)\right) \tag{4.3.3}$$

One can then calculate the lasing threshold output power for a dye-loaded droplet of 0.575 mm radius, but it must be noted that the absorption loss for a DCM-loaded PEG/glycerol droplet is not known, much less at the particular concentration of interest. We therefore resort to obtaining the threshold gain from the cavity losses using the Q-factors of one of the reflection resonances shown in Figure 81. For a given $Q=\frac{\omega}{\Delta\omega}=\omega\tau$ we can rewrite the ringdown time as $\tau=\frac{t_r}{\ln\left(\kappa_r\right)}$, which is in terms of round-trip time t_r and the natural logarithm of the round-trip loss κ_r [156]. Using these, we obtain a lasing threshold of 4 mW. Lasing thresholds for microdroplet cavities are

typically on the order of tens of uW[126] to tens of mW[125], and are function of the size of the cavity as well as the dye concentration. Additionally, experimental determination of the lasing threshold is necessary to deem lasing action as having started in a cavity.

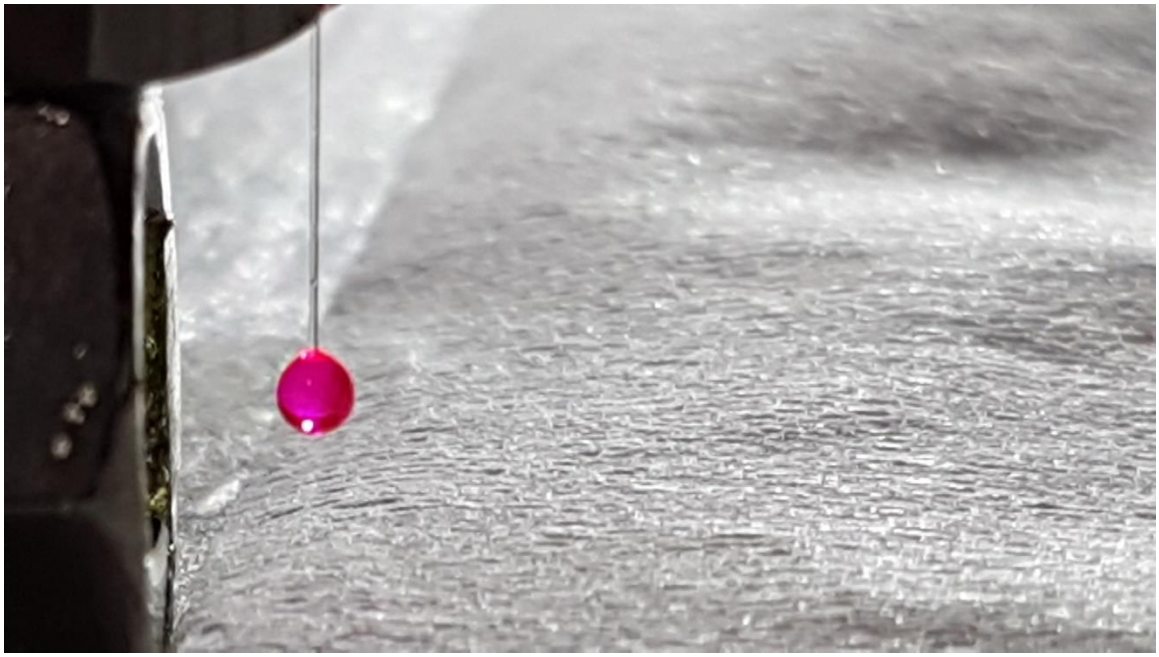

Figure 75. A microdroplet of glycerol in PEG 400 with DCM dye suspended from an SMF-28 fibre tip.

Exciting WGMs in a microdroplet cavity can be done using a free-space laser coupling architecture. Aligning the beam waist tangentially with the rim of the droplet using a translation stage, one can excite modes just below the liquid surface which are then guided by total internal reflection (TIR). Coupling conditions dictate whether fluorescence or amplified spontaneous emission (ASE) dominates. A schematic of the experimental setup is presented in Figure 76. In this figure, laser radiation at 470 nm (Toptica DL Pro) passes through a polarization controller (PC) and is split into two paths using a beam splitter (BS). The diverted ray goes into a commercial Fabry-Pérot interferometer (Toptica FPI100) whose length can be scanned using piezoelectrically controlled mirrors. The beam that propagates through the beam splitter then is redirected using two mirrors (M). These mirrors, together with a fibre collimator used in reverse allow for the laser light to be coupled into the fundamental mode of the single-mode fibre (SMF). This coupling requires a spatial overlap of the input beam (expected

to be Gaussian) and the fundamental mode that is expected to be excited in the single-mode fibre. The polarization of the input beam is controlled using a second PC before the microscrope objective, as coupling between the circumferential, spiral-like WGMs and the free-space beam requires maximizing the spatial overlap between two disparate mode profiles. The suspended droplet profile is also slightly elliptical, which would introduce an element of birefringence visible in the spacing of the WGM modes on the OSA. The output beam is again collimated using a fibre-mounted component and is redirected using another mirror into a second polarization controller before being redirected towards the coupling objective (OBJ) mounted on a linear translation stage. The focal point is aligned with the microdroplet resonator to excite whispering gallery modes in the excitation wavelength. Side-scattering and transmission are both collected using additional microscope objectives and are eventually coupled into photodiodes for detection. The stability of the droplet size was inferred by the stability of the WGM spectra shown in Figure 81 over the course of the experiment. It is possible to measure the evaporation rate of our droplets by placing a droplet on a hydrophobic surface and measuring the evolution of its size over the course of a set time period (e.g., 24 hours).

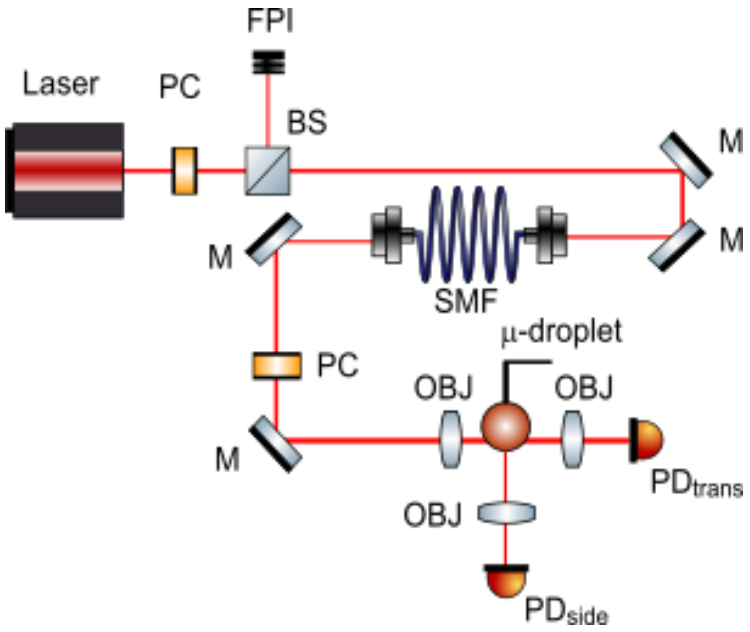

Figure 76. Free-space coupling setup for the microdroplet resonators. Free-space beam is coupled into a SMF to clean the mode profile. The first polarization controller

(PC) coupled with the polarizing beam splitter (BS) at the output of the laser split the into two paths, one launching a beam into the commercial Fabry-Perot interferometer and the other coupling into the mode-cleaning SMF, which is used to ensure that the beam coupled into the droplet is Gaussian in shape. At the output of the SMF, another PC aligns the state-of-polarization in order to excite WGMs at 470 nm. Spectra are acquired using an Ocean Optics Maya spectrometer during experiments, and light is collected directly using photodiodes during alignment.

4.4. Fluorescence in Microdroplets

DCM laser dye (4-(Dicyanomethylene)-2-methyl-6-(4-dimethylaminostyryl)-4H-pyran) is a common red laser dye that has been of interest in converting 488-nm and 514-nm radiation into tunable radiation in the 600-730-nm region when used in ethylene glycol[157]. DCM dye is also known as “red fluorescent dye” in the literature, and its absorption-emission profile has been studied in a wide range of solvents[158]. DCM exhibits large fluorescence quantum efficiency, a large Stokes’ shift, and solvatochromic behaviour. Owing to this large Stokes shift, the excitation and emission spectra of DCM barely overlap – a fact that was exploited in developing red dye lasers based on this chemical. The DCM dye absorption spectrum is strongly dependent on the polarity of the solvent. DCM exhibits two absorption peaks where the longer wavelength band is more strongly absorbing than the shorter wavelength band. The longer-wavelength band is also more structured in non-polar solvents than in polar solvents. In polar solvents, a structureless longer-wavelength band is observed with a maximum at 482 nm and a shoulder at 350 nm. The absorption maximum undergoes a redshift with increasing polarity of the medium, an effect known as the solvatochromic effect. Due to this effect, the absorption and emission of DCM dye needs to be determined empirically in each target host medium as has been done by our group Figure 77. Dissolving DCM dye in minute amounts of glycerol and then in PEG 400, we take advantage of the solvent polarity to redshift the absorption to 540 nm with a red fluorescence emission located at 600-650 nm peaking around 625 nm. In the emission spectrum used for the droplet experiments (Figure 78, PEG 1000), we see scattered laser excitation light at 470

nm with a strong fluorescence emission peaking at 582 nm.

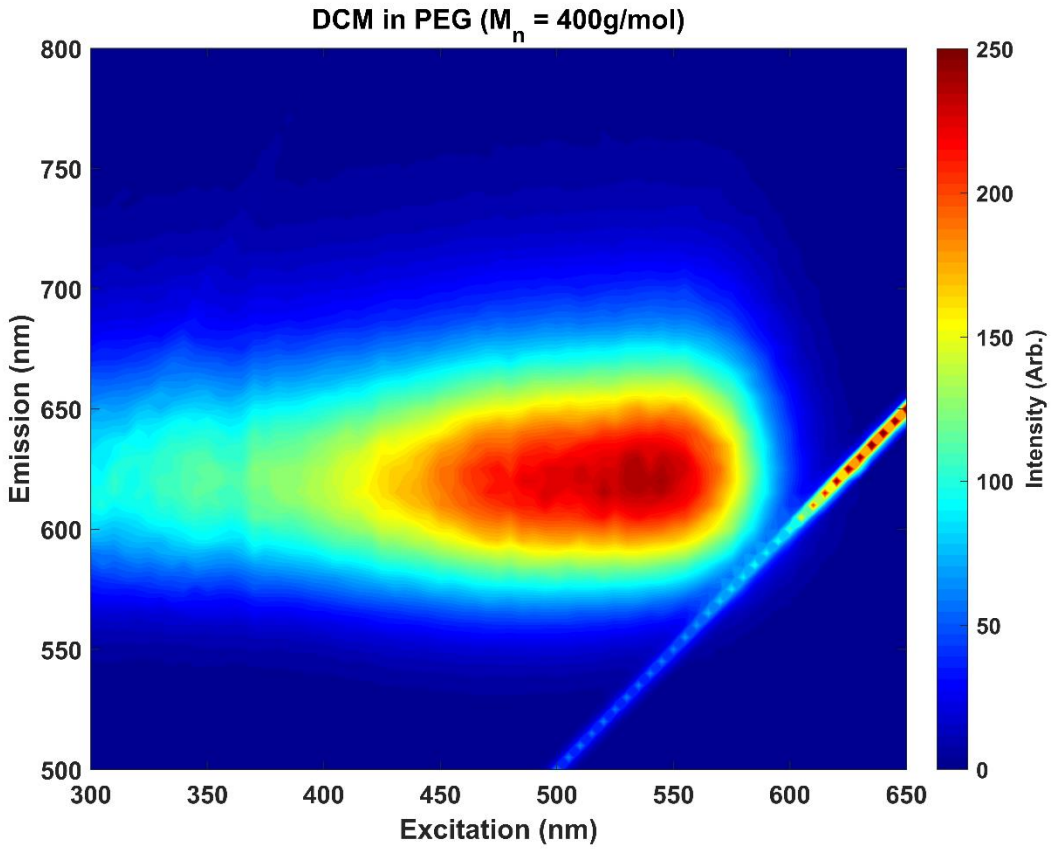

Figure 77. Excitation-emission spectroscopy for DCM dye in PEG 400 collected by Adam Bernicky, Loock Lab.

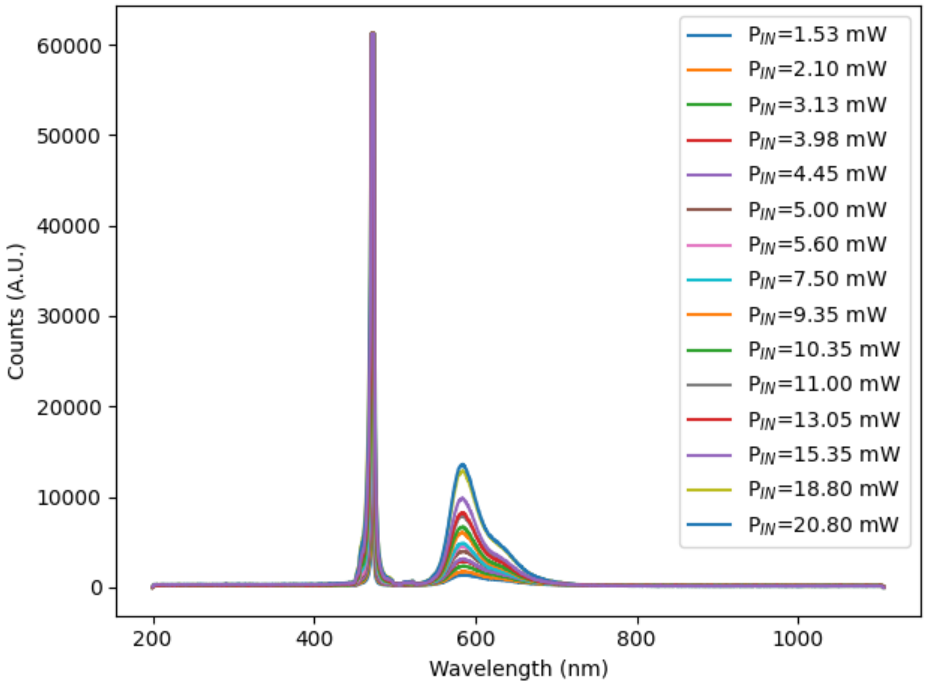

Figure 78. Amplified spontaneous emission in blue-excited microdroplet resonators loaded with DCM dye.

Figure 79 shows the power dependence of the integrated counts of photons for the fluorescence peak. Of note is the large offset from the origin at zero pump power, most likely due to a lack of dark spectrum subtraction. The isotropic emission was collected using a microscope objective in the transmission direction. This emission can be excited by coupling the incident blue light into the WGMs of the resonator. Fluorescent power is seen to increase linearly with pump power in Figure 79, which is reasonable as the process grows linearly at low pump powers before a certain threshold, after which power grows linearly but at a much higher rate [125]. Moreover, the emission is isotropic, as is the case with fluorescence.

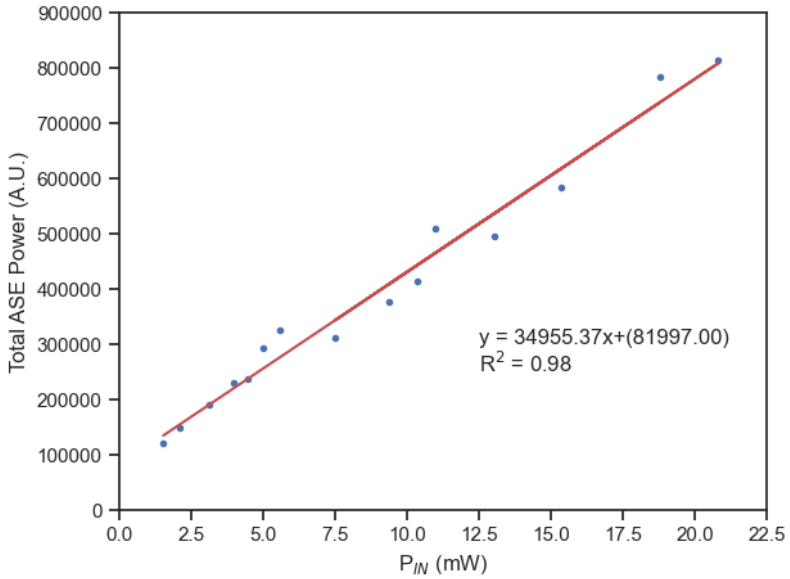

Figure 79. Power dependence of ASE in dye-loaded microdroplet resonators. No thresholding behaviour is observed at these pump powers. The zero offset is most likely due to a lack of background subtraction.

4.5. Amplified Spontaneous Emission in Microdroplets

After optimizing coupling using the microdroplet location with respect to the waist of the Gaussian laser beam to see narrow spectral emissions, Figure 80 shows a narrow-linewidth emission in the green region (518 nm) upon excitation with the same 470 nm light as in Figure 78, but no isotropic fluorescence. The narrow linewidth emission is shown delineated by the green vertical lines and is collinear with the pump in both directions, indicating that its origin is either an ASE process or a Stimulated Raman Scattering process. Depending on the exact coupling conditions, broadband fluorescence shown in Figure 78 or narrow-linewidth ASE in Figure 80 can be emitted from the droplets. The narrow width of the fluorescence process likely arises from it coupling to high-quality resonator modes in the microdroplet. The baseline dipping below zero is an artifact of the spectral collection and background subtraction on the spectrometer and is therefore not physical.

WGMs are shown in Figure 81 , both in reflection and (weakly) in transmission. The inset shows the fringes of a commercial Fabry-Pérot interferometer which provided

wavelength calibration. The adjacent WGM differ only by the mode number *m* given that $2L = mn_{eff}\lambda$ (assuming $n_{eff} = 1$ for the commercial cavity considered here).

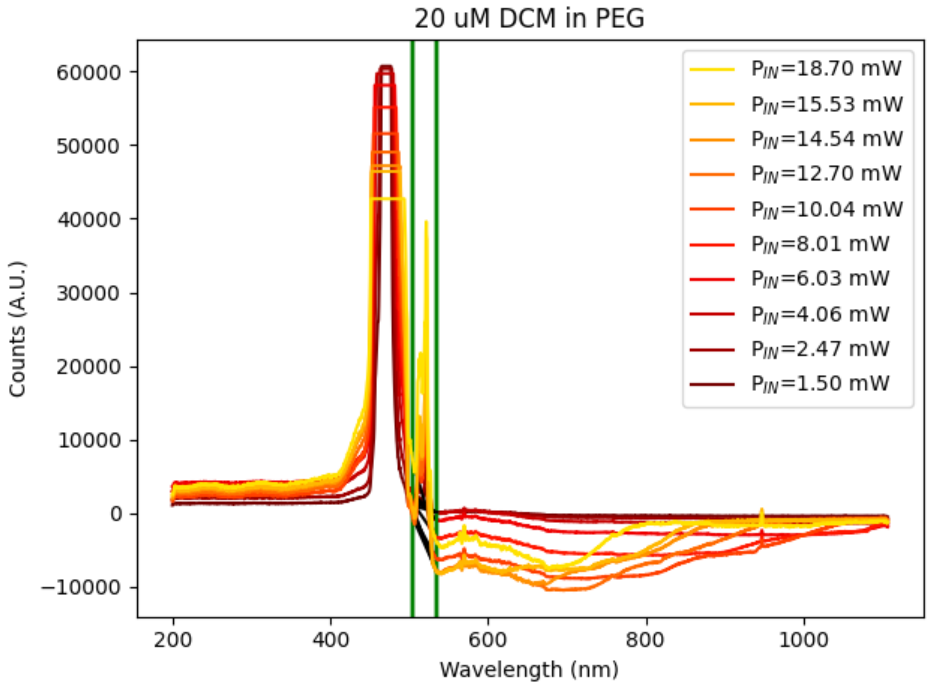

Figure 80. Narrow linewidth green emission in dye-loaded microdroplet resonators.

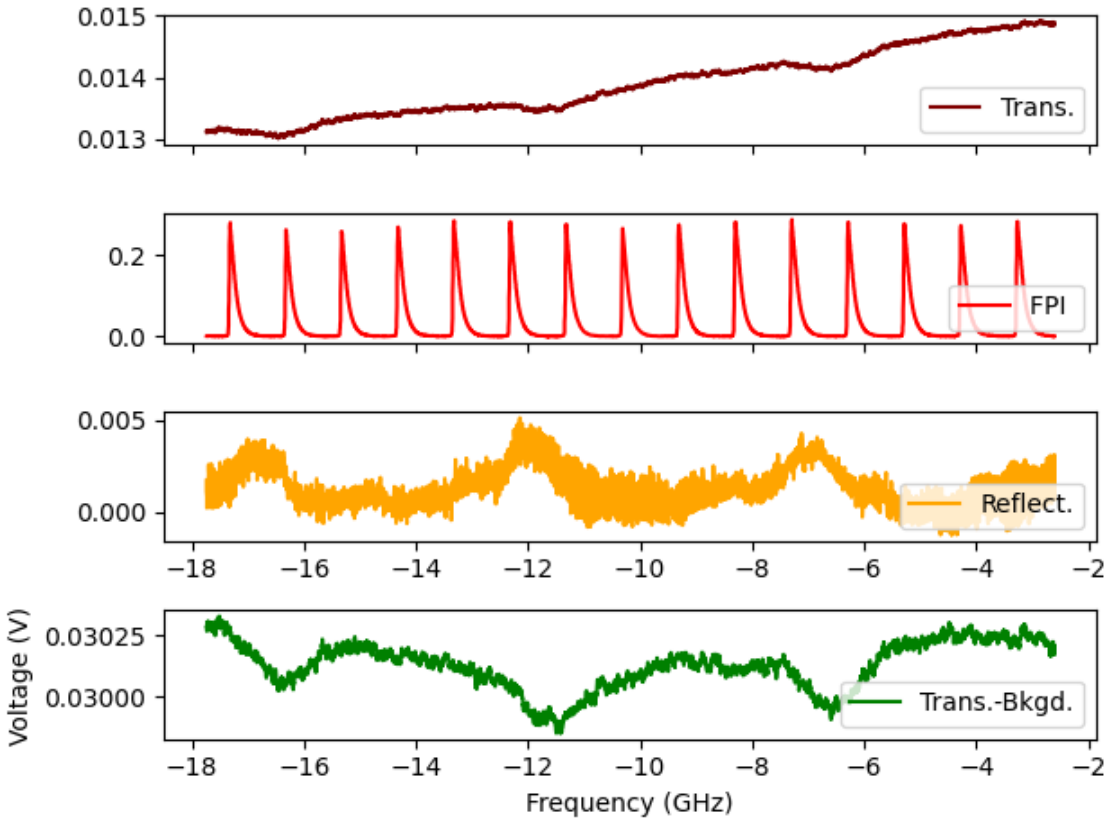

Figure 81. WGMs excited at the blue excitation wavelength in dye-loaded microdroplet resonator, showing 1.2% coupling efficiency. Q-factor of one of the reflection resonances is approximately 425,500. The first subplot shows the raw transmission data overlaid with the laser scan, while the second subplot shows the output of a commercial Fabry-Pérot interferometer for the excitation wavelength. This second plot serves as a "ruler" against which the WGM spectrum is calibrated. The third subplot illustrates the WGMs in the reflection direction, whereas the final subplot shows the transmission-direction WGMs with the linear background subtracted.

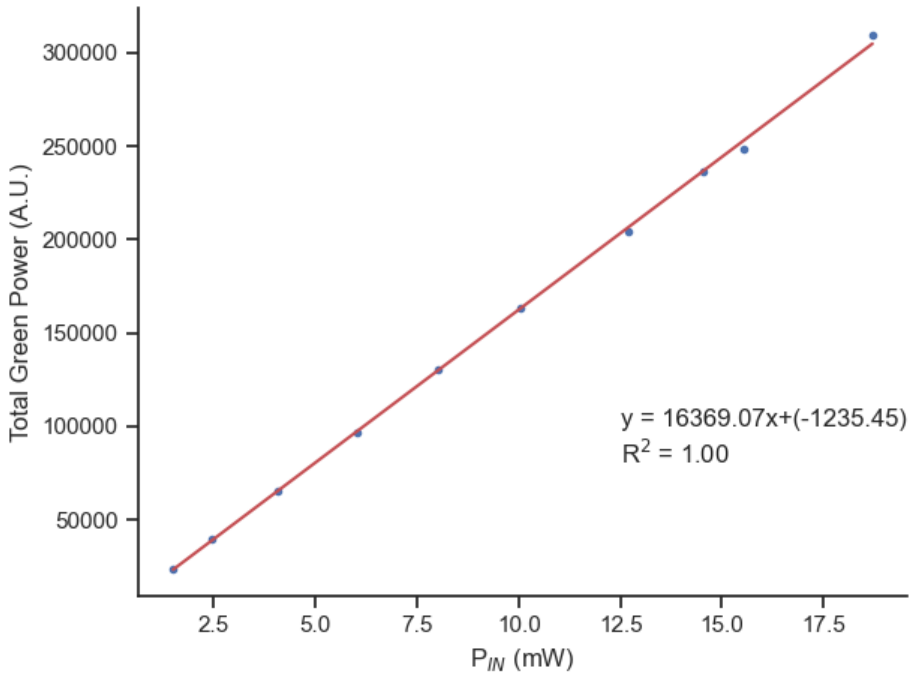

Figure 82. Power dependence of narrow-linewidth green fluorescence emission in dye-loaded microdroplet resonator.

Integration of the counts for the green peak seen in Figure 80, after the subtraction of the linear baseline (shown in black), yields the power in the emission wavelengths. The dependence of output power in this band on the laser pump input power is shown in Figure 82. No thresholding behaviour is observed for this emission line as would be expected for laser emission. This may indicate either a higher laser threshold, or that the emission is not caused by lasing but by other phenomena.

A slightly different coupling scenario is shown in Figure 83 where both green (522 nm) and red (570 nm) emissions are excited, shown delineated by the vertical green and red lines. The Fabry-Pérot modes excited in the interferometer seen in Figure 84 provide insight into the coherence features of the green emission seen in Figure 83. Given the bandwidth of the green emission (0.037 GHz), the coherence length can be calculated according to $L_{coh} = c/\left(\pi\Delta\upsilon_{FWHM}\right)$ to be 1.3 m. The degree of coherence

shown in Figure 84 can be more accurately determined by the use of self-heterodyning methods to determine the linewidth of the green emission at 522 nm.

Indeed, it would be very interesting to see the coherence of the red, narrowband ASE signal seen in Figure 83 and potentially seed it with a laser coupled to the WGM modes of the resonator. The dependence of the microdroplet emission output power on the launched power is shown in Figure 85. If the droplet was indeed lasing we would expect to see a threshold near 4 mW by the above estimate. Currently the evidence for this thresholding behaviour is inconclusive and Fig 85 does not provide strong evidence for laser action.

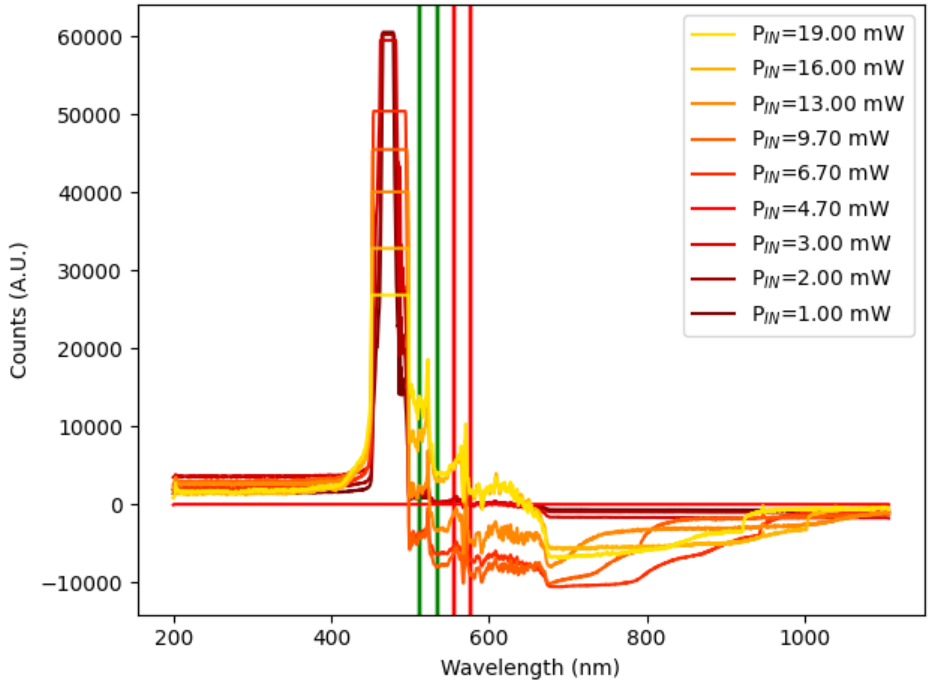

Figure 83. Narrow linewidth green and red emissions in blue-excited dye-loaded microdroplet resonators upon excitation at 470 nm. The negative counts are an artifact of the spectrometer integration time.

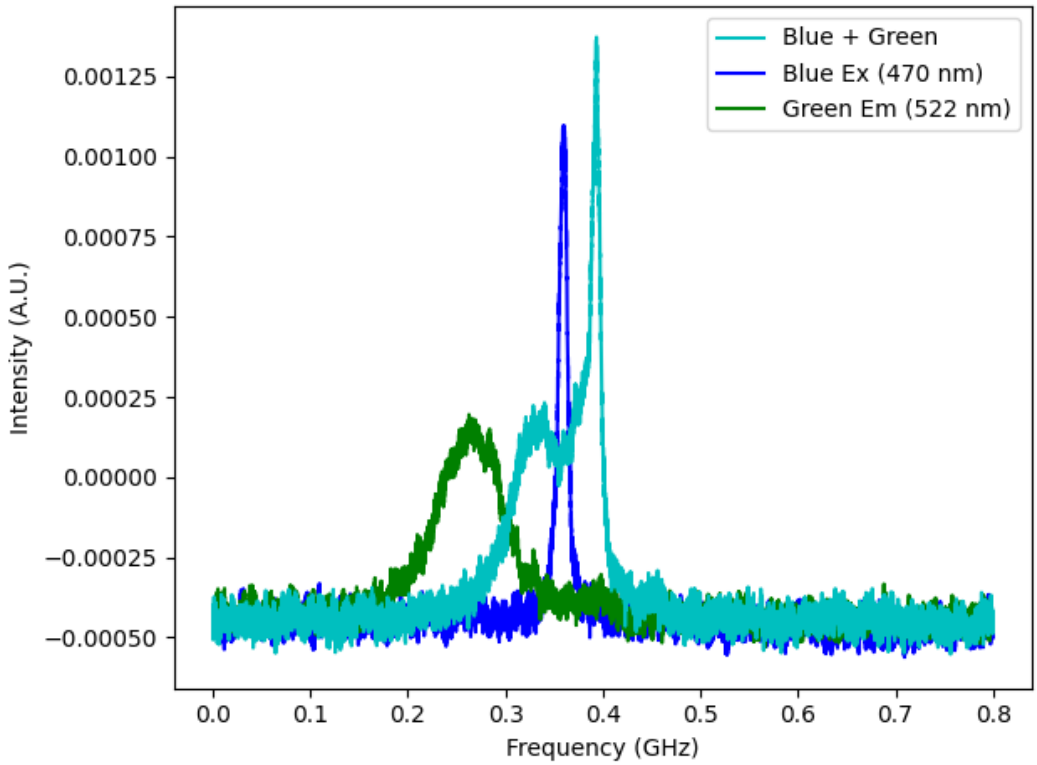

Figure 84. Coherence of blue excitation light, and the emitted narrow linewidth green light using a Fabry-Pérot interferometer. This figure illustrates that the green emission is coherent. The modes of the blue excitation can be seen overlaid with the modes of the green emission. We isolated the green emission by physically blocking the beam.

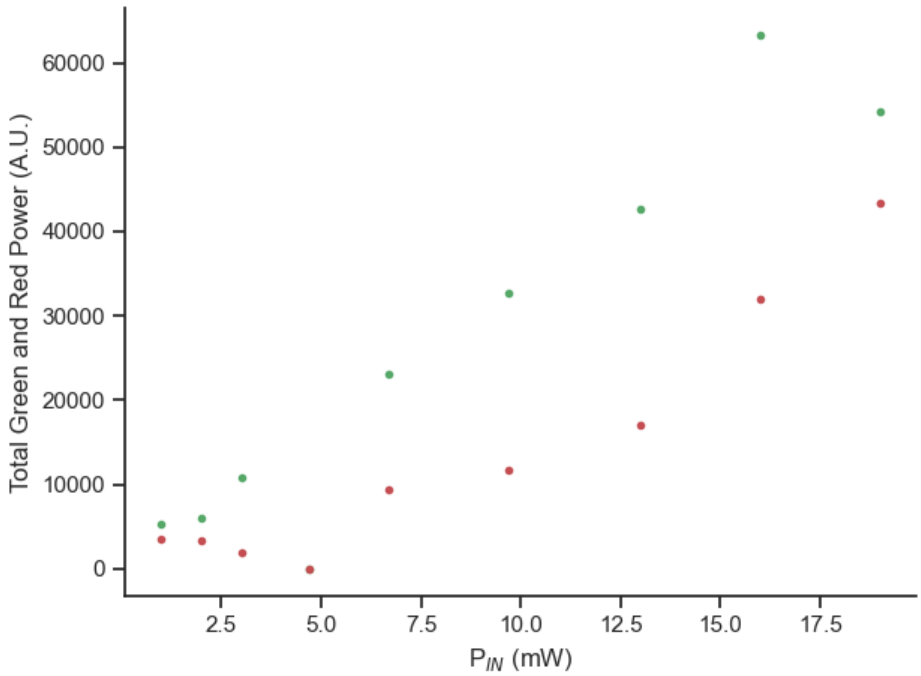

Figure 85. Power dependence of the narrow linewidth green and red light. The total integrated power increases slowly at first and appears to increase linearly, but the evidence is not conclusive for the presence of a threshold.

4.6. Conclusions and Future Work

The results outlined in this chapter show that narrow-linewidth emission can be achieved via spontaneous emission in dye-loaded microdroplets upon excitation with light at 470 nm. The natural next steps then would be to seed the narrow ASE processes at 522 nm and 570 nm to distinguish whether these can lead to lasing when excited with a laser coupled to the WGMs of the microdroplet resonator. Spontaneous Raman scattering is not likely the underlying cause of this droplet emission as the process is expected to produce incoherent light [159], whereas we observe in Figure 84 a clear coherence in the 522 nm emission which could indicate an ASE process or Stimulated Raman Scattering process. Further characterization of the 570 nm emission in terms of coherence is necessary. When increasing the pump power, we may be able to observe a lasing threshold for the 522 nm emission, as per (4.3.3).

Overall, we find that the binary mixture of glycerol/polyethylene glycol 400 serves as a very stable solvent for dissolving the DCM laser dye, with the blue WGM modes stable over the course of several hours when the droplet is suspended from a segment of optical fibre glued to a nut. We characterize both broadband and narrowband spontaneous emissions from this dye to pave the way to further microdroplet laser studies that can build upon the continuous wave lasing work discussed earlier in this chapter. We find that the narrowband green emission at 522 nm could be a promising first step towards building a CW microdroplet laser if coupled to a resonator mode. The emissions observed so far are all expected to be multimode, and single mode operation is feasible through adjustments to the size of the droplet and dye concentration.

Further studies in this area might also include the simulation of lasing in WGMs in spherical resonators using commercial software, which might help confirm the calculated lasing threshold and optimal dye concentrations.

Chapter 5 Conclusions

In this thesis, we explore a number of wave-guided standing- and traveling-wave cavities and interferometers for sensing and emission applications. In Chapter 2, we make use of a π -shifted FBG and fully characterize it for earthquake sensing applications in terms of its strain sensitivity, frequency response, rate of maximal strain change, limit of detection of strain, its noise spectrum while using lock-in detection, and its signal-to-noise while using oscilloscope detection. We find that due to the much larger linewidth of the resonant feature in a π -FBG, the lock achieved is not as good as the FP-FBG previously used by our group, even though the present sensor overcomes the previous issue of birefringent peak-splitting. This "less-tight lock" is reflected in a large error margin in the sensitivity measurement as well as a 25-times larger strain resolution limit compared to previous results from our group. Keeping these results in mind, we suggest the use of a sensor that is able to combine the desirable features of *both* polarization insensitivity, and the narrow linewidth, and pave the way for localized, robust, and temporally stable remote sensing using FBGs. These may be afforded either by longer π-FBG structures, or by isotropically written FP-FBGs.

Chapter 3 outlines important parameters to critically assess most of the literature on in-fibre interferometry. We describe the importance of *Figure of Merit* as the most important, architecture-independent parameter for performance and relate it to the product of two design parameters, the sensitivity coefficient *f,* and interferometer arm length *L*. In all categories of interferometers, we see that larger *f* devices necessitate a shorter sensing arm *L* as larger overlap with the sample implies poorer waveguiding, and therefore a limited propagation length. Specifically, for Mach-Zehnder interferometers (MZI), owing to the large dataset at hand, we can clearly see the tradeoff between *f* and *L* in the different groups of sensors able to achieve a high *fL* product, and therefore a high FoM. These two metrics of *f* and *L* are typically inversely correlated with one another, however, there are architectures that are able to "escape" the parameter space represented by this tradeoff. These are direct sensing methods that employ photonic bandgap guiding, such as hollow-core PCFs.

Michelson interferometers (MI) show a similar tradeoff between the design parameters *f* and *L.* The overlap coefficient can be high in the particular designs that employ direct sensing methods; however, the length is quite limited in these designs owing to the previously discussed issue of waveguiding, particularly as the optical path is traced twice. Overall, the product *fL* and therefore the FoM remain below those of the MZI in all devices reviewed in this chapter.

Generally, the reviewed Sagnac interferometers have lower overlap coefficients than the previous two categories of interferometers due to their design, which typically involves evanescent wave sensing rather than any direct sensing methods. Stronger waveguiding feature then implies greater length of the sensing arms. Despite the limited overlap with the sample, it is then possible to achieve FoMs competitive with most of the MZI and even supersede the performance of MI, despite the fact that the bandgap guiding structures discussed in the MZI will likely continue to outperform Sagnac interferometers.

The Fabry-Pérot interferometers (FPI) used in 3.7.5 are optimized through a triple product of the usual *f* and *L* but also the *finesse* (*F*) of the cavity. This latter can be optimized by increasing the free spectral range (FSR) of a cavity, done by decreasing the path length, or by increasing decreasing the half-width half maximum (HWHM) of the cavity by mitigating the losses. Of note is the fact that the finesse then is at odds with the length *L* of the interferometer in this case. Indeed, most of the high FoM works reviews in this subsection owe their performance to high *f* resulting from large evanescent field overlaps with the sensed material, or a direct sensing architecture. Direct sensing is possible with this type of interferometer because the FPI requirement has the built-in functionality of a cavity which can then be filled with a sample. Overall, we evaluated the performance of hundreds of devices and were able to propose a novel interferometer design informed by this evaluation.

Chapter 4 demonstrates the use of a CW laser and a pendant glycerol/PEG binary mixture microdroplet loaded with DCM dye spontaneously to emit narrow linewidth coherent light. The emission can, in the future, be seeded for stimulated emission which

can then be coupled into one of the high-Q WGM modes for lasing applications. We demonstrate that excitation of the WGMs at 470 nm is sufficient to both generate fluorescence spectrum at 582 nm and narrow linewidth ASE spectra at both 522 nm and 570 nm. This work demonstrates the feasibility of producing a micro-scale droplet laser based on DCM dye in the CW operation regime.

Chapter 6 Bibliography

Uncategorized References

1 K. Schulz, (The New Yorker, Online, 2015), Vol. 2021.

2 Yun-Jiang Rao, Measurement Science and Technology **8** (4), 355 (1997).

3 Ian C. M. Littler, Malcolm B. Gray, Jong H. Chow, Daniel A. Shaddock, and David E. McClelland, Optics Express **17** (13), 11077 (2009).

4 G. Gagliardi, S. De Nicola, P. Ferraro, and P. De Natale, Optics Express **15** (7), 3715 (2007).

5 U.S. Geological Survey, (2016), Vol. 2021.

6 International Seismological Centre, (Online, 2021).

7 J. Wagstaffe, (Online, 2016), Vol. 2021.

8 Carlo E. Campanella, Antonello Cuccovillo, Clarissa Campanella, Abdulkadir Yurt, and Vittorio M. N. Passaro, Sensors **18** (9) (2018).

9 J. H. Chow, D. E. McClelland, M. B. Gray, and I. C. M. Littler, Optics Letters **30** (15), 1923 (2005).

10 Jong H. Chow, Ian C. M. Littler, David E. McClelland, and Malcolm B. Gray, Optics Express **14** (11), 4617 (2006).

11 Gianluca Gagliardi, Mario Salza, Pietro Ferraro, Edmond Chehura, Ralph P. Tatam, Tarun K. Gangopadhyay, Nicholas Ballard, Daniel Paz-Soldan, Jack A. Barnes, Hans-Peter Loock, Timothy T. Y. Lam, Jong H. Chow, and Paolo De Natale, Sensors **10** (3) (2010).

12 Eric D. Black, American Journal of Physics **69** (1), 79 (2000).

13 B. Kennett, *Seismic Wave Propagation in Stratified Media*. (ANU Press, 2009).

14 B. A. Bolt, *Inside the Earth*. (W. H. Freeman and Company, United States of America, 1982), p.191.

15 N. Hazel, Queen's University Canada, 2019.

16 J. Barnes, S. Li, A. Goyal, P. Abolmaesumi, P. Mousavi, and H. P. Loock, Ieee Transactions on Biomedical Engineering **65** (4), 921 (2018).

17 N.; Bakaic Burgwin, M.; Gu, X., US (2018).

18 S. Avino, J. A. Barnes, G. Gagliardi, X. Gu, D. Gutstein, J. R. Mester, C. Nicholaou, and H.-P. Loock, Optics Express **19** (25), 25057 (2011).

19 J. H. Chow, J. S. Cumpston, I. C. M. Littler, D. E. McClelland, and M. B. Gray, (arXiv, 2004).

20 Pi Ceramic, (Online, 2021), Vol. 2021.

21 X. Roselló-Mechó, M. Delgado-Pinar, A. Díez, and M. V. Andrés, Optics Letters **41** (13), 2934 (2016).

22 L. Yan, Z. G. Gui, G. J. Wang, Y. Q. An, J. Y. Gu, M. Q. Zhang, X. L. Liu, Z. B. Wang, G. Wang, and P. G. Jia, Sensors **17** (3) (2017).

23 Hans-Peter Loock and Peter D. Wentzell, Sensors and Actuators B: Chemical **173**, 157 (2012).

24 Michel E. Marhic, *Fiber Optical Parametric Amplifiers, Oscillators and Related Devices*. (Cambridge University Press, Cambridge, 2007).

[25] D. W. Allan, IEEE Transactions on Instrumentation and Measurement **IM-36** (2), 646 (1987).
[26] Patrizia Tosi, Paola Sbarra, and Valerio De Rubeis, Geophysical Research Letters **39** (24) (2012).
[27] Matthieu Sylvander, Christian Ponsolles, Sébastien Benahmed, and Jean-François Fels, Bulletin of the Seismological Society of America **97** (1B), 294 (2007).
[28] M. Wu, Q. Liu, J. Chen, and Z. He, presented at the 2017 25th Optical Fiber Sensors Conference (OFS), 2017 (unpublished).
[29] J. Havskov, P. Bormann, and J. Schweitzer, (GFZ Potsdam, 2011).
[30] Xiong Zhang, Jie Zhang, Congcong Yuan, Sen Liu, Zhibo Chen, and Weiping Li, Scientific Reports **10** (1), 1941 (2020).
[31] W. G. Rees, C. M. Roach, and C. H. F. Glover, J. Opt. Soc. Am. A **8** (2), 330 (1991).
[32] John E. Saunders, Connor Sanders, Hao Chen, and Hans-Peter Loock, Applied Optics **55** (4), 947 (2016).
[33] Z. B. Tian, S. S. H. Yam, and H. P. Loock, Ieee Photonics Technology Letters **20** (13-16), 1387 (2008).
[34] Z. B. Tian, S. S. H. Yam, J. Barnes, W. Bock, P. Greig, J. M. Fraser, H. P. Loock, and R. D. Oleschuk, Ieee Photonics Technology Letters **20** (5-8), 626 (2008).
[35] Z. B. Tian, S. S. H. Yam, and H. P. Loock, Optics Letters **33** (10), 1105 (2008).
[36] Y. Xu, P. Bai, X. D. Zhou, Y. Akimov, C. E. Png, L. K. Ang, W. Knoll, and L. Wu, Advanced Optical Materials **7** (9) (2019).
[37] Kathryn M. Mayer and Jason H. Hafner, Chemical Reviews **111** (6), 3828 (2011).
[38] Moutusi De, Tarun Kumar Gangopadhyay, and Vinod Kumar Singh, Sensors (Basel) **19** (3), 464 (2019).
[39] Vincenza Portosi, Dario Laneve, Mario Christian Falconi, and Francesco Prudenzano, Sensors (Basel) **19** (8), 1892 (2019).
[40] Yanping Xu, Ping Lu, Liang Chen, and Xiaoyi Bao, Fibers **5** (1), 3 (2017).
[41] Francesco Chiavaioli, Francesco Baldini, Sara Tombelli, Cosimo Trono, and Ambra Giannetti, Nanophotonics (Berlin, Germany) **6** (4), 663 (2017).
[42] Aitor Urrutia, Ignacio Del Villar, Pablo Zubiate, and Carlos R. Zamarreño, Laser & photonics reviews **13** (11), 1900094 (2019).
[43] Barbora Spackova, Piotr Wrobel, Marketa Bockova, and Jiri Homola, Proceedings of the IEEE **104** (12), 2380 (2016).
[44] N. L. P. Andrews, R. Ross, D. Munzke, C. van Hoorn, A. Brzezinski, J. A. Barnes, O. Reich, and H. P. Loock, Optics Express **24** (13), 14086 (2016).
[45] Z. Y. Li, Y. P. Wang, C. R. Liao, S. Liu, J. T. Zhou, X. Y. Zhong, Y. J. Liu, K. M. Yang, Q. Wang, and G. L. Yin, Sensors and Actuators B-Chemical **199**, 31 (2014).
[46] Y. Dai, S. S. Tan, Q. Z. Sun, J. H. Wo, Z. L. Xu, and D. M. Liu, Journal of Modern Optics **60** (6), 496 (2013).
[47] C. J. Guo, P. P. Niu, J. Wang, J. F. Zhao, and C. Zhang, Optical Fiber Technology **40**, 46 (2018).
[48] R. Jha, J. Villatoro, G. Badenes, and V. Pruneri, Optics Letters **34** (5), 617 (2009).

[49] P. Torres, E. Reyes-Vera, A. Diez, and M. V. Andres, Optics Letters **39** (6), 1593 (2014).

[50] Z. T. Gu, X. L. Jiang, and H. Y. Chen, in *Sensors, Systems, and Next-Generation Satellites Xvi*, edited by R. Meynart, S. P. Neeck, and H. Shimoda (2012), Vol. 8533.

[51] Vikram Bhatia, Optics Express **4** (11), 457 (1999).

[52] Stephen W. James, Serhiy Korposh, Seung-Woo Lee, and Ralph P. Tatam, Optics Express **22** (7), 8012 (2014).

[53] Ding Jin-Fei, A. P. Zhang, Shao Li-Yang, Yan Jin-Hua, and He Sailing, IEEE Photonics Technology Letters **17** (6), 1247 (2005).

[54] Mateusz Śmietana, Marcin Koba, Predrag Mikulic, and Wojtek J. Bock, Optics Express **24** (11), 11897 (2016).

[55] Z. B. Tian and S. S. H. Yam, Journal of Lightwave Technology **27** (13), 2296 (2009).

[56] W. M. Zhao and Q. Wang, Measurement **139**, 49 (2019).

[57] X. P. Zhang and W. Peng, Ieee Photonics Technology Letters **27** (1), 11 (2015).

[58] X. Liu, Y. Zhao, R. Q. Lv, and Q. Wang, Journal of Lightwave Technology **34** (14), 3293 (2016).

[59] Y. Cao, H. Y. Liu, Z. R. Tong, S. Yuan, and J. Su, Optics Communications **342**, 180 (2015).

[60] R. Huang, K. Ni, X. Y. Wu, and Q. F. Ma, Optics Communications **353**, 27 (2015).

[61] F. D. Yu, P. Xue, X. W. Zhao, and J. Zheng, Ieee Sensors Journal **19** (3), 950 (2019).

[62] J. Zhang, H. Sun, R. H. Wang, D. Su, T. A. Guo, Z. Y. Feng, M. L. Hu, and X. G. Qiao, Ieee Sensors Journal **13** (6), 2061 (2013).

[63] X. Yan, H. W. Fu, H. D. Li, and X. G. Qiao, Chinese Optics Letters **14** (3) (2016).

[64] H. P. Gong, P. C. Yang, H. F. Song, K. Ni, and X. Y. Dong, Optik **126** (21), 3058 (2015).

[65] X. Y. Sun, X. R. Dong, Y. W. Hu, H. T. Li, D. K. Chu, J. Y. Zhou, C. Wang, and J. Duan, Sensors and Actuators a-Physical **230**, 111 (2015).

[66] S. H. Aref, Optical Fiber Technology **38**, 98 (2017).

[67] M. Janik, T. Eftimov, M. Koba, M. Smietana, and W. J. Bock, in *Advanced Fabrication Technologies for Micro/Nano Optics and Photonics Xi* (2018), Vol. 10544.

[68] M. Janik, M. Koba, A. Celebanska, W. J. Bock, and M. Smietana, Optics and Laser Technology **103**, 260 (2018).

[69] F. F. Chen, Y. Jiang, L. C. Zhang, L. Jiang, and S. M. Wang, Measurement Science and Technology **29** (4) (2018).

[70] X. Y. Sun, D. K. Chu, X. R. Dong, Zhou Chu, H. T. Li, Zhi Luo, Y. W. Hu, J. Y. Zhou, Wang Cong, and J. A. Duan, Optics and Laser Technology **77**, 11 (2016).

[71] Z. F. Gong, X. P. Zhang, Y. Liu, Z. G. Liu, and W. Peng, in *Advanced Sensor Systems and Applications Vi*, edited by T. Liu, S. Jiang, and N. Neumann (2014), Vol. 9274.

[72] V. Ahsani, F. Ahmed, M. B. G. Jun, and C. Bradley, Sensors **19** (7) (2019).

[73] J. E. Betancur-Ochoa, V. P. Minkovich, and Y. J. Montagut-Ferizzola, Journal of Lightwave Technology **35** (21), 4747 (2017).

[74] G. A. Cardenas-Sevilla, D. Monzon-Hernandez, I. Torres-Gomez, and A. Martinez-Rios, Optics and Laser Technology **44** (5), 1516 (2012).

[75] A. Dudus, R. Blue, and D. Uttamchandani, Ieee Sensors Journal **13** (5), 1594 (2013).

[76] A. D. Gomes and O. Frazao, Ieee Photonics Technology Letters **29** (18), 1517 (2017).

[77] Q. Z. Sun, H. P. Luo, H. B. Luo, M. C. Lai, D. M. Liu, and L. Zhang, Optics Express **23** (10), 12777 (2015).

[78] C. H. Chen, C. Y. Hsu, P. H. Huang, J. N. Wang, and W. T. Wu, International Journal of Antennas and Propagation (2014).

[79] Z. T. Cao, L. Jiang, S. M. Wang, P. Wang, F. Zhang, and Y. F. Lu, Applied Optics **53** (6), 1028 (2014).

[80] R. Cherif, A. Ben Salem, and M. Zghal, in *Micro-Structured and Specialty Optical Fibres Ii*, edited by K. Kalli, J. Kanka, and A. Mendez (2013), Vol. 8775.

[81] B. J. Luff, J. S. Wilkinson, J. Piehler, U. Hollenbach, J. Ingenhoff, and N. Fabricius, Journal of Lightwave Technology **16** (4), 583 (1998).

[82] H. Y. Choi, M. J. Kim, and B. H. Lee, Optics Express **15** (9), 5711 (2007).

[83] Byeong Ha Lee and Junji Nishii, Applied Optics **38** (16), 3450 (1999).

[84] L. Alwis, T. Sun, and K. T. V. Grattan, Measurement **46** (10), 4052 (2013).

[85] G. Berden and Richard Engeln, *Cavity Ring-Down Spectroscopy: Techniques and Applications*. (2010).

[86] Bahaa E. A. Saleh and Malvin Carl Teich, *Fundamentals of photonics*, 2nd ed. (Wiley-Interscience, Hoboken, N.J, 2007).

[87] H. W. Fu, X. Yan, M. Shao, H. D. Li, H. Gao, Z. A. Jia, and X. G. Qiao, Ieee Photonics Technology Letters **27** (6), 658 (2015).

[88] O. Frazao, J. L. Santos, and J. M. Baptista, Ieee Photonics Technology Letters **19** (13-16), 1260 (2007).

[89] Gianluca Gagliardi and Hans-Peter Loock, *Cavity-Enhanced Spectroscopy and Sensing*, 2014 ed. (Springer Berlin Heidelberg, Berlin, Heidelberg, 2014).

[90] Gianluca Gagliardi, Hans-Peter Loock, and SpringerLink, *Cavity-Enhanced Spectroscopy and Sensing*. (Springer Berlin Heidelberg, Berlin, Heidelberg, 2014).

[91] Klaus Bescherer, Dorit Munzke, Oliver Reich, and Hans-Peter Loock, Applied optics. Optical technology and biomedical optics **52** (4), B40 (2013).

[92] M. Janik, M. Koba, W. J. Bock, and M. Smietana, in *Electron Technology Conference 2016*, edited by B. Swatowska, W. Maziarz, T. Pisarkiewicz et al. (2016), Vol. 10175.

[93] A. K. Debowska, M. Dominik, M. Koba, M. Janik, W. Bock, and M. Smietana, in *Electron Technology Conference 2016*, edited by B. Swatowska, W. Maziarz, T. Pisarkiewicz et al. (2016), Vol. 10175.

[94] B. T. Wang and Q. Wang, Optics Communications **426**, 388 (2018).

[95] Z. Y. Li, C. R. Liao, Y. P. Wang, X. P. Dong, S. Liu, K. M. Yang, Q. Wang, and J. T. Zhou, Optics Letters **39** (17), 4982 (2014).

[96] C. R. Liao, Y. Wang, D. N. Wang, and M. W. Yang, IEEE Photonics Technology Letters **22** (22), 1686 (2010).

[97] Y. W. Qi, S. Y. Zhang, S. F. Feng, X. K. Wang, W. F. Sun, J. S. Ye, P. Han, and Y. Zhang, in *2017 International Conference on Optical Instruments and Technology - Irmmw-Thz Technologies and Their Applications*, edited by C. Zhang, X. C. Zhang, and Z. Huang (2017), Vol. 10623.

[98] F. Ahmed, V. Ahsani, L. Melo, P. Wild, and M. B. G. Jun, Ieee Sensors Journal **16** (24), 8761 (2016).

[99] I. Shavrin, S. Novotny, A. Shevchenko, and H. Ludvigsen, Applied Physics Letters **100** (5) (2012).

[100] F. Ahmed, V. Ahsani, S. Jo, C. Bradley, E. Toyserkani, and M. B. G. Jun, Ieee Photonics Technology Letters **31** (1), 74 (2019).

[101] C. Chen, R. Yang, X. Y. Zhang, W. H. Wei, Q. Guo, X. Zhang, L. Qin, Y. Q. Ning, and Y. S. Yu, Optical Materials Express **8** (4), 919 (2018).

[102] X. H. Fu, J. P. Zhang, S. W. Wang, G. W. Fu, Q. Liu, W. Jin, and W. H. Bi, in *Advanced Sensor Systems and Applications Vii*, edited by T. Liu, S. Jiang, and R. Landgraf (2016), Vol. 10025.

[103] Wei Chang Wong, Chi Chiu Chan, Li Han Chen, Zhi Qiang Tou, and Kam Chew Leong, Optics Letters **36** (9), 1731 (2011).

[104] C. R. R. Liao, D. N. Wang, M. Wang, and M. H. Yang, Ieee Photonics Technology Letters **24** (22), 2060 (2012).

[105] D. Juan Juan Hu, J. Long Lim, Y. Wang, and P. Ping Shum, presented at the SENSORS, 2011 IEEE, 2011 (unpublished).

[106] L. Yuan, H. B. Wu, C. Wang, Y. Y. Yu, S. M. Wang, and H. Xiao, in *2013 International Conference on Optical Instruments and Technology: Optical Sensors and Applications*, edited by B. Culshaw, X. Zhang, A. Wang et al. (2013), Vol. 9044.

[107] M. I. Zibaii, P. A. S. Jorge, O. Frazao, and H. Latifi, in *International Conference on Applications of Optics and Photonics* (2011), Vol. 8001.

[108] P. Gao, X. Y. Chen, and W. J. Feng, Review of Scientific Instruments **83** (10) (2012).

[109] C. Y. Han, H. Ding, X. L. Li, and S. F. Dong, Applied Physics Letters **104** (18) (2014).

[110] L. P. Sun, J. Li, S. Gao, L. Jin, Y. Ran, and B. O. Guan, Optics Letters **39** (12), 3531 (2014).

[111] W. Jin, C. Wang, and H. F. Xuan, Optics Letters **38** (21), 4277 (2013).

[112] S. C. Gao, W. G. Zhang, Z. Y. Bai, H. Zhang, W. Lin, L. Wang, and J. L. Li, Journal of Lightwave Technology **32** (9), 1682 (2014).

[113] Marta S. Ferreira, Luís Coelho, Kay Schuster, Jens Kobelke, José L. Santos, and Orlando Frazão, Optics Letters **36** (20), 4029 (2011).

[114] D. W. Duan, Y. J. Rao, and T. Zhu, Journal of the Optical Society of America B-Optical Physics **29** (5), 912 (2012).

[115] E. Cibula and D. Donlagic, IEEE Photonics Technology Letters **23** (21), 1609 (2011).

[116] T. T. Wang, Y. X. Ge, J. H. Chang, and M. Wang, Ieee Photonics Technology Letters **28** (1), 3 (2016).

[117] Y. Xiang, Y. Y. Luo, Y. P. Li, Y. Li, Z. J. Yan, D. M. Liu, and Q. Z. Sun, Ieee Photonics Journal **10** (2) (2018).

[118] P. G. Jia, G. C. Fang, T. Liang, Y. P. Hong, Q. L. Tan, X. Y. Chen, W. Y. Liu, C. Y. Xue, J. Liu, W. D. Zhang, and J. J. Xiong, Sensors and Actuators B-Chemical **244**, 226 (2017).

[119] J. J. Zhang, Q. Z. Sun, R. B. Liang, W. H. Jia, X. L. Li, J. H. Wo, D. M. Liu, and P. P. Shum, Journal of Lightwave Technology **31** (10), 1608 (2013).

[120] Kristian Mølhave, Anders Kristensen, and Niels Asger Mortensen, in *Advanced Photonic Structures for Biological and Chemical Detection*, edited by Xudong Fan (Springer New York, New York, NY, 2009), pp. 471.

[121] Saverio Avino, Anika Krause, Rosa Zullo, Antonio Giorgini, Pietro Malara, Paolo De Natale, Hans Peter Loock, and Gianluca Gagliardi, Advanced Optical Materials **2** (12), 1155 (2014).

[122] D. K. Armani, T. J. Kippenberg, S. M. Spillane, and K. J. Vahala, Nature **421** (6926), 925 (2003).

[123] M. L. Gorodetsky, A. A. Savchenkov, and V. S. Ilchenko, Optics Letters **21** (7), 453 (1996).

[124] H. M. Tzeng, K. F. Wall, M. B. Long, and R. K. Chang, Optics Letters **9** (11), 499 (1984).

[125] Hatim Azzouz, Søren Balslev, and Anders Kristensen, edited by T. Laurell, J. Nilsson, K. Jensen et al. (Royal Society of Chemistry, Cambridge, United Kingdom, 2004), Vol. 1, pp. 578.

[126] M. Aas, A. Jonáš, and A. Kiraz, Optics Communications **290**, 183 (2013).

[127] A. Kiraz, A. Sennaroglu, S. Doğanay, M. A. Dündar, A. Kurt, H. Kalaycıoğlu, and A. L. Demirel, Optics Communications **276** (1), 145 (2007).

[128] A. K. Ray, R. D. Johnson, and A. Souyri, Langmuir **5** (1), 133 (1989).

[129] A. Kiraz, Y. Karadağ, and M. Muradoğlu, Physical Chemistry Chemical Physics **10** (42), 6446 (2008).

[130] Alexandr Jonáš, Yasin Karadag, Michael Mestre, and Alper Kiraz, J. Opt. Soc. Am. B **29** (12), 3240 (2012).

[131] Jared A. Baird, Roberto Olayo-Valles, Carlos Rinaldi, and Lynne S. Taylor, Journal of Pharmaceutical Sciences **99** (1), 154 (2010).

[132] Sindy K. Y. Tang, Zhenyu Li, Adam R. Abate, Jeremy J. Agresti, David A. Weitz, Demetri Psaltis, and George M. Whitesides, Lab on a Chip **9** (19), 2767 (2009).

[133] Liyuan Zhao, Yan Wang, Yonggui Yuan, Yongjun Liu, Shuangqiang Liu, Weimin Sun, Jun Yang, and Hanyang Li, Optics Communications **402**, 181 (2017).

[134] Alper Kiraz, Qiushu Chen, and Xudong Fan, ACS Photonics **2** (6), 707 (2015).

[135] T. H. Maiman, Nature **187** (4736), 493 (1960).

[136] C. G. B. Garrett, W. Kaiser, and W. L. Bond, Physical Review **124** (6), 1807 (1961).

[137] W. V. Sorin and M. H. Yu, Optics Letters **10** (11), 550 (1985).

[138] G. Das and J. W. Y. Lit, IEEE Photonics Technology Letters **16** (1), 60 (2004).

[139] B. Sprenger, H. G. L. Schwefel, and L. J. Wang, Optics Letters **34** (21), 3370 (2009).

[140] Hossein Hodaei, Mohammad-Ali Miri, Matthias Heinrich, Demetrios N. Christodoulides, and Mercedeh Khajavikhan, Science (American Association for the Advancement of Science) **346** (6212), 975 (2014).

[141] Alexander W. Fang, Brian R. Koch, Kian-Giap Gan, Hyundai Park, Richard Jones, Oded Cohen, Mario J. Paniccia, Daniel J. Blumenthal, and John E. Bowers, Optics Express **16** (2), 1393 (2008).

[142] A. Polman, B. Min, J. Kalkman, T. J. Kippenberg, and K. J. Vahala, Applied Physics Letters **84** (7), 1037 (2004).

[143] S. X. Qian, J. B. Snow, H. M. Tzeng, and R. K. Chang, Science **231** (4737), 486 (1986).

[144] A. Ashkin and J. M. Dziedzic, Science **187** (4181), 1073 (1975).

[145] A. Ashkin and J. M. Dziedzic, Physical Review Letters **38** (23), 1351 (1977).

[146] A. Sennaroglu, A. Kiraz, M. A. Dündar, A. Kurt, and A. L. Demirel, Optics Letters **32** (15), 2197 (2007).

[147] Andrei A. Bunaciu, Hassan Y. Aboul-Enein, and Şerban Fleschin, Applied spectroscopy reviews **50** (2), 176 (2015).

[148] Lord Rayleigh, The London, Edinburgh, and Dublin Philosophical Magazine and Journal of Science **20** (120), 1001 (1910).

[149] Nikita Toropov, Gema Cabello, Mariana P. Serrano, Rithvik R. Gutha, Matías Rafti, and Frank Vollmer, Light: Science & Applications **10** (1), 42 (2021).

[150] J. Barnes, B. Carver, J. M. Fraser, G. Gagliardi, H. P. Loock, Z. Tian, M. W. B. Wilson, S. Yam, and O. Yastrubshak, Optics Express **16** (17), 13158 (2008).

[151] Niranjan M. Hanumegowda, Caleb J. Stica, Bijal C. Patel, Ian White, and Xudong Fan, Applied physics letters **87** (20), 201107 (2005).

[152] Vladimir S. Ilchenko, X. Steve Yao, and Lute Maleki, Optics Letters **24** (11), 723 (1999).

[153] Saverio Avino, Anika Krause, Rosa Zullo, Antonio Giorgini, Pietro Malara, Paolo De Natale, Hans Peter Loock, and Gianluca Gagliardi, Advanced Optical Materials **2** (12), 1155 (2014).

[154] Antonio Giorgini, Saverio Avino, Pietro Malara, Paolo De Natale, and Gianluca Gagliardi, Sensors **19** (3), 473 (2019).

[155] A Yariv, Ed. John Wiley & Sons, New York, NY, 123 (1975).

[156] K. Bescherer, J. A. Barnes, S. Dias, G. Gagliardi, H. P. Loock, N. R. Trefiak, H. Waechter, and S. Yam, Applied Physics B **96** (1), 193 (2009).

[157] Peter Hammond and Diane Cooke, Applied Optics **31** (33), 7095 (1992).

[158] Ravi Kumar Kanaparthi, Satyen Saha, Manjeev Singh, and Akhila M, (2020).

[159] E. Potma and S. Mukamel, *Theory of Coherent Raman Scattering*. (CRC Press, 2013).

Chapter 7 Appendix

7.1. Correction for dispersion

The equations given above all neglect the effect of dispersion. In the following paragraphs we introduce dispersion as a correction to the above calculations. Oftentimes the effect cannot be neglected, and it is necessary to invoke dispersion relations especially when high-order cladding modes are responsible for the changes in the sensing arm.

If the interference is between an isolated core mode in the reference arm and a cladding mode in the sensing arm, the condition for destructive interference, at wavelength $\lambda_{min,j}$, can be written as

$$\frac{2\pi L}{\lambda_{\min,i}}\left[n_{co}^{eff}(\lambda)-n_{cl,m}^{eff}(\lambda,n_{ex})\right]=(2k-1)\pi \qquad (7.1.1)$$

where $n_{co}^{eff}(\lambda)$ and $n_{cl,m}^{eff}(\lambda,n_{ex})$ are the effective refractive indices of the core and *m*th order cladding modes respectively, *L* is the interaction length and *k* is an integer. Equation (1) can be rearranged to give

$$\lambda_{\min,i}=\frac{2L\left[n_{co}^{eff}(\lambda)-n_{cl,m}^{eff}(\lambda,n_{ex})\right]}{2k-1}=\frac{2L\Delta n_{m}^{eff}}{2k-1} \qquad (7.1.2)$$

With (3.4.7) the sensitivity of the interferometer to changes in external refractive index can be obtained by evaluating under the assumption that only the cladding mode interacts with the sample

$$S=\frac{d\lambda_{\min,k}}{dn_s}=\chi\frac{\partial n_{cl,m}^{eff}}{\partial n_s} \qquad (7.1.3)$$

where in the most general case

$$\chi=-\frac{\lambda_{\min,k}}{\Delta n_{eff,m}}\left[1-\frac{\lambda_{\min,k}}{\Delta n_{eff,m}}\left(\frac{\partial n_{co}^{eff}}{\partial\lambda}-\frac{\partial n_{cl,m}^{eff}}{\partial\lambda}\right)\right]^{-1} \qquad (7.1.4)$$

and where χ is related to *f* under the assumption that n_{co} does not depend on n_s/n_{ex}.

$$S=\frac{2\pi L}{\Delta\phi}\frac{d\Delta n^{eff}}{dn_s} \qquad (7.1.5)$$

where for attenuation maxima $\Delta\phi = 2\pi\left(m+1/2\right)$ with *m* being an integer. By substituting Eq. (3.4.3) into Eq. (3.4.6) or (3.4.7), we can give the sensitivity coefficient

$$f = \frac{d\Delta n^{eff}}{dn_s} \tag{7.1.6}$$

In (7.1.3), $\frac{\partial n_{cl,m}^{eff}}{\partial n_s}$ is a positive quantity, which becomes larger in magnitude with increasing mode order; hence, the sign of the sensitivity $S = \frac{d\lambda_{\min,k}}{dn_s}$ is dictated by the sign of χ. In Equation (4), $\frac{\lambda_{\min,k}}{\Delta n_{eff,m}}$ is always positive so that the sign of χ is determined by the denominator of the expression. When $\frac{\partial n_{cl,m}^{eff}}{\partial\lambda} > \frac{\partial n_{co}^{eff}}{\partial\lambda}$, χ will be negative and λ_{min} will show a blue shift with increasing external refractive index. This response is typical when low-order cladding modes are excited in a single-mode fibre. When $\frac{\partial n_{cl,m}^{eff}}{\partial\lambda} < \frac{\partial n_{co}^{eff}}{\partial\lambda}$, the sign of χ will depend on whether $\frac{\lambda_{\min,k}}{\Delta n_{eff,m}}\left(\frac{\partial n_{co}^{eff}}{\partial\lambda} - \frac{\partial n_{cl,m}^{eff}}{\partial\lambda}\right)$ is greater or less than 1. These two cases apply for higher-order cladding mode excitation.

It may be the case that multiple cladding modes are excited and interfere, in which case all modes involved are influenced by the external refractive index. In this case we may write

$$\frac{d\lambda_{\min,k}}{dn_{ex}} = \chi_{cl}\left(\frac{\partial n_{cl,m}^{eff}}{\partial n_{ex}} - \frac{\partial n_{cl,j}^{eff}}{\partial n_{ex}}\right), m > j \tag{7.1.7}$$

where

$$\chi_{cl} = \frac{\lambda_{\min,k}}{\Delta n_{eff,mj} - \lambda_{\min,k}\left(\frac{\partial n_{cl,m}^{eff}}{\partial\lambda} - \frac{\partial n_{cl,j}^{eff}}{\partial\lambda}\right)} \tag{7.1.8}$$

The bracketed quantity in Equation (7.1.8) is positive, but no general statement can be made about the sign of χ_{cl}. From the general considerations above, we can see

that when multi-mode interference is involved the magnitude and sign of the refractive index sensitivity will strongly depend on which modes are involved and the power distribution between those modes.

7.2. Determination of the refractive index of mixtures

In many previous studies the refractive index of a sample liquid is adjusted by making mixtures of liquids with known indices. Contrary to common assumptions the refractive index of a sample solution, n_s, does not change linearly with the mole fraction or volume fraction of the constituents. Instead one has to use the Lorentz-Lorenz equation Saunders, et al. [32]

$$\frac{n_s^{\,2}-1}{2+n_s^{\,2}} = \sum_i \chi_i \frac{\rho_i N_A}{3\varepsilon_0}\frac{\alpha_i}{M_i} \qquad (7.2.1)$$

to determine the refractive index where the polarizability of the solution can be obtained, to a good approximation, from the weighted sum of the polarizabilities of the constituent compounds.

$$\alpha_{LL}(x) = \sum_i x_i \alpha_i \qquad (7.2.2)$$

In these equations, N_A is Avogadro's number, ε_0 is the vacuum permittivity, M_i is the respective molar mass of the neat components, and their densities are given by, ρ_i. The refractive index of the solution or mixture can accordingly be calculated from mole fractions x_1 and $x_2 = (1 - x_1)$, the electronic polarizabilities, α_i, and density of the solution. Note that the volume of solutions is not linearly additive. The deviation from the expected additive volume is known as the excess molar volume and can be positive or negative. The excess volume may be determined from the molar masses, M_i, as well as the masses of the components added to the solution, m_i, if the density of the solution as a function of mole fraction, $\rho(x)$, is known.

$$V_{exc}(x) = \frac{1}{\sum(m_i/M_i)}\left[\frac{\sum m_i}{\rho(x)} - \sum\left(\frac{m_i}{\rho_i}\right)\right] \qquad (7.2.3)$$

It was previously shown that the Lorentz-Lorenz equation is valid to within better than 1% of the expected refractive index, i.e., to about 10,000 ppm, under the assumption that appropriate corrections for the excess volume have been made. In those studies, where sample solutions were prepared in-house from neat constituents to generate a calibration curve, these conditions are not always given, and the accuracy of the measurements may then suffer from errors in the calculated indices of the calibration solutions.

7.3. Calculation of the modulation depth on a logarithmic (dB) scale

In (7.3.1), we calculate the modulation depth on a dB scale using the known quantities of the HWHM $dB_{1/2}$, maxima $dB_{\max}$, and minima $dB_{\min}$ on a dB scale.

$$\begin{aligned} M'_{1/2} &= \frac{10^{\frac{dB_{1/2}}{10}}}{10^{\frac{dB_{max}}{10}}} = 10^{\frac{dB_{1/2}}{10} - \frac{dB_{\max}}{10}} = 10^{0.1(dB_{1/2} - dB_{\max})} = 10^{0.1(0.5dB_{\max} + 0.5dB_{\min} - dB_{\max})} \\ &= 10^{0.1(0.5dB_{\min} - 0.5dB_{\max})} = 10^{0.05(dB_{\min} - dB_{\max})} = 1.122^{(dB_{\min} - dB_{\max})} \end{aligned} \qquad (7.3.1)$$

7.4. Conversion of the HWHM of a function on a dB scale (interferometer) to the HWHM of a cosine function on an absolute scale

Interferograms are cosine functions. For large values of *m* we find a symmetric peak at each fringe centred around λ_0, with a peak height $I_{\max}$, a baseline of $I_{\min}$ and a half-width at half-maximum, $\lambda'_{1/2}$

$$\frac{I(\lambda) - I_{\min}}{I_{\max} - I_{\min}} = \frac{1}{2}\cos\left(\frac{\pi}{2}\frac{\lambda - \lambda_0}{\gamma}\right) + \frac{1}{2} \qquad (7.4.1)$$

On a linear scale, the right term evaluates to 1/2 when $(\lambda - \lambda_0) = \lambda_{1/2}$, corresponding to the half maximum of the cosine function. When $\lambda'_{1/2}$ is instead measured on a dB-scale the LHS of (7.4.1) transforms to

$$\frac{dB\left[I(\lambda)\right]-dB\left[I_{\min}\right]}{dB\left[I_{\max}\right]-dB\left[I_{\min}\right]}=\frac{1}{2} \tag{7.4.2}$$

Using $dB[f(x)] = 10\log_{10}(f(x))$ and (7.4.1) we can express (7.4.2) as

$$\frac{1}{2}=\frac{\log\left[\left(I_{\max}-I_{\min}\right)\left(\frac{1}{2}\cos\left(\frac{\pi}{2}\frac{\lambda'_{1/2}}{\lambda_{1/2}}\right)+\frac{1}{2}\right)+I_{\min}\right]-\log\left[I_{\min}\right]}{\log\left[I_{\max}\right]-\log\left[I_{\min}\right]} \tag{7.4.3}$$

which may be rearranged to give

$$\lambda_{1/2}=\frac{\pi}{2}\left(\lambda'_{1/2}\right)\left(\cos^{-1}\left(2M''-1\right)\right)^{-1} \tag{7.4.4}$$

where we define the modulation depth as

$$\begin{aligned} M'' &= \frac{10^{\frac{1}{2}\left(\log\left[I_{\max}\right]+\log\left[I_{\min}\right]\right)}-I_{\min}}{\left(I_{\max}-I_{\min}\right)} \\ &= \frac{10^{\frac{1}{2}\left(dB\left[I_{\max}\right]+dB\left[I_{\min}\right]\right)}-10^{dB(I_{\min})}}{10^{dB(I_{\max})}-10^{dB(I_{\min})}} \end{aligned} \tag{7.4.5}$$

Equation (7.4.4) may be used to determine the half-width of an interferometer fringe on an absolute scale, $\lambda_{1/2}$, if the HWHM is known on the dB-scale as, $\lambda'_{1/2}$, and if the maximum and minimum intensities on a dB scale, $dB[I_{max}]$ and $dB[I_{min}]$, are known.

7.5. Conversion from the HWHM of a function on a dB scale (cavity resonance) to the HWHM of a Lorentzian function on an absolute scale

Cavity resonances can be approximated with good accuracy as Lorentzian functions. Their half-width at half-maximum, $\lambda_{1/2}$, produces a symmetric peak around λ_0, with a peak height $I_{\max}$ and a baseline of $I_{\min}$.

$$\frac{I(\lambda)-I_{\min}}{I_{\max}-I_{\min}}=\frac{1}{1+\left(\frac{\lambda-\lambda_0}{\lambda_{1/2}}\right)^2} \tag{7.4.6}$$

On an absolute scale, the right term evaluates to ½ when $\left(\lambda-\lambda_0\right)=\lambda_{1/2}$. We are interested to determine $\lambda_{1/2}$ when the HWHM, $\left(\lambda_{dB_{1/2}}-\lambda_0\right)$,is instead determined from

a spectrum given on a dB-scale. In that case we can use (7.4.2) and dB[f(x)]=10 $\log_{10}$(f(x)) to write, for the Fabry-Perot cavity,

$$\frac{\log\left[\dfrac{I_{\max}-I_{\min}}{1+\left(\dfrac{\lambda_{dB_{1/2}}-\lambda_0}{\gamma}\right)^2}+I_{\min}\right]-\log\left[I_{\min}\right]}{\log\left[I_{\max}\right]-\log\left[I_{\min}\right]}=\frac{1}{2} \qquad (7.4.7)$$

which may be rearranged to give

$$\gamma=\left(\lambda_{dB_{1/2}}-\lambda_0\right)\left(\frac{1}{M''}-1\right)^{-1/2} \qquad (7.4.8)$$

This equation may be used to determine the half-width of a cavity resonance on an absolute scale, γ, if it is known on the dB-scale as $\left(\lambda_{dB_{1/2}}-\lambda_0\right)$.